공학박사 학위논문

Comparison of the aero-optical effects due to shock wave and boundary layer in high-speed flow

고속 유동에서 충격파 및 경계층에 의한 공기광학 효과 비교

2020년 8월

서울대학교 대학원

기계항공공학부

이상윤

Comparison of the aero-optical effects due to shock wave and boundary layer in high-speed flow

고속 유동에서 충격파 및 경계층에 의한 공기광학 효과 비교

지도교수 이 복 직

이 논문을 공학박사 학위논문으로 제출함
2020년 5월

서울대학교 대학원
기계항공공학부
이 상 윤

이상윤의 공학박사 학위논문을 인준함
2020년 6월

위 원 장 _____ (인)

부 위 원 장 _____ (인)

위 원 _____ (인)

위 원 _____ (인)

위 원 _____ (인)

Abstract

Comparison of the aero-optical effects due to shock wave and boundary layer in high-speed flow

Sangyoon Lee
Department of Mechanical and Aerospace Engineering
The Graduate School
Seoul National University

An antiballistic missile seeker is essential for a successful interception. However, aero-optical effects due to the flow field around the seeker window degrade the image captured using the seeker, making it difficult to identify the target. Thus, studying aero-optical phenomena and calibrating the images are necessary to improve the performance of seekers. Flight speed of antiballistic missiles are usually supersonic or hypersonic, where shock waves and boundary layers are inevitable and always exist. Therefore it is important to understand the aero-optical effects due to these flow features. In this dissertation, aero-optical phenomena due to the shock wave and boundary layer in supersonic and hypersonic flow are compared using numerical and experimental methods. In addition, a new experimental method based on background-oriented schlieren (BOS) is suggested and well validated using a Shack-Hartmann wavefront sensor in a subsonic heated jet. Because the BOS-based method could simultaneously visualize

the flow and acquire optical characteristics, it is expected that flow properties could be more closely related to aero-optical effects. For supersonic flow, the flow field around the compression ramp is studied, and for hypersonic flow, the flow field around the wedge and cone model is investigated. To study the individual contribution of the shock wave and boundary layer to the wavefront distortion, numerical simulation is conducted. Flow is simulated by solving the two-dimensional Reynolds-averaged Navier-Stokes equations, and the ray-tracing method has been adopted to calculate the propagation of the optical wave. The deflection angle of the ray at the center of the laser beam is analyzed to assess the aero-optical effects caused by the shock wave and boundary layer. In the current wavefront measurement configuration, aero-optical effects due to two boundary layers cancel out and only shock wave effect remains. To compare aero-optical effects due to only one boundary layer and the shock wave, numerical simulations are conducted with a slip condition on the one side of the wall. From these numerical simulations, the aero-optical effects due to shock wave and boundary layer are comparable, Therefore the aero-optical effects due to the shock wave and the boundary layer are both important for the flow field around the window of the seekers.

Keywords: Aero-optics, Shock wave, Supersonic flow, Hypersonic flow, Wavefront measurement, Ray -racing, Background-oriented schlieren

Contents

List of Figures

List of Tables

Nomenclature

Symbols

f	Focal length
H	Height
J_0	Zeroth order Bessel function of first kind
K_{gd}	Gladstone-Dale constant
M	Mach number
N	Total number of samples
n	Index of refraction (Refractive index)
n_0	Refractive index of the reference state
p	Pressure
p_1	Pressure of driven tube
p_4	Pressure of driver tube
r	Position of the ray
s	Distnace along the ray path
T	Temperature

W	Width
y^+	Dimensionless distance to the wall
z_b	Distance from the mid-plane of the flow to background pattern
z_c	Distance from the mid-plane of the flow to the camera
z_f	Width of the flow or width of the test section

Greek symbols

α	Coefficient for adaptive Fourier-Hankel method
β	Angle of a oblique shock wave
λ	Wavelength of light
ρ	Density
θ	Angle
ε	Deflection angle

Subscripts

0	Stagnation condition
rms	Root mean square
w	Wavefront

Abbreviations

2D	Two-dimensional
3D	Three-dimensional
AHF	Adaptive Fourier-Hankel
AOA	Angle of attack

AST2 Aerospace Propulsion and Combustion Laboratory Shock Tunnel 2

BOS Background-orietnted schlieren

BSE Boresight error

CCD Charge-coupled device

DSLR Digital single-lens reflex

ISSW International Symposium on Shock Waves

LOS Line of sight

MOCs Methods of characteristics

NPLS Nanoparticle-based planar laser scattering

OPD Optical path length difference

OPL Optical path length

PET Polyethylene terephthalate

PSF Point spread function

PV Peak-to-valley

RANS Reynolds-averaged Navier-Stokes

SABT Small-aperture beam technique

SHWS Shack-Hartmann wavefront sensor

TTL Transistor-Transistor Logic

Chapter 1

Introduction

In this chapter, the motivations for the dissertation and fundamentals of aero-optics are described. In the first part of the chapter, the background of the study on aero-optics in high-speed flow is explained. Problems due to the aero-optical phenomena on missile seekers are introduced, and fundamental theories for aero-optics are discussed. In the second part of the chapter, the previous studies on aero-optical phenomena in high-speed flow are introduced. The results of these previous studies are presented, and the methods used for the investigation of aero-optical phenomena are categorized. In the final part of the chapter, the objective and scope of the dissertation are described.

1.1 Background

Ever since the ballistic missile V-2 and atomic bomb demonstrated their power during the mid-twentieth century, research has been conducted to combine both technologies to develop powerful weapons [3]. As such, nuclear weapons with extended ranges and faster speed have been developed. Some of these weapons even cross the continents and threat all over the world. Therefore the demands on the missile defense system have grown nowadays. The missile defense system, such as Arrow 3 or Terminal High Altitude Area Defense (THAAD) [4], detects ballistic missiles and launches hypersonic antiballistic missiles to intercept and destroy ballistic missiles before they reach the destination. Antiballistic missiles usually navigate to the target missile with the aid of radar, but at the final phase of interception, the missile seeker installed on the antiballastic missile tracks the target and leads the interceptor to the target [5]. If the seeker fails to track the exact location of the target, the interceptor misses it, and the atomic bomb strikes the destination. Therefore, the tracking performance of the seeker is essential for the success of the interception of ballistic missiles.

Seekers track the target by capturing images using an optical sensor and then distinguish the target from the captured images. Thus, acquiring high-quality images with an optical sensor is essential to

track the target accurately. However, the optical sensor must capture images through the flow field surrounding the seeker, as illustrated in Fig. 1.1, where the complicated flow field is formed around the seeker window [6]. When the image of a subject is captured through the flow field, the target is blurred or displaced from the original position, as depicted in Fig. 1.2, where the object beyond the shock wave and wingtip vortex is distorted and difficult to recognize. This distortion of the image due to the flow field is known as an aero-optical phenomenon. Due to aero-optical phenomena, the images acquired using optical sensors are blurred, or the position of the target is displaced from its original position, decreasing the accuracy of the seeker. Thus, research has been conducted to enhance the accuracy of the seeker by understanding the aero-optical phenomena, predicting the distortion of the images due to the flow field, and calibrating the captured images using predicted data [7].

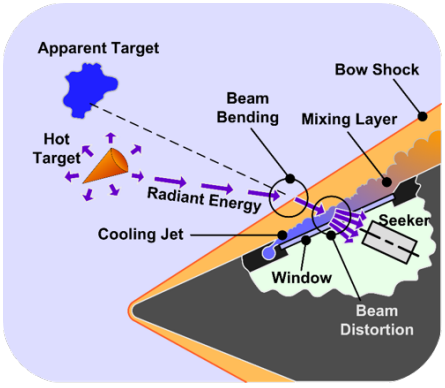

Figure 1.1: Flow field around a missile seeker and the distortion of light due to the flow field.

(a) (b)

Figure 1.2: Distortion of images due to (**a**) shock waves [1] and (**b**) wingtip vortex [2].

The main flow features around the seeker of the hypersonic interceptor are the shock wave, boundary layer, and mixing layer. Shock waves are generated when fight speed is supersonic and acts as a lens, refracting and dispersing the optical wave [6, 8]. The boundary layer refracts the rays, and if the boundary layer is turbulent, scattering also occurs, resulting in a reduction of intensity and blurriness in the images [8]. The mixing layer is usually generated due to the cooling jet, or cooling film, which is used to lower the temperature of the seeker window, which is heated by aerodynamic heating. The mixing layer acts similarly as a turbulent boundary layer, and the optical waves are refracted and scattered, blurring the images or reducing the intensity. Furthermore, the seeker vibrates due to the aerodynamic force, which results in jitter and blurriness in the images [8]. Among these flow features, shock waves and boundary layers are inevitable

during supersonic and hypersonic flight. Furthermore, the variation of the density of the flow due to the shock wave and boundary layer is relatively higher than other flow features. Thus, understanding the aero-optical phenomena due to the shock wave and boundary layer is essential for the enhancement of seeker accuracy. Therefore, in this dissertation, the aero-optical phenomena due to the shock wave and boundary layer in supersonic and hypersonic flows are investigated.

1.2 Introduction to Aero-optics

The propagation of optical waves is dependent on the index of refraction of the medium. In a gaseous medium, the index of refraction is related to the density of the gas. The Gladstone-Dale equation illustrates the relationship between the index of refraction and the density of the gas:

$$n = 1 + K_{\mathrm{gd}}\rho, \tag{1.1}$$

where K_{gd} depends on the medium and wavelength, which is about 2.25×10^{-4} m^3/kg in the air for a laser with a wavelength of 635 nm [9]. Thus, propagation of light passing through the flow field around flight vehicles is closely related to the density of the flow field. Therefore, the aero-optical phenomena occur due to the variation in the density of the flow field around flight vehicles. The aero-optical phenomena are also closely related to the wavelength of the propagating optical wave. The amount of optical aberration increases as the wavelength

decreases; thus, the aero-optical phenomena occur more in the visible region, rather than the infrared region [10].

The propagation of light through a medium is governed by Maxwell's equation. However, if the light propagates through a medium where the length scale is much greater than the wavelength of the light, the propagation of light can be described using geometrical optics [11], also known as ray optics [12]. In ray optics, the propagation of light is described with the location and direction of the rays, which is governed by the following ray equation:

$$\frac{\mathrm{d}}{\mathrm{d}s}\left(n\frac{\mathrm{d}\vec{r}}{\mathrm{d}s}\right) = \bigtriangledown n, \tag{1.2}$$

where s is the distance along the ray path, r is the position of the ray, and n is the index of refraction. Because the smallest length scale of the flow feature is usually greater than the wavelength (0.1 to 1.0 μm), ray optics can be adopted to understand the physics of the aero-optical phenomena. Thus, in this dissertation, ray optics is adopted to explain the optical characteristics. The optical characteristics of the light are usually described with the wavefront of the light, where the normal vectors are the rays, as illustrated in Fig. 1.3. Furthermore, the wavefront can be expressed as the surface with a coincident optical path length (OPL):

$$\mathrm{OPL} = \int_{\mathrm{A}}^{\mathrm{B}} n ds. \tag{1.3}$$

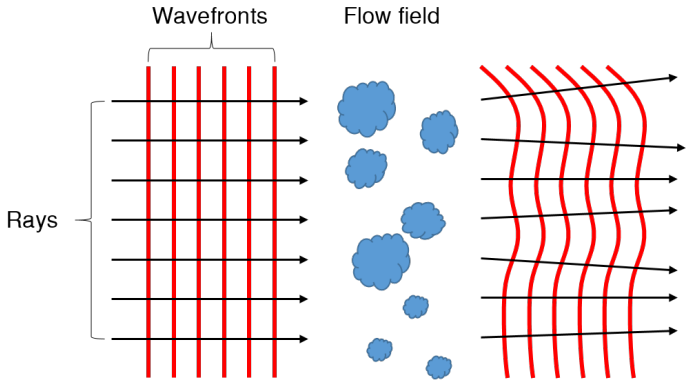

Figure 1.3: Schematic of wavefronts and rays propagating through the flow field.

Because the refractive index is reciprocal to the speed of light within the medium, the OPL is proportional to the time ray traveling from position A to B. Thus, the same OPL means that the rays traveled at the same time. If the refractive index along the rays is known, the wavefront of the light can be acquired from Eq. 1.3. However, because optical aberration due to the flow field is more relevant to aero-optics, the optical path difference (OPD) is more commonly used to describe the optical characteristics. The OPD is defined as follows:

$$\mathrm{OPD} = \mathrm{OPL} - \overline{\mathrm{OPL}}, \tag{1.4}$$

where the $\overline{\mathrm{OPL}}$ is the spatially averaged [13]. The OPD is usually normalized with the wavelength of the light, λ. Larger OPD value means bigger distortion on the wavefront due to the flow field. The overall optical distortion is usually quantified with representative val-

ues, which are the peak-to-valley OPD (PV OPD) and root means square of the OPD (OPD_{rms}). Moreover, PV OPD is the difference between the maximum and minimum of the OPD, which provides information regarding the overall distortion. In addition, OPD_{rms} indicates the difference in the OPD within a wavefront, which is usually representative of the distortion due to the turbulence of the flow.

The far-field pattern of the OPD is also investigated Since because the wavefront, which is aberrated due to the flow field near the flight vehicle, propagates further, the far-field pattern of the OPD is also investigated. Usually, the aberration due to the atmosphere is neglected, and the wavefront is assumed to propagate the free space for an infinite distance to acquire the far-field pattern. This far-field pattern can be calculated using the Fourier transform. Assuming that the incident OPD of the light is all zero at the wavefront, the far-field pattern of the OPD of the aberrated wavefront can be considered as a point spread function (PSF).

From this PSF, boresight error (BSE), blurriness, and the Strehl ratio can be defined. The boresight error is defined as a displacement of the peak position of the PSF. Blurriness is defined as an area of a circle containing the same intensity of light, and the Strehl ratio is defined as the ratio of the peak intensity of the aberrated and diffraction-limited PSF. The boresight error is related to the displacement of the subject in the image. Blurriness is related to the clearness of the subject in

the image, and the Strehl ratio is related to the overall performance of the optical system.

Optical parameters that are important for seeker operation are the line of sight (LOS), wavelength, and exposure time. The LOS is defined as the angle between the axis of the seeker and the axis of the optical sensor. As the attitude of the interceptor and position of the target changes, the LOS changes during flight. However, if the LOS changes, the optical path differs, and the aero-optical effects vary. Thus, investigating aero-optical effects depending on the LOS is important for the data calibration and mission profile. If possible, the LOS with fewer aero-optical effects should be chosen for the mission. The wavelength of the optical sensor differs from visible to infrared, depending on the mission. However, as mentioned, aero-optical effects increase as the wavelength decreases. Finally, the exposure time of the optical sensor affects the quality of the image. If the exposure time is long, the image is blurred, whereas, if the exposure time is low, a small-scale flow structure appears in the image, and the intensity of the image decreases. In this dissertation, only aero-optical effects due to the LOS are studied while the wavelength and exposure time are fixed.

1.3 Previous Studies

Myriad studies on aero-optics have been conducted since the 1950s [10]. Many of these studies were focused on the aero-optical effects due to the turbulent boundary layer or flow field around laser turrets. Studies on the turbulent boundary layer primarily modeled the related equations linking the turbulent property with optical characteristics. Laser turrets have been extensively studied by the Air Force Research Laboratory (AFRL) [8, 14] and the Aero-optics group at the University of Notre Dame [15–17]. The application of the laser turret is usually subsonic or transonic, rather than supersonic. Thus, the fluctuation due to the boundary layer, shear layer, and vortex is the main interest in these studies, whereas aero-optical effects due to shock waves are less considered. Several flight tests have also been conducted to study aero-optical effects around laser turrets. The methods to study aero-optics in the early era were primarily statistical approaches. As the techniques for laser and optical measurement advanced, faster and higher resolution acquisition became available. Furthermore, as the computational techniques advanced, numerical methods have been developed to study aero-optical effects. In the following sections, the previous studies on the supersonic turbulent boundary layer and flow field, including shock waves, are described. Then, the experimental and numerical methods to quantify aero-optical effects are introduced.

1.3.1 Aero-optical effects due to the supersonic turbulent boundary layer

Optical degradation due to the random fluctuation of the density was studied for the supersonic turbulent boundary layer to correlate the turbulence properties and optical characteristics. Stine and Winovich [18] measured the intensity of the light penetrating through two boundary layers over a flat plate in a wind tunnel and analyzed the scattering of the light. The Mach number ranged from 0.4 to 2.5, and the boundary layer thickness differed from 38.1 mm to 88.9 mm. This study revealed that the loss of the intensity of light is related to the integral length scale and intensity of the density fluctuation. Furthermore, the measured maximum scattering angle due to the boundary layers was 0.0006 rad.

Sutton [19, 20] modified earlier theoretical approaches linking atmospheric turbulence and optical characteristics to analyze the aero-optical effects numerically due to the turbulent boundary layer. As the aperture size is different relative to the length scale of the turbulence, the resolution increased beyond the limit that existed in the previous relationship as the aperture decreased. In this study, the linking equation between the turbulence property and aero-optical effects was derived for the first time.

Elghobashi and Wassel [21] mathematically analyzed optical degra-

dation due to the supersonic boundary layer, which interacts with subsonic or supersonic cooling jets. This study mathematically modeled the turbulent heat transfer in the boundary layer or shear layer and predicted the optical phase variance due to the flow field. The predicted density is validated with experimental data, whereas the aero-optical effects due to the boundary layer were not directly validated with experimental measurements.

Tromeur et al. [11, 22] numerically validated Sutton's linking equation by conducting a large eddy simulation and calculating optical characteristics through this flow field. The simulations were conducted for two Mach numbers, 0.9 and 2.3, and the phase variance calculated using Sutton's linking equation was different from the simulation. These studies concluded that the assumption of Sutton's linking equation that the turbulent boundary layer is homogeneous and isotropic should be questioned, and the accuracy of the equation is limited.

Gordeyev et al. [23, 24] measured optical distortion due to the supersonic turbulent boundary layer and developed a new model to link the turbulent properties and optical phase variance. Furthermore, in this study, the small, turbulent scale has a less aero-optical effect in supersonic compared to subsonic boundary layer. However, because the experiment was only conducted for Mach number 2, the new linking model should be validated for other Mach numbers.

Gao et al. [25–27] studied the aero-optical effects due to the Mach 3 turbulent boundary layer by measuring the tilt of the laser beam and quantifying the refractive index using nanoparticle-based planar laser scattering (NPLS). From the measured tilt results, the correlation between the tilt along two directions was statistically analyzed. The correlation was strong for small-beam apertures, whereas it was weak for large-beam apertures, which was concluded due to the hairpin vortex structure of the boundary layer. From the measured refractive index result, Sutton's linking equation was evaluated, and if the turbulent flow was inhomogeneous, the integral length scale calculated based on methods of Wang et al. [13] was more reasonable. Furthermore, Gao proposed a model for the two-dimensional (2D) power spectrum of the OPD, which could be used to generate the 2D OPD from the basic flow parameters.

Ding et al. [28–30] also measured the density of the supersonic turbulent boundary layer using the NPLS technique and evaluated Sutton's linking equation and studied the effect of the turbulence length scale on aero-optical effects. Similar to Gao, an integral length scale calculated based on Wang's method was more reasonable for the inhomogeneous turbulent flow. From the 2D density result, a turbulent length scale was extracted, and each aero-optical effect was calculated numerically. The results demonstrated that small, turbulent length scales have small aero-optical effects. Furthermore, Ding also studied

optical degradation due to the supersonic cooling film [31]. The cooling film was injected into the Mach 3 nozzle flow. In this study, the wavefront was measured using the BOS technique. As the density of the nozzle flow and cooling film increased, the optical distortion also increased.

Throughout the previous studies, the relation between the turbulence of the flow and the optical characteristics was primarily studied, focusing on the linking equation. Thus, the random fluctuation of the optical characteristics has been studied more, and less effort has been made regarding the overall deflection due to the boundary layer. Although Gao et al. [25] presented the deflection due to the boundary layer, the experiment was conducted only for the LOS perpendicular to the boundary layer.

1.3.2 Aero-optical effects due to shock waves

Aero-optical effects due to shock waves are usually studied with the boundary layer because it is difficult to separate each effect. However, several studies have measured the deflection of the beam only for the shock wave [32] or have calculated the aero-optical effect only for the shock wave using numerical methods [33, 34].

Kiefer and Manson [32] measured the angle of refraction of a narrow laser beam that propagated through a moving shock wave gener-

ated by a shock tube. They neglected the aero-optical effects caused by boundary layers because of the rarefied gas flow inside the shock tube. This study focused on the development of the experimental methods to measure the shape of the shock front. In this study, the refraction calculated using Snell's law was quite a coincidence with the measured results.

Banakh et al. [33, 35] modeled a series of phase screens from the supersonic flow field around the conical model and computed the propagation of the optical beam through these phase screens. The boundary layer around the conical model was neglected during the computation. The simulation result indicated that the shock wave acted as a focusing lens, which distorted the distribution of the intensity of the laser beam.

Sun et al. [34] computed the propagation of the optical wave through an oblique shock wave using ray-tracing computation. The computed refraction angle was compared with the refraction angle calculated using Snell's law, and the results were coincident.

Other studies have investigated aero-optical effects due to the shock wave and boundary layer together. These studies have analyzed the flow field around a compression ramp [36, 37], a wedge [38], or an ogive body [39–48].

Xu et al. [36] computed scattering caused by turbulence by solving

the scattering potential integral equation. Using this approach, aero-optical effects on a laser propagating through the turbulent boundary layer over a weak compression ramp were investigated.

White and Visbal [37] numerically studied the distortion of the wavefront caused by interactions between the shock wave and boundary layer in the supersonic compression ramp flow. Using about 340 million cells, turbulent eddies in the boundary layer were demonstrated with high resolution. The results revealed that a turbulent boundary layer made a random tip in the OPD, whereas the general slope of the OPD was primarily affected by the shock wave.

Gordeyev et al. [38] used a Malley probe to acquire the deflection angle spectrum of the laser beam propagating through an oblique shock wave and a turbulent boundary layer around a wedge model. In addition, Frumker and Pade [39] used commercial flow-simulation software and ray-tracing software to evaluate the modular transfer function for a Mach 2 flow field over the spherical dome. This study focused on the establishment of numerical methods for aero-optics, but it indicated that aero-optical effects are not neglectable when a high-resolution image is needed.

Sorrente et al. [40] conducted a Reynolds-averaged Navier-Stokes (RANS) simulation of the flow field around an ogive body and solved the ray equation to quantify the aero-optical effects. The tilt dom-

inated the simulated wavefront, which was maximum at the lowest LOS. Furthermore, the tilt decreased significantly for the lowest LOS as the Reynolds number increased.

Chen and Fu [41] measured the transient wavefront of the laser beam propagating through the Mach 2 flow field over an ogive body. As the flow developed, the pattern of the wavefront varied, but when the flow was established, the wavefront became stable. When the wavefront became stable, a circular pocket appeared at the center of the laser beam.

Yi et al. [42] measured the density around the ogive body using NPLS techniques and traced the rays through this measurement result. This study presented how the OPD changes as it propagates through the flow field. It demonstrated how the OPD changed as the ray passes through the shock wave and boundary layer, but the aero-optical effects between these two flow features were not strictly compared. In addition, the ray-tracing result depending on the resolution of the density measurements was analyzed, and as the resolution decreased, the small-scale structure disappeared in the OPD result, whereas the overall pattern of the OPD remained.

Xiao et al. [43] studied the aero-optical effects numerically in a spherical dome with a very small LOS, almost near the axis of the body. This could be performed because the window was assumed to

be at the front of the body, whereas other studies have assumed the window was on the side of the body. Three different LOSs were calculated, and as the LOS departed from the axis, the distortion of the shape of the wavefront increased, and the scattering in the PSF also increased.

Hao et al. [44, 45] conducted research similar to that by Xiao, but with a different shape of the window at the top of the body. Three window shapes were investigated: spherical, ellipsoid, and paraboloid. The ellipsoidal shape has the smallest aero-optical effects, while the spherical shape had the largest aero-optical effects. Furthermore, the aero-optical effect due to the angle of attack (AOA) of the body was investigated, where the distortion increased as the AOA increased. The ray-tracing computation to study the aero-optical effects was based on the shape of an optical window installed on a blunt body.

Liu et al. [46] conducted a ray-tracing computation on the supersonic flow field around a blunt-nosed model and studied the optical transmission through the aerodynamically heated window. Using the PSF of the simulated aero-optical effects, the image seen by this flow field was simulated with true Infra red images. The images were blurred when the aero-optical effects were convoluted.

Yao et al. [48] numerically simulated the flow field over the spherical dome, and Hao and Xiao and studied the deviation of the image

depending on the LOS. The LOS varied from 0°to 90°, and the image deviation decreased as the LOS increased. The image deviation changed more significantly depending on the LOS when the LOS angle was below 40°.

he deflection of the rays due to the shock wave seems to follow Snell's law as reflected in previous studies considering only the shock wave. Few studies have compared the aero-optical effects due to the shock wave and turbulent layer, instead investigating the overall aero-optical effects due to both flow features. Moreover, most of the studies on supersonic shock waves and boundary layers were conducted for the ogive body, rather than the compression ramp or wedge. Therefore, the aero-optical effects due to shock waves were complicated, and the wavefront distortion appeared in a complex shape due to the three-dimensional (3D) effects of the flow. Furthermore, aero-optical effects are primarily quantified using numerical methods rather than direct experimental measurements.

1.3.3 Aero-optical effects due to hypersonic flow

Compared to subsonic or supersonic flows, few studies have been conducted for aero-optical effects due to hypersonic flow. Because the available experimental time for hypersonic is far less than supersonic, developing measurement techniques with a high frame rate had been

a top priority. Therefore, many studies have focused on establishing experimental methods to quantify aero-optical effects in hypersonic flows. Aero-optical effects due to hypersonic flow had been studied only recently.

Tropf et al. [6] numerically simulated the aero-optical effects due to the hypersonic flow field around the blunt body. Depending on the LOS, the BSE was simulated. Similar to the supersonic flow result of Yao et al. [48], the BSE decreased as the LOS increased.

Hedlund et al. [49] conducted experiments using a hypervelocity wind tunnel to measure aero-optical effects due to the hypersonic flow field around the conical forebody. The blur diameter and BSE were measured for several LOSs, where the aero-optical effects decreased as the LOS increased. The measured BSE was in several hundred μradians.

The Arnold Engineering Development Center (AEDC) [50, 51] established an aero-optics measuring system using a hypervelocity wind tunnel. Yanta et al. [52] used this measurement system and studied the aero-optical effects due to the hypersonic flow around a wedge. The transient BSE and Strehl ratio were presented for several test conditions. The BSE was about several tens of μradians. Various optical measurement methods were adopted to evaluate the measurement uncertainties, facility errors, and instrument errors.

Moreover, Calspan-UB Research Center (CUBRC) [53–55] also established a measurement system for aero-optical research in hypersonic flow using the Large Energy National Shock Tunnel (LENS). The validation of the measurement system was conducted using a flat plate, 2D wedge, and 3D triconic model. For the triconic model, the aero-optical effects due to a coolant jet were also investigated. Using these experiment data, Sutton et al. [7] validated their numerical simulation methods. The numerical calculation was different from the measurement of the BSE, which error was about 50%.

Wyckham and Smits [56] studied the turbulent effect in the hypersonic boundary layer. This study was first to relate turbulent properties to optical characteristics in hypersonic flow using experimental methods. Sutton's linking equation was evaluated and modified for the hypersonic condition.

Xu and Cai [57] analyzed imaging deviation depending on the altitude at over 10 to 60 km for a Mach 3 and 6 flow field over an ogive body. The flow simulation was conducted by solving the RANS equation, and the rays propagating through this flow field were computed by solving the ray equation. As the altitude decreased, the imaging deviation increased due to the smaller density changes in higher altitudes.

Ren and Liu [58] analyzed the effect of the Knudsen number and

the compressibility in the hypersonic flow around a spherical body. The optical distortion increased as the Knudsen number decreased. For supersonic flow, the optical distortion decreased as the Mach number increased, whereas, for hypersonic, it was the opposite.

Gordeyev et al. [59, 60] studied the deflection spectrum of the laser beam when the transition occurred in the hypersonic laminar boundary layer. From the measurement, transition structures were well observed.

Mackey and Boyd [61] studied the nonequilibrium effect on aero-optics with numerical simulation. The OPD was compared for the perfect gas assumption and the thermochemical nonequilibrium assumption, but the difference was not great. However, as the Mach number increased, the difference between these assumptions increased. Thus, the nonequilibrium effect on aero-optics is greater in a higher Mach number flow.

Zhao et al. [47] measured the wavefront of the laser beam propagating through a blunt body with a coolant film over the window. The results revealed that, as the pressure of the coolant film increased, the optical distortion also increased.

Studies on hypersonic flow have predominantly focused on the establishment of experimental methods, which is more difficult than supersonic experiments. The aero-optical measurement system for hy-

personic flow has been established for several institutes, but few experimental results have been presented. Several studies have investigated the nonequilibrium effect or Knudsen number effect in hypersonic flow. Thermochemical nonequilibrium does not seem to have much effect on optical degradation, whereas the Knudsen number has some effect on optical degradation.

1.3.4 Experimental methods for the aero-optics study

Experimental investigations have been conducted. These investigations used the laser-schlieren technique [32], a Malley probe [62–65], a Shack-Hartmann wavefront sensor (SHWS) [52, 66], the laser-induced breakdown method [67], the BOS method [47, 68, 69] and the NPLS technique [28, 30, 42].

The laser-schlieren technique [32] propagates a narrow laser beam with a diameter of 0.8 mm through the test section and measures the position of the laser beam using a photodiode. Using a rotational mirror, photodiode data are calibrated with the angle of the laser beam, and the transient refraction angle can be acquired from photodiode data.

Similar to the laser-schlieren technique, the Malley probe [62] measures the jitter of a laser beam and reconstructs the wavefront assuming Taylor's frozen flow hypothesis. The Malley probe is also known as

a small-aperture beam technique (SABT), and Jumper et al. [63–65] validated the technique by comparing the reconstructed OPD with a simulation result for a 2D heated jet. The reconstructed OPD and simulated OPD were quite coincident.

From the Shack-Hartmann principle, the SHWS was developed with a micro-lenslet array and charge-coupled device (CCD) [66]. The SHWS could acquire a 2D near-field wavefront, which was difficult with other measurement techniques. A laser beam with a certain diameter propagates through the test section, and the SHWS measures the wavefront of this laser beam. Yanta et al. [52] had validated the performance of the SHWS by comparing it with other optical sensors. Furthermore, PSF converted from the measured OPD was validated with the measured PSF and demonstrated that these results are similar. Thus, the SHWS could be used to evaluate near-field aero-optics and far-field aero-optics simultaneously.

The laser-induced breakdown method [67] generates a spark in the middle of the flow field and measures the wavefront of this spark. This method was developed for a flight test, where a laser beam cannot be generated as easily as in the ground tests. The aero-optical effects due to motion of the spark itself could be removed, and the capability of this method for aero-optical measurement was proved.

The BOS method [47, 68, 69] converts BOS images to wavefront

slopes and reconstructs the wavefront, similar to the SHWS. As the BOS does not require a lenslet array, the aero-optical effects could be studied for a large area. Furthermore, the hardware less expensive than the SHWS, whereas more computation is needed for postprocessing.

The NPLS technique [28, 30, 42] measures the density of the flow field, and ray-tracing is performed to study the aero-optical effects. Thus, it is different from previous optical measurement techniques and indirectly quantifies the optical properties. However, the NPLS technique can easily relate the flow properties to the optical characteristics because it obtains the data simultaneously. Moreover, other optical measurement techniques require an additional flow visualization system to acquire the flow information, and in most cases, the simultaneous acquisition of the flow visualization technique and optical measurement is difficult due to the test section configuration.

The SABT technique could acquire high-frequency data; however, acquiring 2D OPD is challenging. Furthermore, in modern studies, the SHWS or BOS method is widely used to quantify the wavefront directly. The NPLS technique is appropriate to relate the flow field property and optical characteristics but is an indirect optical measurement method. Thus, analyzing both direct optical measurement data and the NPLS techniques seems to be favorable for aero-optics study. However, the hardware for the NPLS technique is complicated,

and establishment seems to be difficult. Thus, an alternative method for flow density acquisition, such as the BOS-based method, seems appropriate.

1.3.5 Numerical methods for the aero-optics study

As information obtained from experimental methods is limited, numerical methods have been adopted to investigate the aero-optical effects in supersonic flow fields. Such simulations are usually conducted by acquiring the density of the flow field numerically, converting the density to the index of refraction, and calculating the propagation of the optical wave. Several numerical methods have been adopted to simulate the propagation of the optical waves.

Banakh et al. [33] modeled a series of phase screens from the supersonic flow field and computed the propagation of the optical beam through these phase screens. Between the phase screens, only the diffraction of the waves is considered.

Xu et al. [36] computed scattering caused by turbulence by solving the scattering potential integral equation. Several researchers have neglected the deflection of rays and acquired the wavefront of the optical beam by integrating the index of refraction along a straight line [11, 22, 37]. This was valid because the refractive index slightly changes in the air, and the refraction angle is neglectable. This numer-

ical method has the lowest computation cost. Other studies assumed that refraction or reflection occurs only at the edges of the computational cells used for the flow field calculation, and Snell's law was used to calculate the refraction angles at those edges [34, 70].

Sun et al. [34] computed the propagation of the optical wave through an oblique shock wave using ray-tracing computation and validated the computational result with the refraction angle calculated using Snell's law. In this method, an additional grid for optical calculation is not needed, and computational cells for flow simulation could be directly used. The propagation of the optical wave through a flow field has also been simulated by solving the ray equation numerically [39, 40, 44, 46, 47, 71]. The ray equation is solved using the Runge-Kutta method or commercial software. The computational cost of this method is high relative to other methods. However, if geometrical optics is valid, this method is most reliable.

The ray-tracing method, which solves the ray equation, is the most common numerical method used for aero-optics. However, due to the computational cost, methods such as straight ray computation are used often. However, the accuracy of this method should be evaluated because the path of the ray is different. The numerical method provides more information on aero-optical effects, and the flow field could be more easily investigated than experimental methods, but numerical methods should always be validated with the experimental results.

1.4 Objectives

Shock waves and boundary layers are inevitable aerodynamic features in the flow field around a seeker flying at supersonic or hypersonic speed. Thus, studying the aero-optical effects due to these flow features is important. The previous studies have investigated the aero-optical effects for these aerodynamic features but focused on the turbulence of the flow field, which induces random aberrations on the wavefront of the optical wave. Furthermore, few studies have investigated the deflection due to the boundary layer, and none of the studies compared the deflection due to shock waves and boundary layers. Moreover, few studies have investigated the aero-optical effects due to hypersonic flow.

Thus, in this dissertation, aero-optical effects due to shock waves and boundary layers are compared in supersonic and hypersonic flow. For the supersonic flow regime, the flow field over a 2D compression ramp is studied, and for the hypersonic flow regime, the flow field over a 2D wedge is studied. The aero-optical effects are studied by adopting both experimental and numerical methods. With only the experimental methods, the information that can be uncovered is limited, and comparing the individual contributions to the aero-optical effects due to shock waves and boundary layers is difficult. However, with only numerical methods, more information can be discovered than experi-

mental methods, but the validation of the numerical methods is always questioned.

Furthermore, the boundary condition, initial condition, and computational domain for numerical methods could be set up correctly when the procedures and conditions of the experimental methods are sufficiently known. Thus, to understand the aero-optical effects induced by shock waves and boundary layers, it is necessary to conduct numerical and experimental methods simultaneously. However, few studies have conducted both numerical and experimental methods simultaneously. Therefore, this dissertation also aims to demonstrate the importance of conducting both experimental and numerical methods simultaneously.

Before investigating supersonic and hypersonic flow, the fundamentals of aero-optics are studied in a subsonic heated jet. In this jet flow, the wavefront measurement system based on the SHWS, which is also used for supersonic and hypersonic flows, is established. Furthermore, a new experimental method based on the BOS method is suggested and evaluated in a subsonic heated jet flow.

After the experiments in subsonic heated jet flow, the aero-optical effects due to the shock wave and boundary layer are investigated for the supersonic flow field. The wavefront measurement method established in the subsonic heated flow is applied for the supersonic ex-

periment. Because the result of the SHWS involves both aero-optical effects caused by both the shock wave and the boundary layer, a ray-tracing computation is conducted to obtain the wavefront numerically to identify the individual contributions of the shock wave and boundary layer. The flow field required for ray-tracing is obtained from a numerical simulation by solving the RANS equations. Then, the propagation of optical waves through this flow field is computed by solving the ray equation.

The numerical result is validated with the experimental result, and from the numerical result, the aero-optical effects in the middle of the flow are analyzed. Using an approach similar to that used for the supersonic flow field, the aero-optical effects due to the shock wave and boundary layer in the hypersonic flow field are studied. Additionally, the aero-optical effects due to the flow field around the ogive nose cone model are investigated for hypersonic flow.

Chapter 2

Experimental Methods

In this chapter, the experimental methods used in the dissertation are introduced. In the first part of the chapter, the experimental facilities used to generate the flow fields are reviewed. Information on the supersonic wind tunnel and hypersonic shock tunnel is described. In the second part, the test model and configuration of the experiments are presented. The test configurations for the three flow regimes, which are subsonic heated flow, supersonic flow, and hypersonic flow, are described. In the final part of the chapter, the methods for data acquisition during the experiment are discussed. The flow visualization techniques and optical system for the wavefront measurement are presented.

In this chapter, the experimental setup for the supersonic flow

was presented at the 30th International Symposium on Shock Waves (ISSW) [72], and the experiment setup and facility for the hypersonic flow were presented at the 30th and 31st ISSW [73, 74]. The design and validation of the hypersonic-contoured nozzle were presented at the 2014 KSPE fall conference [75].

2.1 Experimental Facility

2.1.1 Heated subsonic jet

To establish the measurement system for the aero-optical experiments, a preliminary study of the aero-optics was conducted on the subsonic heated jet. The heated subsonic jet was adopted because the density of the cold flow ($T_0 \sim 300$ K) is not that different from the atmosphere, resulting in little aero-optical effect. Thus, to intensify the aero-optical effect and easily measure the aberration of the wavefront, the flow must be heated. A commercial heat gun (Steinel, HG2310LCD) with a controllable flow rate and temperature was used to generate the heated subsonic flow. The airflow rate can be set to 102 to 498 L/m, and the temperature can be controlled to between 322 and 922 K. The nozzle of the heat gun is depicted in Fig. 2.1, where Fig. 2.1(a) is the front view of the nozzle exit, and Fig. 2.1(b)) is the schematic of the nozzle. The outer diameter of the nozzle is 34 mm, and the diameter of the nozzle exit is 22 mm. As illustrated in Fig. 2.1, six vanes are located at the exit of the nozzle, which efficiently mix the

temperature of the flow.

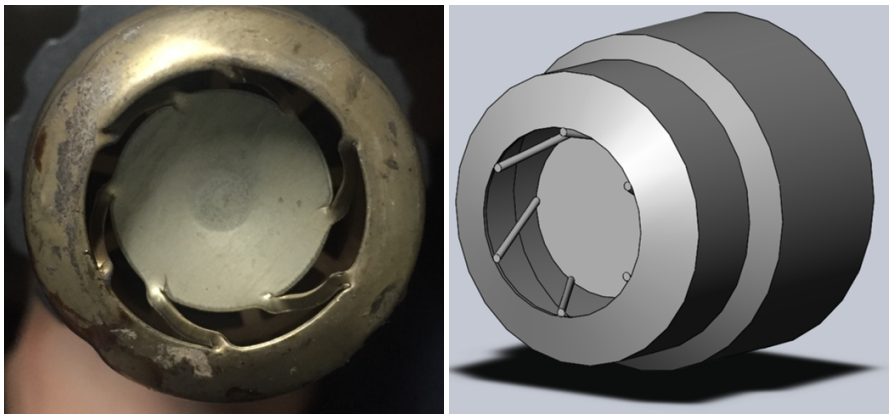

(a) (b)

Figure 2.1: Nozzle of the heat gun for the subsonic experiment; (**a**) front view of the exit and (**b**) schematic.

2.1.2 Supersonic windtunnel

Experiments to investigate the aero-optical phenomenon in the supersonic flow field over a compression ramp were conducted with a supersonic wind tunnel at Seoul National University. The picture of the supersonic wind tunnel used for the experiment is presented in 2.2. The supersonic wind tunnel comprises an air compressor, dryer, high-pressure tank, on/off valve, control valve, settling chamber, test section, diffuser, and dump tank. The air compressor compresses atmospheric air and sends it to the tank through the dryer, which reduces the humidity of the compressed air. The air inside the tank can be compressed to 3 Mpa, and the compressed air is blocked by the

on/off valve. When the supersonic wind tunnel operates, the on/off valve suddenly opens, and the pressure inside the settling chamber can be manually controlled by the control valve. The pressure inside the settling chamber is measured using an analog pressure gage and pressure sensor, which records the data during the experiment. A screen is installed inside the settling chamber to reduce the turbulence intensity before entering the test section. The air inside the settling chamber accelerates to supersonic by the nozzle and enters the test section.

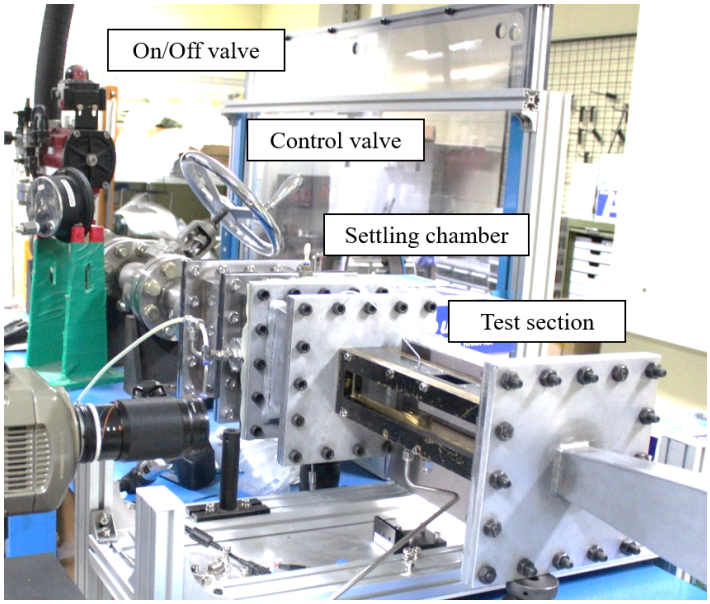

Figure 2.2: Supersonic wind tunnel for investigation of the aero-optical phenomenon in a supersonic flow.

For the experiment in this dissertation, a closed-type test section configuration was adopted to avoid the shear layer at the exit of the nozzle and to generate a thick boundary layer. In this configuration,

the nozzle, compression ramp, and test section were integrated, as depicted in Fig. 2.3. The designed Mach number of the half-contoured nozzle is 2, and the throat height is 17.2 mm. The height of the exit of the nozzle and the inlet of the test section were both 30.7 mm, whereas the width was 30 mm. The height of the exit of the test section was 36.7 mm. Windows are installed on each side of the test section to view the flow. After the test section, the air passes through the diffuser and finally enters the dump tank. The test time using this facility is about several minutes, which is sufficient to acquire several images of the wavefront during the operation of the wind tunnel.

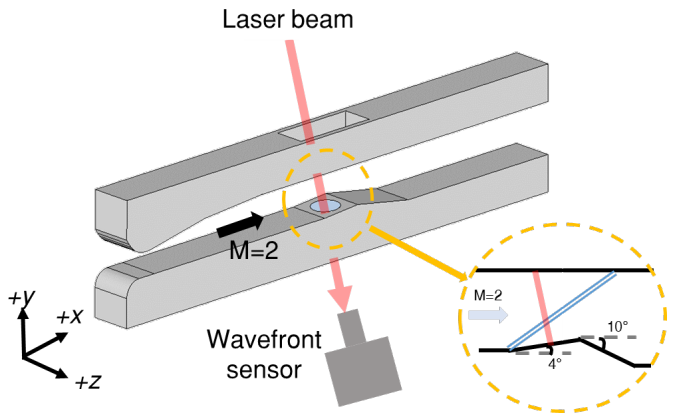

Figure 2.3: Configuration of the test section for the supersonic experiment and the optical setup for the aero-optical measurement.

2.1.3 Hypersonic shock tunnel

The experiments for the aero-optical phenomenon in the hypersonic flow were conducted using a shock tunnel at Seoul National University. Figure fig:AST2 is the illustration and picture of the shock tunnel used for the experiment, which is called the Aerospace Propulsion and Combustion Laboratory Shock Tunnel 2 (AST2). The AST2 comprises a boosting system, control panel, driver tube, insert, driven tube, nozzle, test section, and vacuum pump. The boosting system pressurizes high-pressure gas inside a cylinder to a higher pressure. Nitrogen or helium can be pressurized using this system. In this dissertation, nitrogen gas was used as the driver gas to increase the density of the flow by lowering the temperature of the gas. The pressurized gas was stored in a storage tank, which can endure up to 45 Mpa.

After the driver gas was pressurized using the boosting system, the vacuum pump was operated to lower the pressure inside the test section for the nozzle flow to expand fully. The pressure of the test section is usually set to 50 Pa to 150 Pa. After the pressure inside the test section was lowered, the control panel was manually controlled to send the gas into the driver tube, insert, and driven tube. Between these three tubes, diaphragms were installed to block the gas until the pressure can reach the operating condition. The material used as a diaphragm is a polyethylene terephthalate (PET) film with differ-

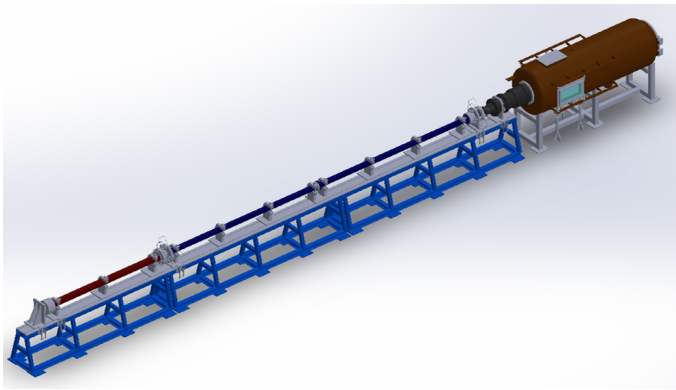

(a)

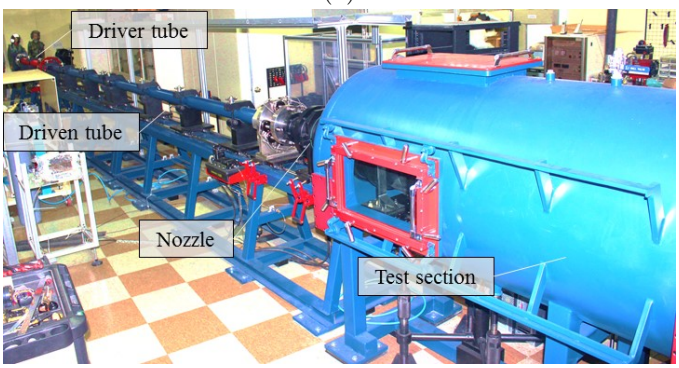

(b)

Figure 2.4: Hypersonic shock tunnel for investigating the aero-optical phenomenon in hypersonic flow: (**a**) overall illustruation and (**b**) side view.

ent thicknesses. Moreover, a diaphragm was located at the throat of the nozzle to reflect the shock wave and achieve a higher stagnation temperature and pressure at the nozzle inlet.

An insert was installed between the driver tube and the driven tube to achieve higher pressure inside the driver tube with the same

thickness as the diaphragm. Usually, the insert is pressurized until half of that of the driver gas. As the pressure inside the driver tube and insert increases, the diaphragms burst, and a shock wave generates and propagates through the driven tube. As the propagated shock wave reflects at the end of the driven tube, the reflected shock wave compresses and heats the driven gas again. Then, the diaphragm at the nozzle throat melts, and the gas inside the driven tube accelerates within the nozzle, and the flow is established inside the test section.

The inner diameter of the tubes is 100 mm, the length of the driver tube is 3 m, and the driven tube is 8.2 m. The drawing of the contoured nozzle, where the exit flow is designed to be Mach 7, is illustrated in Fig. 2.5. The diameter of the throat of the nozzle is 32.03 mm, and the diameter of the nozzle exit is 340 mm. The nozzle was designed based on the methods of characteristics (MOCs) with the correction of the boundary layer. The inviscid nozzle profile was first generated based on the MOCs, and then the flow simulation was conducted to simulate the boundary layer and correct the profile of the nozzle. The inner diameter of the test section is 1.5 m, and the length of the test section is 3 m. To reduce the vibration generated from the burst of the diaphragm and the aerodynamical vibration from the nozzle to be transferred to the test section and model, the tubes and nozzle were installed on a rail to be able to slide during the burst. The duration of the test time differed by conditions, and for the conditions in this

dissertation, the duration was 3 to 5 ms. Because the duration of the test is very short, only one image of the wavefront is acquired during each run, which makes the aero-optical experiments relatively more difficult compared to supersonic flow.

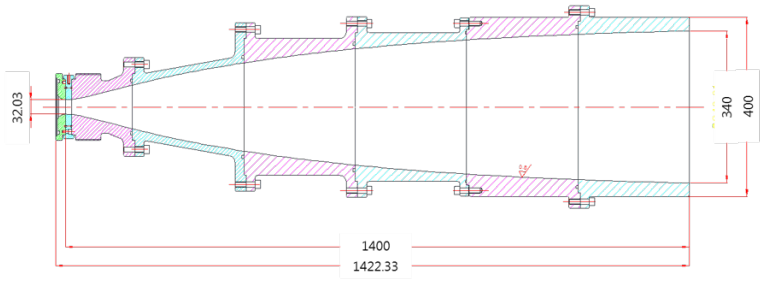

Figure 2.5: Cross-section of the drawing of the Mach 7 nozzle.

Before conducting the aero-optical experiments, the nozzle flow was validated using several tests. First, the Mach number of the nozzle flow was measured by visualizing the oblique shock over the wedge with a known angle. Using the θ-β-M equation, the Mach number of the flow could be calculated from the shock wave angle over the wedge measured from the flow visualization result and known wedge angle. For the test, a wedge with an angle of 10°was installed in the test section, and the oblique shock wave was visualized using the shadowgraph method. The flow visualization result is presented in Fig.2.6. In Fig. 2.6, the transient development of the oblique shock wave is observed. The time for the nozzle flow to be stable was 250 μs, which is 10% of the total test time. The measured shock wave angle when

the steady flow was established over the wedge is 16.4°. From the analytical calculation using the θ-β-M equation, this shock wave angle corresponds to Mach 6.97, which is close to the design Mach number.

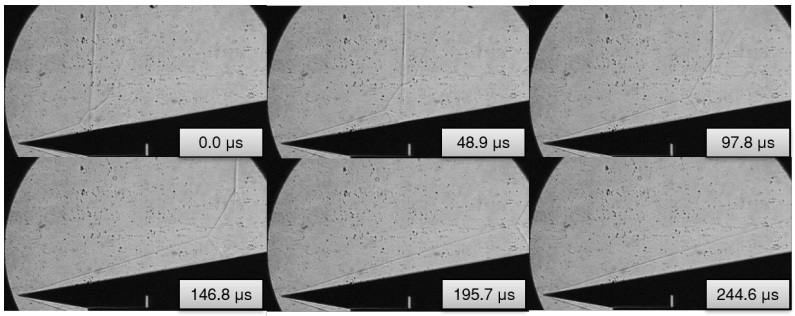

Figure 2.6: Transient oblique shock wave visualized using the shadowgraph method.

NThe nozzle exit flow was further investigated by measuring the total pressure with a pitot rake. The picture of a pitot rake and pitot tubes installed at the nozzle exit is presented in Fig. 2.7. Piezoelectric pressure sensors were installed in each pitot tube. Due to the limitations of the data acquisition system, the pressure at eight points were measured simultaneously. Assuming the nozzle flow is axisymmetric, the pressure was measured for half of the nozzle to increase the spatial resolution of the measurement. Assuming that the isentropic expansion occurred along the nozzle and a normal shock wave formed at the front of each pitot tube, the Mach number along the nozzle exit was calculated from the total pressure measured with the pitot tube

and the total pressure measured at the front of the nozzle inlet. The calculated Mach number and flow-simulation results acquired during the nozzle design process were compared and illustrated in Fig. 2.8. The flow was uniform within a 75% radius, and the experimental and numerical results were coincident in this region. Thus, the nozzle flow is valid within 75% of the nozzle exit radius, and the Mach number of the nozzle exit flow is 7.

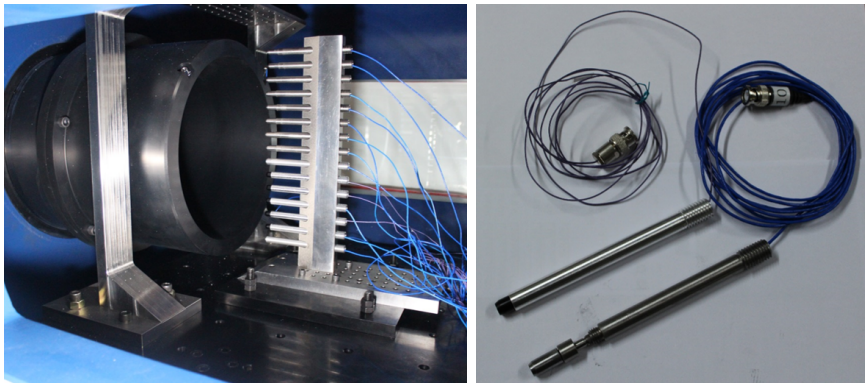

(a) (b)

Figure 2.7: Pitot rake to measure the pressure at the exit of the nozzle: (**a**) pitot rake and (**b**) pitot tube.

2.2 Experimental Configuration and Test Model

2.2.1 Heat gun for the subsonic experiment

The experimental configuration and picture of the setup for the heated subsonic jet are presented in Fig. 2.9. The heat gun was installed on

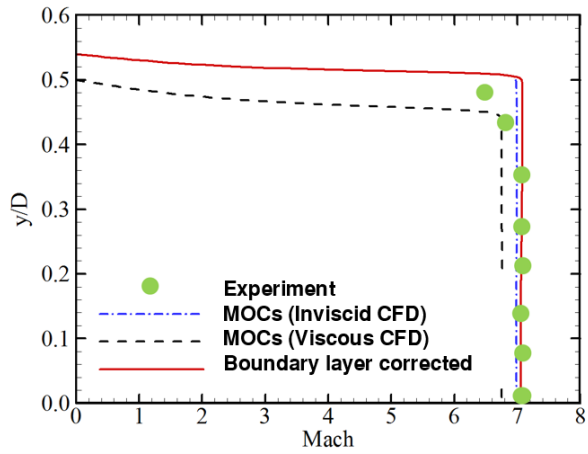

Figure 2.8: Mach number along the exit of the contoured-nozzle designed with the method of characteristics (MOCs).

the optical table where the flow visualization system and wavefront measurement system are installed perpendicularly, as in Fig. 2.9(a). The details of the flow visualization method and wavefront measurement system are described in the following sections. A delay generator (DG-535) was used to trigger the camera for the flow visualization system and the SHWS of the wavefront measurement system to acquire the flow and wavefront data simultaneously. The delay generator produced a 5 V Transistor-Transistor Logic (TTL) signal at a rate of 0.5 Hz. This data acquisition rate is set because this is the maximum frame rate of the camera for the flow visualization system used for the subsonic experiment. The experiments were conducted by setting the heat gun with a temperature to 523 K, and the airflow rate was set to approximately 189 L/min. The surrounding atmosphere of the

heat gun was assumed to be 101,325 kPa and 300 K, which are the room pressure and temperature.

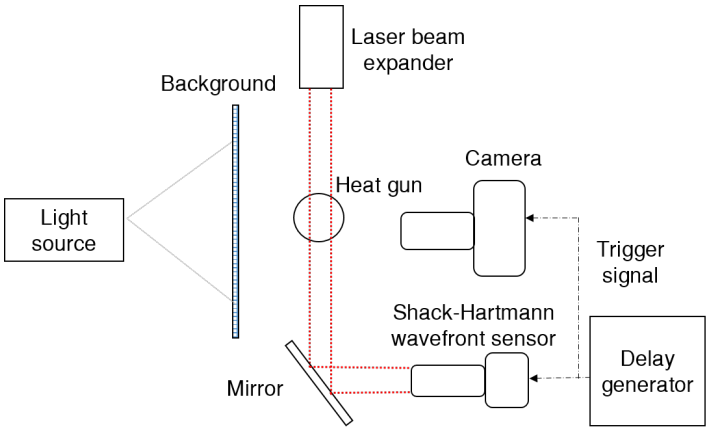

(a)

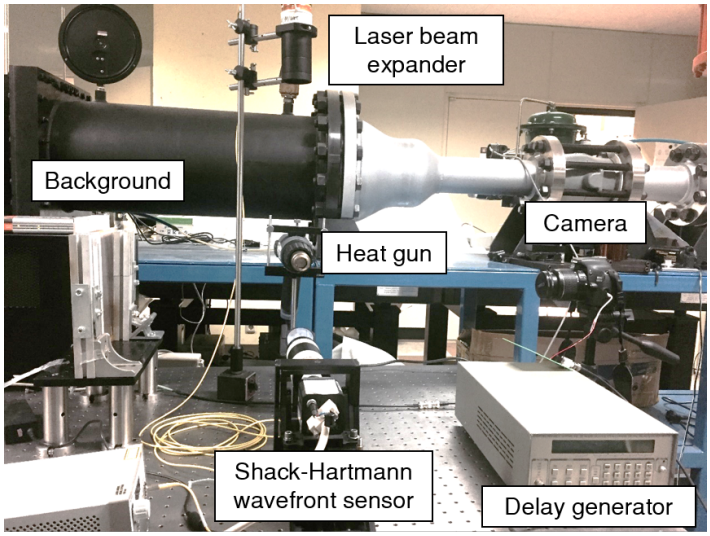

(b)

Figure 2.9: Experimental setup for the heated subsonic flow: (**a**) configuration of the experimental setup and (**b**) picture of the experimental setup.

2.2.2 Supersonic flow over a compression ramp

To investigate the aero-optical effects due to the boundary layer and shock wave, a 2D compression ramp was used for the supersonic experiment, as illustrated in Fig. 2.10. Through the compression ramp, a thick boundary layer was generated over the wedge, and an oblique shock wave was generated from the ramp. The angle of the compression ramp was 4°, which was expected to generate an oblique shock wave with an angle of 33.394°. The angle of the compression ramp was set to 4°because, in a larger angle ramp, the shock train is established over the compression ramp and a complicated flow was established [72]. The width of the compression ramp was 30 mm, which was the same as the width of the test section.

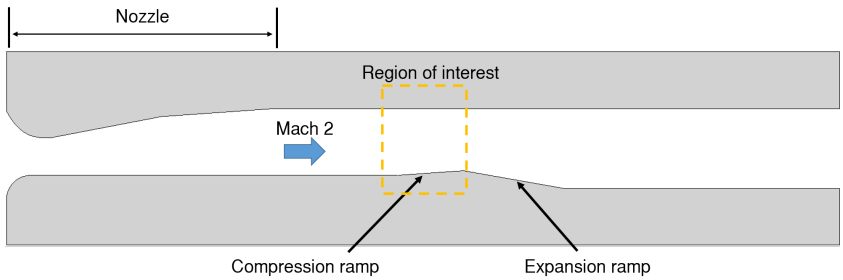

Figure 2.10: Illustration of the compression ramp for the supersonic experiment.

Just behind the compression ramp, an expansion ramp was installed to lower the back pressure and avoid a shock train to be generated over the compression ramp. The angle of the expansion ramp

was 10°. The expansion ramp was extended until the height of the test section became 36.7 mm. The length of the compression surface was 30 mm.

In the middle of the ramp surface, a circular window was installed for a laser beam to propagate through. The diameter of the window was 20 mm. A window on the top plate of the test section allowed the laser beam to propagate into the flow field. The width of the window on the top plate was 30 mm, and the length was 50 mm. The frame rate of the wavefront measurement system was set to 0.5 Hz, which was the same as the subsonic experiment. Similar to the subsonic experiment, this was the maximum frame rate that could be achieved with the camera of the flow visualization system.

The duration of each experiment was around 10 s; thus, about six images could be acquired during each operation. The total pressure of the flow field was set below 1 Mpa, and the total temperature was assumed to be 300 K, which is the same as the atmospheric temperature. For each experiment, total pressure was measured with pressure sensor and the trigger signal generated from the delay generator was recorded through data acquisition system.

2.2.3 Hypersonic flow over a wedge

The experiments concerning the aero-optical phenomenon due to the hypersonic flow field were conducted using a wedge, as depicted in Fig. 2.11. The back view of the test section is illustrated in Fig. 2.11(a) and a detailed view of the wedge and the up-plate are depicted in Fig. 2.11(b). Because the test section type was open, the shear layer established at the exit of the nozzle could have interfered with the laser beam. Thus, in the hypersonic experiment, the up-plate, which is flat, was installed to prevent the laser beam from being distorted due to the shear layer at the nozzle exit. The angle of the wedge was 12°, the width was 150 mm, and the axial length was 330 mm. The width of the up-plate was the same as the wedge, which was 150 mm, and the length of the up-plate was 300 mm. For the laser beam to propagate through the flow field, windows were installed on both the wedge and up-plate. The width of the window installed on the wedge was 40 mm, and the length was 100 mm. The width of the window installed on the up-plate was 45 mm, and the length was 130 mm. The center of the window installed on the wedge was displaced by 200 mm from the tip of the wedge. Behind of the wedge, the pitot rake was installed to identify the state of the flow inside the test section. Using this information, the wavefront measurement system was triggered by the delay generator (DG535) when the steady flow was established inside the test section. Through this trigger signal,

the wavefront measurement system acquired one frame during each operation of the shock tunnel due to the limitation of the maximum frame rate that the wavefront measurement system could achieve. The experimental conditions for the hypersonic experiment are described in Chapter 6.

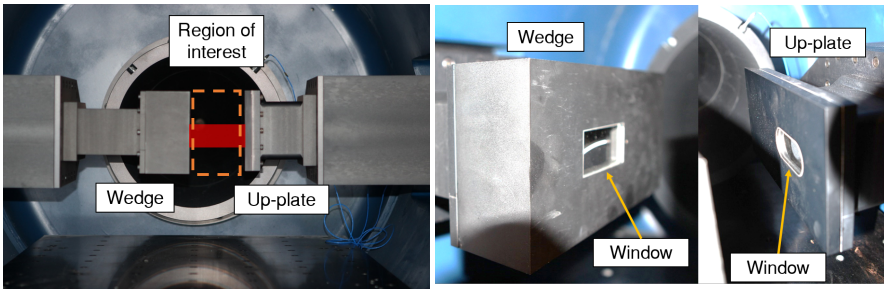

(a) (b)

Figure 2.11: Experimental setup for the hypersonic flow experiment: (**a**) the back view of the test section for the hypersonic flow experiment and (**b**) picture of the experimental setup.

2.2.4 Hypersonic flow over an ogive nose cone

The flow field around the ogive nose cone model and its aero-optical effects were investigated for hypersonic flow. The ogive nose cone model installed in the test section is shown in Fig. 2.12(a)The flow field around the ogive nose cone model and its aero-optical effects were investigated for hypersonic flow. The ogive nose cone model installed in the test section is shown in Fig. 2.12(b). The diameter of the nose is 60 mm. The angle of the cone is 15°, and the maximum diameter

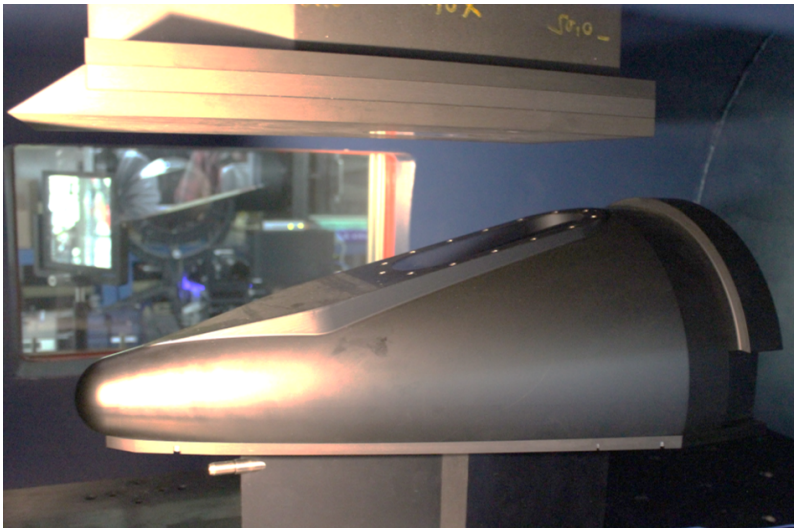

(a)

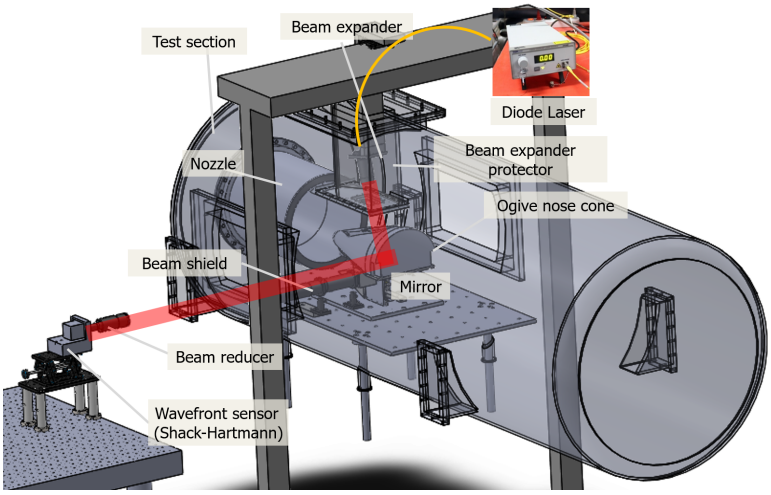

(b)

Figure 2.12: Ogive nose cone model used for the hypersonic experiment: (**a**) ogive nose cone model installed in the test section and (**b**) configuration of the experimental setup.

is 300 mm. To install the model within the uniform flow region of the nozzle, the model was cut in half. As the body is conical, the window must be installed with a window frame, making a disturbance on the flow field. The total length of the window is 177 mm, and the width is 33.5 mm. The material of the window is BK7, which was the same as that for the wedge model. Because the flow field around the ogive body is more complicated than the wedge model, the experimental setup, which could simultaneously visualize the flow and measure the wavefront, was adopted.

The laser beam expander was protected with a shield on top of the test section, which was similar to the up-plate in the hypersonic wedge experiment. The laser beam propagated through the flow field was reflected with a mirror inside the cone model into the SHWS outside the test section. The outgoing laser beam was also protected from the flow field using a beam shield. Similar to the wedge model, the wavefront measurement system was acquired once per each run. A pitot tube was installed below the ogive nose cone model at the strut, and these pressure data were used to trigger the wavefront measurement system.

2.3 Data Acquisition

2.3.1 Flow visualization

Shadowgraph and schlieren techniques

To investigate the flow field, the shadowgraph and schlieren conventional flow visualization techniques were adopted. The configuration of these techniques is illustrated in Fig. 2.13. In the configuration, the only difference is the knife-edge at the focal point. The schlieren technique blocks a certain area of the light at the focal point, whereas the shadowgraph technique installs the imaging lens on the focal point. The schlieren technique visualizes the flow by showing the density gradient of the flow, whereas the shadowgraph technique visualizes the flow by showing the divergence of the density gradient of the flow. The direction of the blocking of the knife-edge is coincident to the direction of the gradient it shows. If the knife-edge blocks in the x-direction, the density gradient in the x-direction is visualized. Thus, the direction of the knife-edge should be selected depending on the characteristics of the flow.

In this dissertation, the schlieren technique was used for the flow visualization of the heated subsonic flow, whereas the shadowgraph technique was used for the flow visualization of the supersonic and hypersonic flow. For the flow visualization of the subsonic and hy-

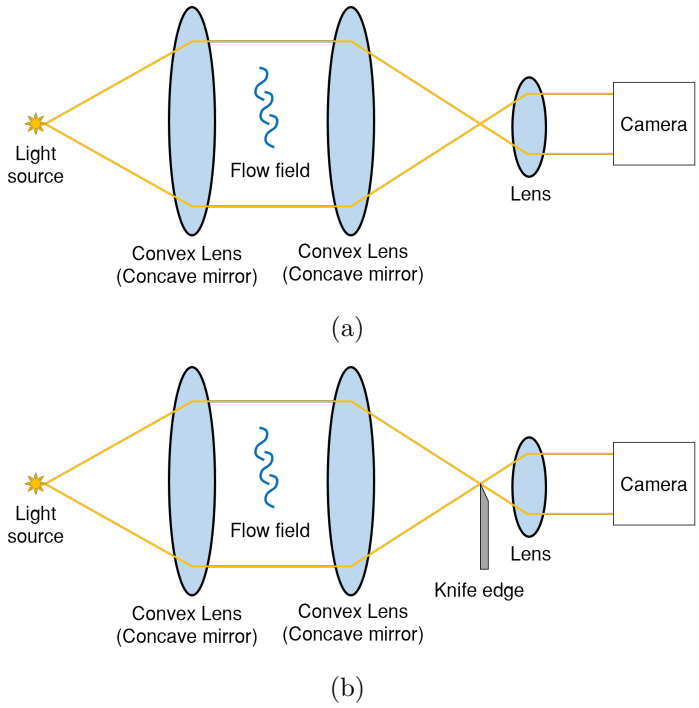

Figure 2.13: Configuration of conventional flow visualization techniques: (**a**) configuration of the shadowgraph technique and (**b**) configuration of the schlieren technique.

personic flow, a concave mirror was used, whereas, for the supersonic flow, a large convex lens was used. The focal length of the concave mirror was 2540 mm, and the diameter was 254 mm, whereas the focal length of the convex lens was 400 mm, and the diameter was 200 mm.

For the flow visualization of the subsonic and supersonic flow, a digital single-lens reflex (DSLR) camera (Canon, EOS 600D) was used

with a zoom lens (Canon Zoom Lens EF 24-70mm 1:2.8 L USM). A DSLR camera has a low frame rate of 0.5 Hz and the shortest shutter speed is 250 μs, but the maximum resolution is 5184 x 3456 pixels. Thus, with the DSLR camera, the time resolution is low, but the spatial resolution is high. For the flow visualization of the hypersonic flow, a high-speed camera (Phantom, v710) was used with a zoom lens (Nikon 70-180mm f4.5-5.6 D). The maximum frame rate that can be achieved is 680 kHz, and the shortest shutter speed is 1 μs, whereas the maximum resolution is 1280 x 780 pixels. Thus, with the high-speed camera, the time resolution is high, but the spatial resolution is low.

Background-oriented schlieren technique

The BOS system can be established with a light source, a background pattern, a lens, and a camera, as illustrated in Fig. 2.14. Compared to Fig. 2.13(a), the configuration of the BOS system is simpler. A conventional light source can be used to illuminate the background enough to take the image with a camera. The background pattern is made with randomly positioned dots, or a natural environment behind the flow can be used without installing an artificial background. A convex lens is located to focus the camera onto the background, which makes the density gradient obtained from BOS images blurred.

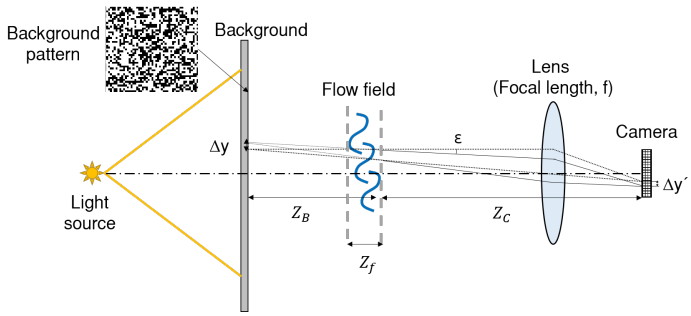

Figure 2.14: Configuration of the background-oriented schlieren technique.

To avoid this problem, the background pattern could be placed as near as possible to the testing region, but it can reduce the sensitivity because the displacement of the background pattern can become too small. When the BOS system is aligned, the camera takes background images at a reference state without the flow and in the condition that the wanted flow exists. Then, the displacement of the background pattern between these two images can be obtained using a cross-correlation method, which is generally used for the particle image velocimetry technique [76]. After the cross-correlation process, the displacement vectors, $\Delta x'$ and $\Delta y'$, are obtained, which can be converted to density gradient by applying the optics theory. During this procedure, density gradient can be acquired for both x and y direction simultaneously, whereas the conventional schlieren can acquire the density gradient in only one direction for each experiment. The density gradient can be numerically integrated to acquire density. From these density results, the wavefront passing through the

flow field can be calculated. Thus, the flow and optical information can be achieved at once, making it easier to analyze the optical aberration due to the flow field.

The feasibility of the BOS technique for an aero-optical study was validated in the subsonic heated flow experiment. In the BOS system of the subsonic heated experiment, a light source (Sumita, LS-M350), a background, a focal lens (Canon Zoom Lens EF 24-70mm 1:2.8 L USM), and a camera (Canon, EOS 600D) were used for subsonic and supersonic flow, whereas a high-speed camera (Phantom, v711) was used for the hypersonic flow. A light source illuminated the background from the backside. The distances to the background and the focal lens were 361 mm and 581 mm from the center plane of the hot gas flow, respectively. The focal length of the lens was set to 70 mm, and the F-stop was set to 5.6. The camera exposure time was set to 250 μs, which is the lowest. The camera was triggered by a 5 V signal generated using a 0.5 Hz rate, which was generated using a delay generator (DG-535).

2.3.2 Wavefront measurement system

The wavefront measurement system used for each experiment was composed, as depicted in Fig. 2.15. The components of the wavefront measurement system included a laser source, optical fiber, beam ex-

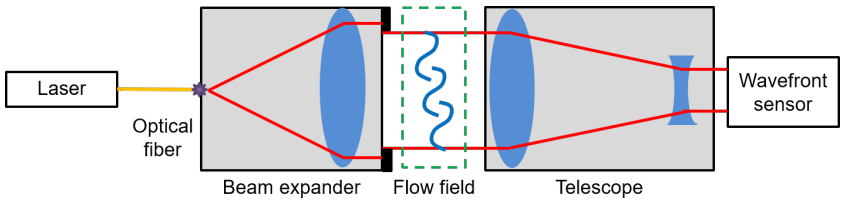

(a)

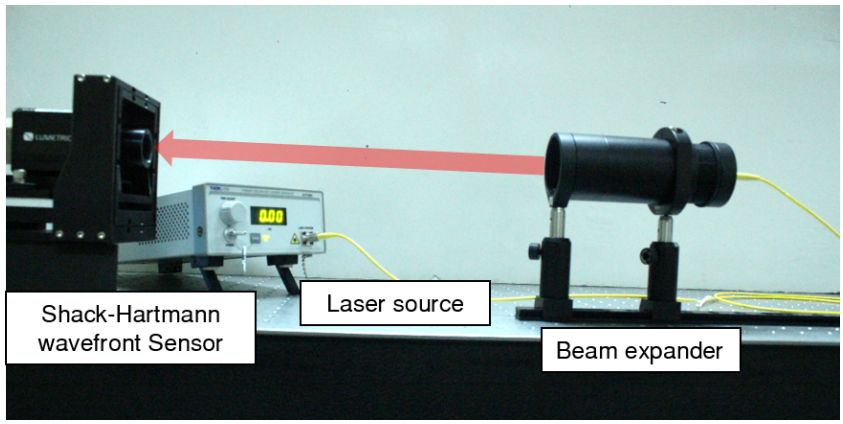

(b)

Figure 2.15: Optical composition of the wavefront measurement system.

pander, telescope, and SHWS. The laser source was transferred to the beam expander using an optical fiber, and then the laser beam was generated from the beam expander. The expanded beam propagated through the test region, and then the size of the aberrated laser beam was reduced with the telescope. Finally, the reduced aberrated beam entered the SHWS, and the data from the sensor were recorded.

The laser source used for the experiments is a diode laser (Thor-

labs, S1FC635) with a wavelength of 635 nm. The maximum output power of this laser source is 2.5 mW. This laser source was transferred to the beam expander with an optical fiber (Thorlabs, P1-630A-FC-2). The beam expander expanded the point source to a beam using an achromatic lens with a diameter of 50.8 mm and a focal length of 100 mm (Thorlabs, AC-508-100-A). The expanded laser beam was cropped at the end of the laser beam using a 25 mm aperture for subsonic and hypersonic flow and a 10 mm aperture for supersonic flow. Because the diameter of the beam was larger than the aperture of the SHWS, the beam with a diameter of 25 mm was reduced using a telescope composed of two achromatic lenses, which have positive and negative focal lengths. The lens with a positive focal length has a diameter of a 50.8 mm and a focal length of 180 mm (Thorlabs, AC-508-180-A), whereas the lens with a negative focal length has a diameter of 25.4 mm and a focal length -40 mm (Thorlabs, ACN-254-40-A). The laser beam with a diameter of 10 mm was not reduced. Thus, the telescope was not used for this case. In the subsonic and supersonic experiment, a reflection mirror was installed after the test region to steer the laser beam into the telescope or the Shack-Hartmann wavefront sensor.

The SHWS comprises a lenslet array and CCD, as illustrated in Fig. 2.16. As the optical wave enters the SHWS, the lenslet array focuses each region of the wavefront to points on the CCD, which is

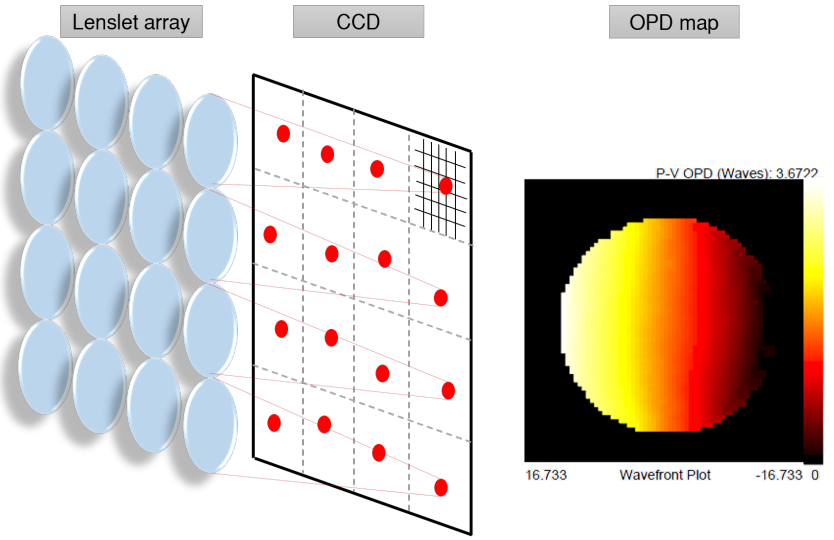

Figure 2.16: Composition and principle of the Shack-Hartmann wavefront sensor.

displaced from the lenslet array as the focal length of the lens of the lenslet array. From the geometrical calculation, the location of each focal point is related to the averaged slope of each region of the wavefront. Thus, the SHWS provides an image of dots, and postprocessing software calculates the slope of the wavefront, coincident to each dot. From these slopes of the wavefront, methods, such as the zonal, modal, or hybrid method, are adopted to reconstruct the wavefront.

For the experiment, a 2D SHWS (Lumetrics, XP-CLAS 2D) was used, which has a lenslet array consisting of 69x69 convex lenses with a focal length of 4.607 mm and a diameter 0.108 μm. The hybrid method, which uses both the zonal and modal methods, was used for

wavefront reconstruction in this dissertation. Furthermore, by recording the reference wavefront before the test, where the distorted wavefront due to the optical system was measured, only the aberration of the wavefront due to the flow field was provided through the SHWS. The aberration of the wavefront is provided through an OPD map.

Chapter 3

Numerical Methods

In this chapter, the numerical methods used in the dissertation are introduced. In the first part of the chapter, an overview of the method of the numerical simulation conducted to obtain the wavefront of the optical wave propagating through the flow field is introduced. In the second part of the chapter, the details on the methods to obtain the density of the flow field are described. The BOS-based and flow-simulation methods are described. In the final part of the chapter, the optical calculation methods are introduced. Two calculation methods, which are the straight-line assumed method and ray-tracing method, are also discussed. In this chapter, the numerical methods to acquire the density and estimate the propagation of the wavefront have been published in the *International Journal of Aeronautical and Space Sci-*

ences [77] and the numerical methods to calculate the optical wave have been presented at the KSAS 2019 fall conference [78].

3.1 Overview of the Numerical Simulation

To obtain more information than that derived from the experimental result and to complement the experiment, numerical simulations were conducted and the propagation of the optical wave along the flow field was obtained. The procedure for the overall numerical simulation is illustrated in Fig. 3.1. First, the density of the flow field must be obtained to compute the propagation of the rays through the flow field.

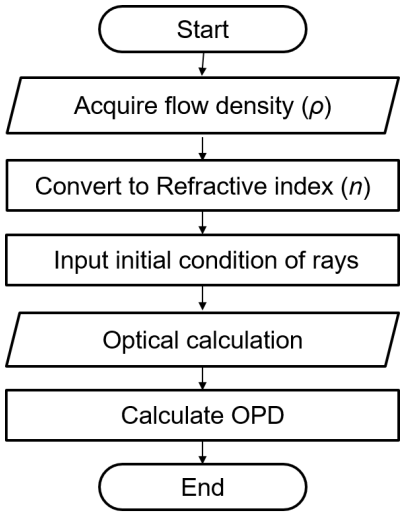

Figure 3.1: Procedure for the numerical simulation to obtain the wavefront of the optical wave propagating through a flow field.

Two methods were used to obtain the density of the flow field

numerically in this dissertation. The first method is based on BOS techniques, which reconstruct the density from the density gradient achieved experimentally. The second method is by solving the Navier-Stokes equations through the domain. For the subsonic flow, the density of the flow field is calculated from the BOS technique, and for the supersonic and hypersonic flow, the Navier-Stokes equations are solved. After the density of the flow field was obtained, then the density was converted to a refractive index using Eq. 1.1. Then, the initial condition of the rays was set, and the propagation of the optical wave along the flow field was calculated. In this dissertation, two methods were adopted to calculate the propagation of the rays: the straight-line assumption method and ray-tracing method. Finally, the OPD was calculated from the propagated rays. The optical calculation methods to propagate the ray through the flow field were validated using Snell's law, and the errors between these two different methods were compared. The OPDs obtained from the numerical simulation were compared with the OPDs measured experimentally, and the comparison of the results is described in the Chapter 5 and 6.

3.2 Numerical Methods to Obtain the Flow Density

The procedures to acquire the density from the BOS images are illustrated in Fig. 3.2. First, reference image of the background pat-

tern was captured when there was no flow. Then, the image of the background pattern was captured when the flow field was established. These BOS images were cross-correlated to acquire the displacement of the background pattern, which is represented with the unit of a pixel. Then, the pixel data were converted to a density gradient from the geometrical optics theory. Furthermore, this density gradient can be numerically integrated to obtain the density of the flow field. The detailed procedure and equations are described below.

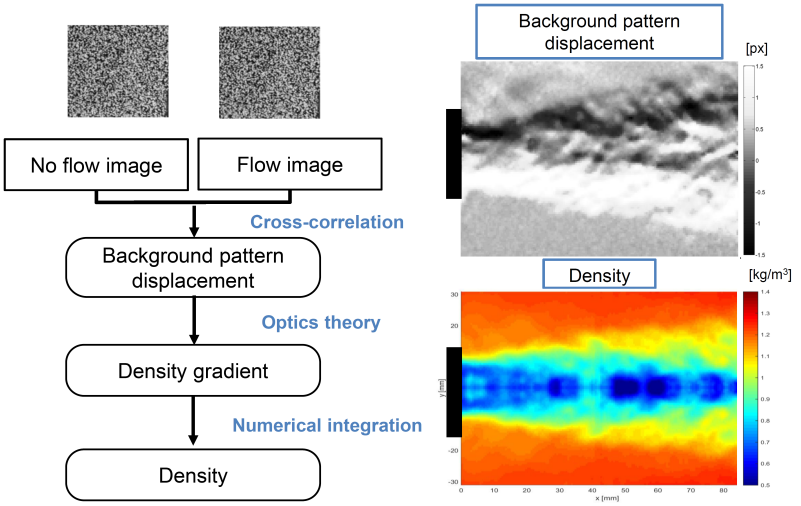

Figure 3.2: Procedure of the density acquisition method using background-oriented schlieren.

3.2.1 Density from the BOS technique

In the cross-correlation procedure, first, the pixels in the BOS images were divided into windows with the same pixel sizes. Then the win-

dows were cross-correlated, and one displacement vector was obtained per window. Therefore, the resolution of the dispacement vector was smaller than the original BOS images. In other words, using the same camera to capture the images for BOS technique and conventional schlieren, the BOS technique always have smaller resolution. The reduction of resolution could be compensated for by using other methods, such as the colored BOS [79], but it is beyond the scope of this study and was not considered. After the cross-correlation procedure, the vectors of the background pattern displacement were acquired. The relationship between the background pattern displacement and density gradient can be derived using optical theory based on geometrical optics [80–82]. When the deflection angles ε_x and ε_y are assumed to be small and the light rays are assumed to deflect at the mid-plane of the flow, the following equations are derived geometrically:

$$\varepsilon_x \approx \tan\varepsilon_x = \frac{z_b f}{z_c}\Delta x', \varepsilon_y \approx \tan\varepsilon_y = \frac{z_b f}{z_c}\Delta y', \tag{3.1}$$

where $\Delta x'$ and $\Delta y'$ are displacements of the background pattern, z_b is the distance from the mid-plane of the flow to the background pattern, z_c is the distance from the mid-plane of the flow to the camera, and f is the focal length of the lens. This deflection angle is related to the refractive index of light as shown in the following equations:

$$\frac{\partial\varepsilon_x}{\partial z} = \frac{1}{n}\frac{\partial n}{\partial x}, \frac{\partial\varepsilon_y}{\partial z} = \frac{1}{n}\frac{\partial n}{\partial y}, \tag{3.2}$$

$$\varepsilon_x = \int_{-Z_f/2}^{Z_f/2} \frac{1}{n}\frac{\partial n}{\partial x}\partial z, \varepsilon_y = \int_{-Z_f/2}^{Z_f/2} \frac{1}{n}\frac{\partial n}{\partial y}\partial z, \tag{3.3}$$

where z_f is the width of the flow or the width of the test section. If the flow is assumed to be 2D, the refractive index along the z-axis is coincidence and the perturbation of the refractive index of the flow can be neglected. Using Eqs. 3.1 and 3.2, the following equations can be derived:

$$\frac{z_b f}{z_c}\Delta x' = \varepsilon_x \frac{z_f}{n_0}\frac{\partial n}{\partial x}, \frac{z_b f}{z_c}\Delta y' = \varepsilon_y \frac{z_f}{n_0}\frac{\partial n}{\partial y}, \tag{3.4}$$

where n_0 is the refractive index of the reference state. Then, Eq. 3.4 can be differentiated, and the following Poisson equation is derived:

$$\frac{z_b f}{z_c z_f n_0}\left(\frac{\partial \Delta x'}{\partial x} + \frac{\partial \Delta y'}{\partial y}\right) = \frac{\partial^2 n}{\partial x^2} + \frac{\partial^2 n}{\partial y^2}, \tag{3.5}$$

where the left-hand terms are all known experimental values. The solution for the refractive index n can be numerically calculated from Eq. 3.5. Then, using Eq. 1.1, the density field can be acquired.

If the flow is axisymmetric, optical tomography processing must be applied [81, 82]. Neglecting the perturbation of the refractive index along the light ray, neglecting ε_x, and assuming the light ray is parallel

to the z-axis, Eq. 3.3 can be written as follows:

$$\varepsilon_y(y) = 2y \int_y^R \frac{\mathrm{d}n(r)}{\mathrm{d}y} \frac{\mathrm{d}r}{\sqrt{r^2 - y^2}}, \tag{3.6}$$

where $n(r)$ is the refractive index in the r coordinate. Defining the relative refractive index of difference $\delta(r)$ as the following equation, and applying the Abel inverse integral transform, Eq. 3.6 becomes the following:

$$\delta(r) = \frac{n(r)}{n_0} - 1, \tag{3.7}$$

$$\delta(r) = -\frac{1}{\pi} \int_y^R \varepsilon_y(y) \frac{\mathrm{d}r}{\sqrt{r^2 - y^2}}. \tag{3.8}$$

Using the adaptive Fourier-Hankel (AFH) method, Eq. 3.8 can be solved by calculating the following discretized equation:

$$\delta(r_i) = -\frac{\alpha}{N} \sum_{j=0}^{N} \frac{z_b f}{z_c} \Delta y'_j \sum_{k=0}^{N/\alpha} sin\left(\frac{\alpha \pi j k}{N}\right) J_0\left(\frac{\alpha \pi k i}{N}\right), \tag{3.9}$$

where N is a total number of samples of i, J_0 is a zero-order Bessel function of the first kind, and α is a coefficient between 0 and 1. The calculation time increases as α becomes smaller, but the accuracy of the result increases. From the acquired $\delta(r)$, the refractive index field $n(r)$ at the cross-section of the flow can be determined using Eq. 3.7. Finally, using Eq. 1.1, the density field at the flow cross-section is acquired. For the 3D complex flow, where the axisymmetric assumption cannot be used, several BOS images must be captured

from various directions, and the convolution theorem must be applied to reconstruct the flow. Thus, further efforts are required for hardware establishment and for image-processing procedures, which are beyond the scope of this dissertation.

3.2.2 Flow-simulation method

Flow simulations are also conducted to obtain the density of the supersonic and hypersonic flows. For the flow over the compression ramp inside the test section of the supersonic wind tunnel, the computational domain is depicted in Fig. 3.3.

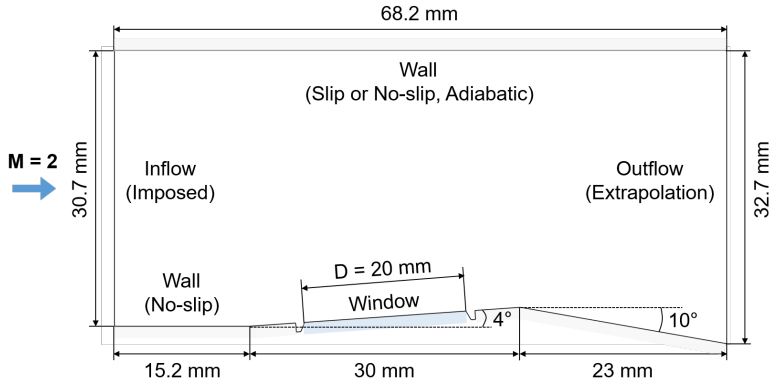

Figure 3.3: Computational domain used for the supersonic flow simulation.

The computational domain for the simulation of the flow field is 2D because the configuration of the compression ramp in the experiment is 2D. The small gap between the window and ramp was considered

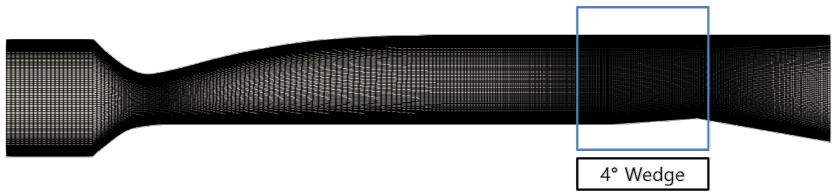

Figure 3.4: Computational domain used for calculation of nozzle exit flow condition.

in the simulation. The 2D compressible RANS equations were solved using a finite volume solver based on Roe's flux with a second-order total variation diminishing reconstruction. The implicit Gauss-Seidel method was used for time integration. The shear stress transport k-ω model was used for the turbulence. The total number of cells was 352,800, and the size of the first cell from the wall was designed to satisfy a y^+ of less than 1.2.

For the inflow boundary condition, the full domain of the test section, as depicted in Fig. 3.4, including the nozzle, was solved first. Then, the flow direction and velocity were adjusted to match the flow visualization result acquired from the wind tunnel experiment. From this adjustment, the shock wave generated between the nozzle and compression ramp can be demonstrated. The angle of the Mach wave before and after the shock wave was measured and the flow directions to match this Mach wave angle were calculated.

For the inflow boundary condition of the full domain of the test section, the stagnation pressure was set to 0.72 MPa, and the stag-

nation temperature was set to 300 K. For both the wall and glass, the adiabatic and no-slip boundary conditions were adopted. For the top plate of the test section, two simulations are conducted with the no-slip and slip conditions to exclude the aero-optical effects due to the boundary layer at the top wall. For the boundary condition at the outflow, the extrapolation boundary condition was adopted.

The flow simulations for the hypersonic wedge flow are conducted with a similar method used for the supersonic flow. The computational domain used for the hypersonic flow simulation is depicted in Fig. 3.5. The computational domain for the simulation of the flow field is 2D because the width of the wedge in the experiment is sufficiently large so that the flow region where the laser beam propagated through could be assumed to be 2D. The flow region between the top plate and the wedge was only considered to reduce the computational cost. The 2D compressible RANS equations are solved with coincident numerical scheme and turbulence model adopted for superosnic flow-simulation. The total number of cells was 132,000.

The size of the first cell from the wall was designed to satisfy a y^+ of less than 1.0, which was 0.1 in the simulation result. For the inflow boundary condition, a uniform Mach 7 flow was set, assuming that the model is within the uniform flow region of the nozzle. A simulation was conducted for two stagnation conditions: the low-density and high-density cases. For the low-density case, stagnation pressure was 1.69

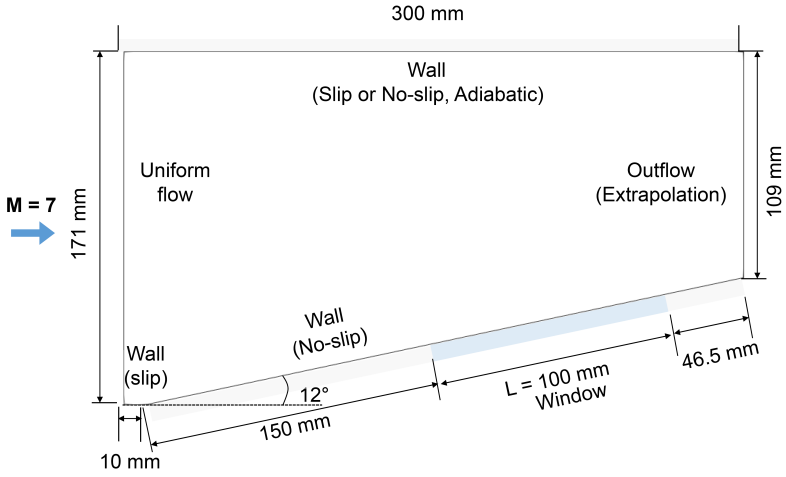

Figure 3.5: Computational domain used for the hypersonic flow simulation.

Mpa, and the stagnation temperature was 745.3 K. For the high-density case, the stagnation pressure was 3.2 Mpa, and the stagnation temperature was 631.2 K. For both the wall and glass of the model, the adiabatic and no-slip boundary conditions were adopted. For the up-plate, two simulations with no-slip and slip conditions were conducted to exclude the aero-optical effects due to the boundary layer at the up-plate. For the outflow, the extrapolation boundary condition was adopted.

3.3 Optical Calculation

Two methods were adopted in this dissertation to acquire the wave-front propagating through the flow field. The propagation path of the rays along the computation domain using these methods is illustrated

in Fig. 3.6. The first method assumes the rays propagate in a straight line, neglecting the deflection along the ray path. The procedure of this numerical method is depicted in Fig.3.7. This could be valid because the refractive index of the flow changes slightly, and the values are usually near 1.

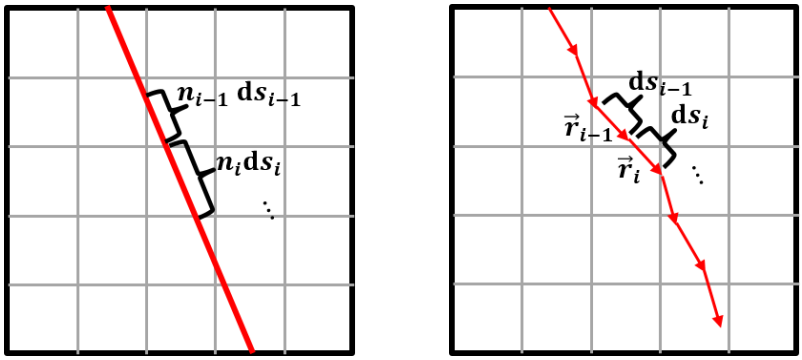

(a) (b)

Figure 3.6: Propagation of rays along the computation domain depending on the methods: (**a**) straight line ray and (**b**) ray-tracing.

In this method, the rays were assumed to be a straight line, and the OPL of each ray was calculated using Eq. 1.3. Then, the wavefront can be reconstructed by finding the same OPL location between the rays, or the OPD can be acquired using Eq. 1.4. The straight-line assumption might have some error due to neglecting the deflection, but the computation cost was very low. The straight-line assumption method was adopted for the subsonic heated flow case. The schematic of the OPD calculation in the heated subsonic flow is shown in Fig. 3.8. As in Fig. 3.8, the optical properties of the laser beam passing

through the hot jet flow were measured using the SHWS. Therefore, the SHWS measures the wavefront of the laser beam along xz-plane, whereas the BOS image is taken along the xy-plane. Thus, OPD obtained from the BOS images by applying Eqs. 1.3 and 1.4 corresponds to the x-axis, which corresponds to the centerline of the OPD map measured using the SHWS. A smaller value of the OPD means that a ray of the laser beam passed through the flow region with a smaller n value, which corresponds to a smaller density. In other words, a ray of the laser beam becomes shorter as the beam passed through the flow. Generally, the OPD is nondimensionalized using the laser beam wavelength, which is 635 nm. All measurement data are synchronized using a triggering signal generated from the delay generator.

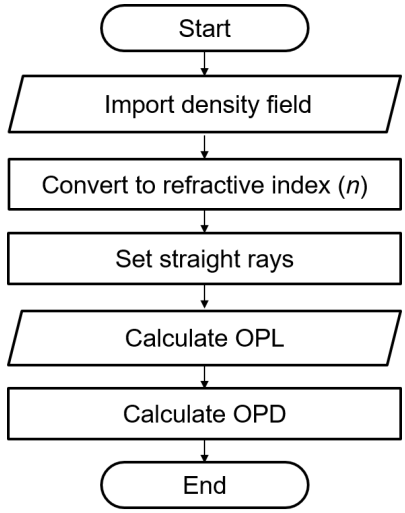

Figure 3.7: Procedure for the numerical calculation for the straight-line ray method.

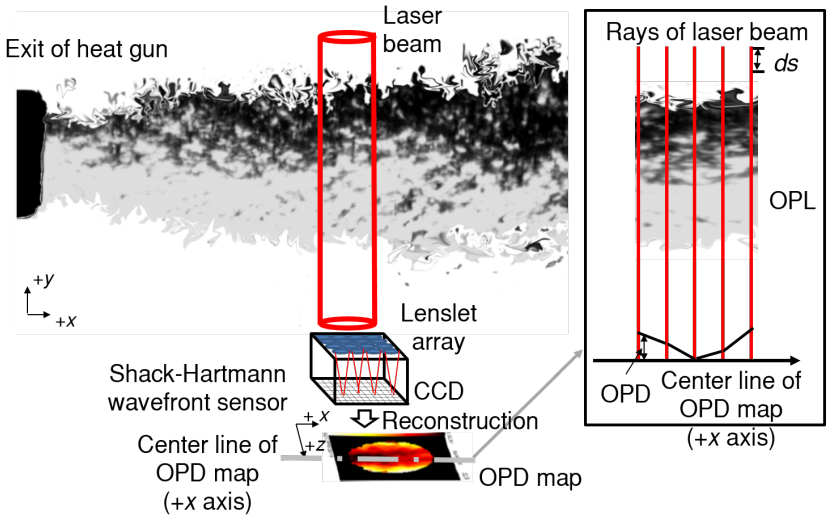

Figure 3.8: Schematic of optical path difference calculated in subsonic heated flow.

The second method for the optical calculation is solving the ray equation, Eq. 1.2 to acquire the path of the rays through the flow field. The procedure for the ray-tracing method is depicted in Fig. 3.9. The ray equation was solved using the Runge-Kutta method [83]. With the given index of refraction, step size of the ray, initial ray position, and incidence angle, the propagation of the ray through the flow field were computed. First, the density of the flow field should be determined throughout the region to be calculated. Then, the density of the flow field was converted using Eq. 1.1. After obtaining the index of refraction of the flow field, the index of reaction was differentiated numerically. Then, with the given initial ray position and incidence angle, the propagation of the ray was computed through the super-

sonic flow field with a given step size. Because the step size of the ray and the cell size for the flow field calculation differ, the value of the index of refraction at the ray position was interpolated from the given field of the index of refraction.

The step size of the ray varies within the flow field to reduce the computational time while resolving the boundary layer. The step size was set to 0.001 mm near the wall, to 0.02 mm within the boundary layer, and 0.05 mm outside the boundary layer. The initial ray position was set at the top plate of the test section, and the incidence angle was set as normal to the surface of the ramp. The propagation of each ray terminated at the surface of the ramp. Thus, the position and direction of each ray were acquired along the surface of the ramp. The refraction due to the window was neglected because the index of refraction between the surrounding atmosphere and the flow field is similar, which results in negligible deflection by the window. With the acquired ray directions and positions, the wavefront was reconstructed by calculating the OPD. The relationship between the OPD and slope of the wavefront was geometrically derived using the following equation:

$$\theta_w = \arctan(\frac{\triangle \text{OPD}}{n \triangle r_x}), \tag{3.10}$$

where θ_w is the slope of the wavefront and $\triangle$OPD is the difference in the OPD between the neighboring rays, and $\triangle r_x$ is the distance between the positions of those neighboring rays. Because the ray is

perpendicular to the wavefront, the slope of the wavefront equals the angle of the ray. Thus, OPD can be calculated from the ray position and direction using Eq. 3.10.

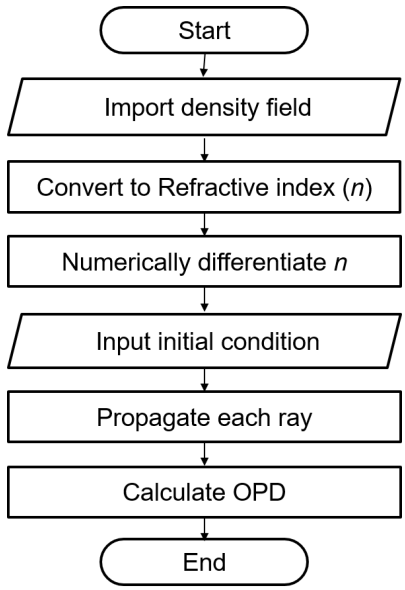

Figure 3.9: Procedure of the numerical calculation for the ray-tracing method.

However, with the above methods, the refraction of the rays due to the windows cannot be considered and only the refraction along the flow field was calculated. Thus, for some simulations, the windows at the test section and model were considered during the optical calculation. As depicted in Fig. 3.10, only the refraction due to the windows is considered, and this refraction angle is calculated using Snell's law:

$$n_1 \sin\theta_1 = n_2 \sin\theta_2, \tag{3.11}$$

where θ is the angle between the ray and the normal vector of the surface. For simplicity, the displacement of the position of the ray due to the window was neglected throughout the calculation. Then, applying Snell's law multiple times, the following relation is derived:

$$n_1 \sin\theta_1 = n_3 \sin\theta_3, \tag{3.12}$$

where the notation is depicted in Fig. 3.10. Thus, the refractive index of the window is not needed for the calculation. During the simulations considering the refraction due to the windows, the OPD was reconstructed using the reference ray without the flow. This is to simulate a procedure similar to that of the SHWS, which provides OPD maps reconstructed from the reference wavefront of the laser beam acquired before each run. For the supersonic flow, the direction of the reference rays is the same as the incident rays because the air inside the test section is the same as that in the surrounding atmosphere, which means n_1 and n_3 are the same in Eq. 3.12.

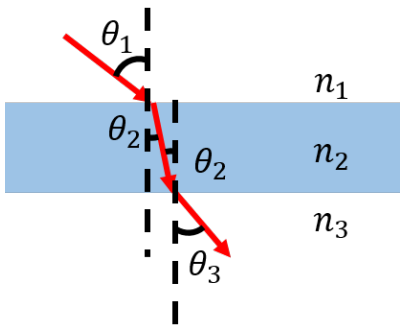

Figure 3.10: A ray propagating through a window.

However, for the hypersonic flow, the test sections are vacuumed for each run, and the reference wavefront of the laser beam is acquired in this vacuumed condition. Thus, n_1 and n_3 are different, and the direction of the reference rays is different from the incident rays. The effect of the refraction due to the windows is described in more detail in Chapter 6.

Before computing the propagation of the optical wave through the flow field, the optical calculation was validated using Snell's law. A simple computational domain with a structured grid was generated, as depicted in Fig. 3.11. The computational domain was divided into two regions with a surface inclined with a certain angle, and a uniform refractive index is assumed for each region. The grid size was 0.01 mm, n_1 was 1.0002, and n_2 was 1.03. Moreover, n_1 was set to a refractive index similar to the atmosphere, whereas n_2 was the refractive index of a high-density gas to intensify the angle of refraction to easily validate the optical calculation methods. The inclination angle of the line dividing the regions was also set to a high value to intensify the refraction angle, which was set to 45°. The initial rays were directed downward, parallel to the y-axis.

The deflection of the rays at the surface of the inclination is shown in Fig. 3.12(a) when the ray-tracing method is adopted. The deflection angle from the initial ray direction calculated using Snell's law was 1.6346°. The deflection angle calculated from the straight-line

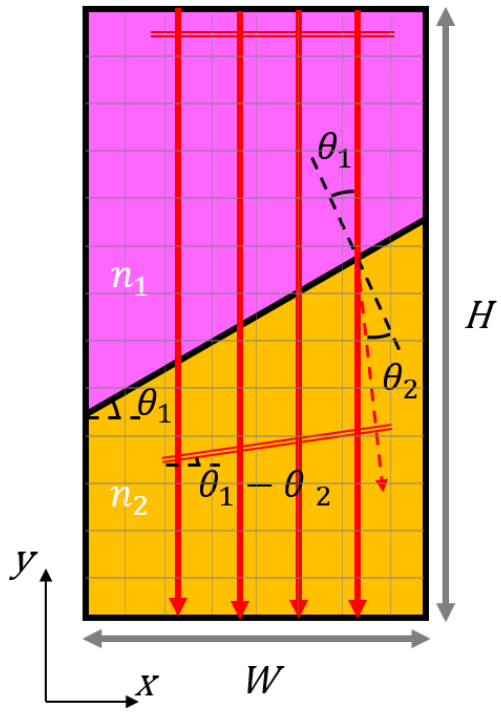

Figure 3.11: Computation domain for the validation of the optical calculation methods.

assumption was 1.6585°, which is a 1.46% error, whereas the deflection angle calculated from the ray-tracing computation was 1.6347°, which constitutes a 0.17% error. The reconstructed OPD results are presented in Fig. 3.12(b). The OPD values obtained from Snell's law and the optical calculations are similar. Thus, the optical calculation methods can be used to calculate the propagation of rays through a flow field.

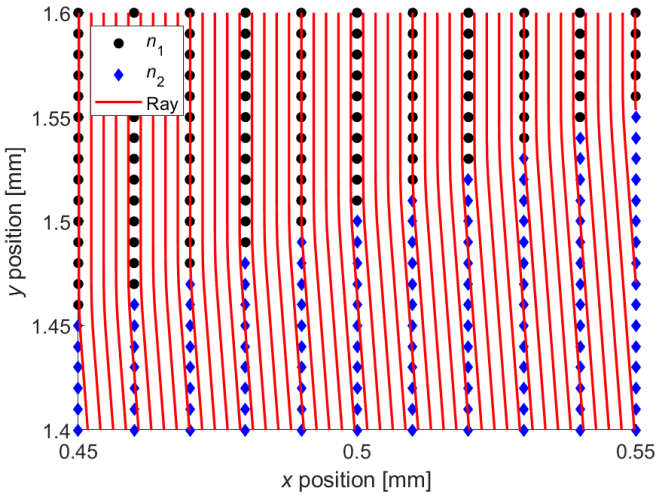

(a)

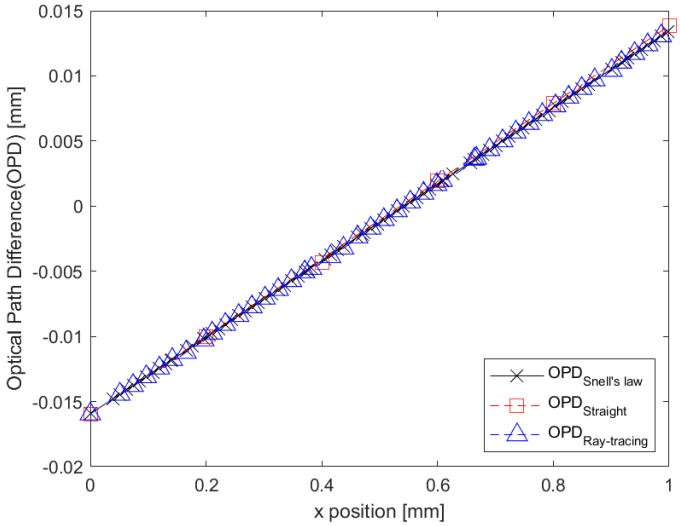

(b)

Figure 3.12: Validation of the ray-tracing computation: (**a**) ray-tracing computation result for rays propagating through two regions with different indices of refraction and (**b**) comparison between the optical path difference calculated using Snell's law and the optical path difference acquired from the ray-tracing computation.

Chapter 4

Aero-optics in Subsonic Heated Flow

In this chapter, a preliminary experiment conducted with the subsonic heated jet is described. In the first section of the chapter, the BOS technique is qualitatively evaluated. The BOS images and conventional schlieren flow visualization results are compared. In addition, the density calculated from the BOS result for numerical calculation is presented. In the second part of the chapter, the wavefront measurement result using the SHWS is discussed. Then, in the final part of the chapter, the wavefront measurement result and the calculated result are compared and validated. In this chapter, some parts are included that have been published in the *International Journal of Aeronautical*

and Space Sciences [77].

4.1 Flow Field of the Heated Subsonic Jet

The flow field of the subsonic heated jet was visualized using BOS and conventional techniques. For BOS techniques, the first important step is to acquire high-quality background images. The BOS images taken for the subsonic heated jet is shown in Fig. 4.1. Figure 4.1(a) is a reference image taken before the activation of the hot gas gun, and Fig. 4.1(b) is a flow image captured when the hot gas gun is activated. Because the resolution decreases during the cross-correlation process, as described in Chapter 2, a high-resolution DSLR camera was used to capture these BOS images.

Further, as the camera lens is focused on the background pattern rather than the flow field itself, the shadow of the heat gun was blurred, as shown in Figs. 4.1(a) and 4.1(b). Thus, the displacement of the background pattern at this edge of the shadows has considerable errors. This blurriness could be reduced by installing a background pattern closer to the heated jet, but then the magnitude of the density gradient reduces, making the visualization of the flow difficult. Thus, selecting an appropriate location of the background pattern is essential for BOS techniques.

Because the laser beam used for the measurement of the wavefront is far from the edge of the shadows, the position of the background

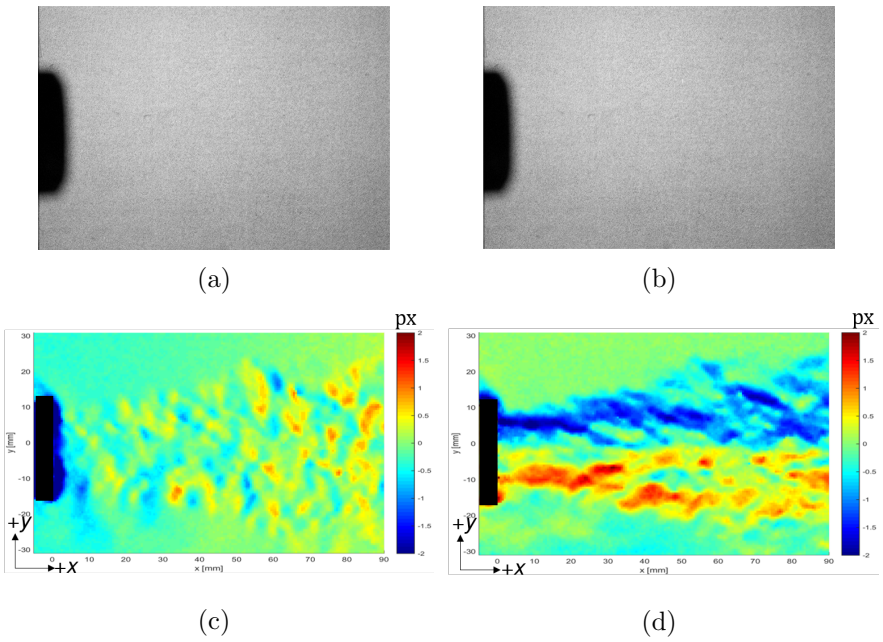

Figure 4.1: Raw background-oriented schlieren (BOS) image and displacement of background pattern: (**a**) reference BOS image (Heat gun off), (**b**) flow BOS image (Heat gun on), (**c**) x-direction displacement, and (**d**) y-direction displacement.

pattern is selected to sufficiently intensify the density gradient. From the captured BOS images, the displacement of the background pattern is achieved from cross-correlation, as shown in Figs. 4.1(c) and 4.1(d), which are the displacements along the x- and y-directions, respectively. The flow features of the hot jet are more dynamic in the y-direction than in the x-direction, when comparing Figs. 4.1(c) and 4.1(d). In Fig. 4.1(c), the shape of the hot jet is difficult to identify, whereas Fig. 4.1(d) presents the jet more clearly. Moreover, the magnitude of the displacement vector is larger for the y-direction. Thus, the

density gradient along the y-direction is larger than the x-direction, which may be due to the rapid expansion along the y-direction rather than the x-direction. Here, another advantage of the BOS compared to the conventional schlieren method is proved. When the density gradient direction is not known, it is difficult to choose the direction of the knife-edge for the conventional schlieren method. Thus, several experiments must be conducted with different directions of the knife-edge; otherwise, the flow features may not be clearly observed. However, the BOS technique could obtain the density gradient in the x- and y-directions simultaneously, and one test could be enough to analyze the flow field. For further analysis, the displacement of the background pattern was converted to the density gradient using Eq. 3.4.

The converted density gradient from the displacement of the background pattern was compared with the conventional schlieren image, as shown in Fig. 4.2. Because flow features are more visualized along the y-direction, a comparison is performed for the y-direction. Figures 4.2(a) and 4.2(c) present the y-directional density gradient calculated from the background pattern displacement. Figures 4.2(b) and 4.2(d) depict conventional schlieren images taken with the same exposure time as the BOS system. The knife-edge is set to a horizontal direction to acquire the y-component of the density gradient. Comparing Figs. 4.2(a) and 4.2(b), the flow appears similar, but the detailed

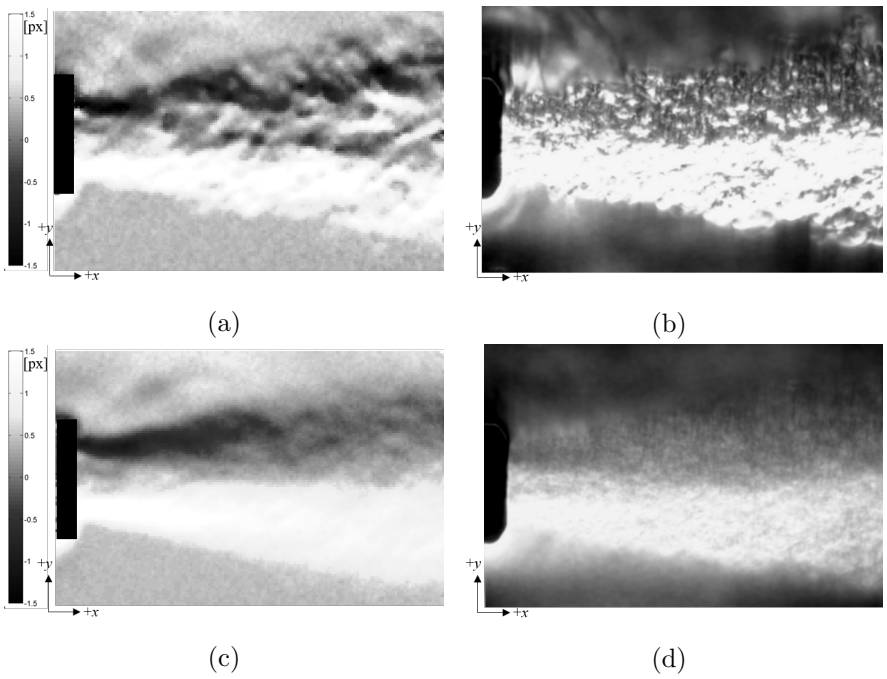

Figure 4.2: Displacement of the background pattern and schlieren image: (**a**) instantaneous displacement, (**b**) instantaneous schlieren image, (**c**) time-averaged displacement, and (**d**) time-averaged schlieren image.

flow structure inside the hot jet is different. It is understood that the flow was originally unsteady, and the schlieren and BOS images were not measured at the same time. The density gradient obtained from BOS images reveals a lower spatial resolution than the conventional schlieren image due to the cross-correlation process, which reduces the resolution by a factor of 64 in this experiment. When time-averaged, both the density gradient and conventional schlieren images show a smoothed flow structure inside the jet, where the unsteadiness of the

flow can be neglected. Comparing the density gradient obtained from the BOS images and the conventional schlieren image, the ratio of the jet length (x-direction) to the jet height (y-direction) is similar. Thus, images and the density gradient obtained using the BOS technique are reliable.

4.2 Density Acquisition from Background-oriented Schlieren Images

At first, the density was obtained from the BOS images by numerically solving the Poisson equation, as shown in Eq. 3.5. The Poisson equation is solved using numerical integration. The boundary condition at the top and bottom was set to 1 atm and 300 K, while the left and right sides were set to the extrapolation conditions. The obtained density is shown in Fig. 4.3. Near the exit of the nozzle, the density is high, and the density decreased as the jet flowed. Additionally, the density of the jet is smaller than that of the atmosphere. This follows the physics because pressure does not change much within the jet, whereas the temperature is higher than that of the atmosphere, resulting in a smaller density than the atmosphere. Furthermore, the shape of the jet near the nozzle exit is too small compared to the nozzle exit. Moreover, the expansion is rapid compared to the schlieren results. Considering that the jet has axisymmetric flow, the light near the axis passes through more of the flow region than the outside part.

Thus, displacement of the background pattern along the axis of the jet is intensified compared to the outer part of the jet. Thus, special treatment is necessary when analyzing the axisymmetric flow, and the 2D assumptions do not seem appropriate for the current flow field. Therefore, the axisymmetric assumption was adopted, and the density was obtained using the AFH Abel inversion.

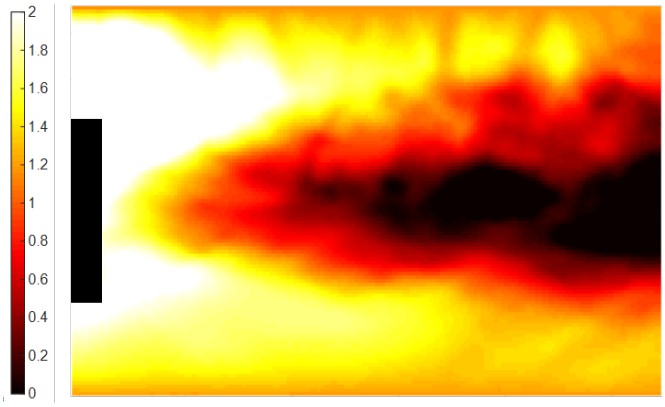

Figure 4.3: Density field obtained from background-oriented Schlieren images by integrating the Poisson equation.

Applying the AFH Abel inversion method to the density gradient field, the radial density field at the cross-section of the center of the hot jet was obtained, as shown in 4.4. The boundary conditions at the top side were set to 1 atm and 300 K, which were the atmospheric conditions. The coefficient α was set to 1.0 when adopting Eq. 3.9, which is the lowest accuracy and fastest computation time. The figure reveals the selected density field captured every 2 s when the hot jet is fully developed. Due to the shadow of the nozzle and the blurriness

near the nozzle, which was generated due to the limitation of the BOS technique, the density around the nozzle exit has substantial errors. The hot jet emitting from the nozzle exit seems to exhibit conventional subsonic flow features. As the hot jet propagates toward the $+x$-direction, the jet height increases. The shear layer of the hot jet is stable near the nozzle exit and becomes unstable from $x = 45$ mm. After $x = 45$ mm, the shear layer is unstable and complicated, as observed in the figure. The general structure of the hot jet is unsteady, whereas the hot jet height is almost similar, independent of time. The overall density of the hot jet is lower than the ambient air because the temperature of the gas is higher.

At the center of the jet flow, high-density fluctuation exists because the difference in the temperature is high. The size of the small density core region near the center of the jet (blue region in Fig. 4.4) varies depending on time. This may be due to the commercial hot gas gun, which cannot emit the high-temperature gas uniformly. The lowest density is formed near the center axis of the hot jet ($y = 0$ mm) and near the outlet of the heat gun ($x = 0$ mm). The minimum density value was around 0.6 kg/m^3. This value is similar to 0.67 kg/m^3, which is the density of the air for the conditions of pressure at 1 atm and a temperature of 523 K. As this low-density core expands and mixes with the ambient air, the density increases and recovers to that of the ambient air. Thus, comparing the density near the core region

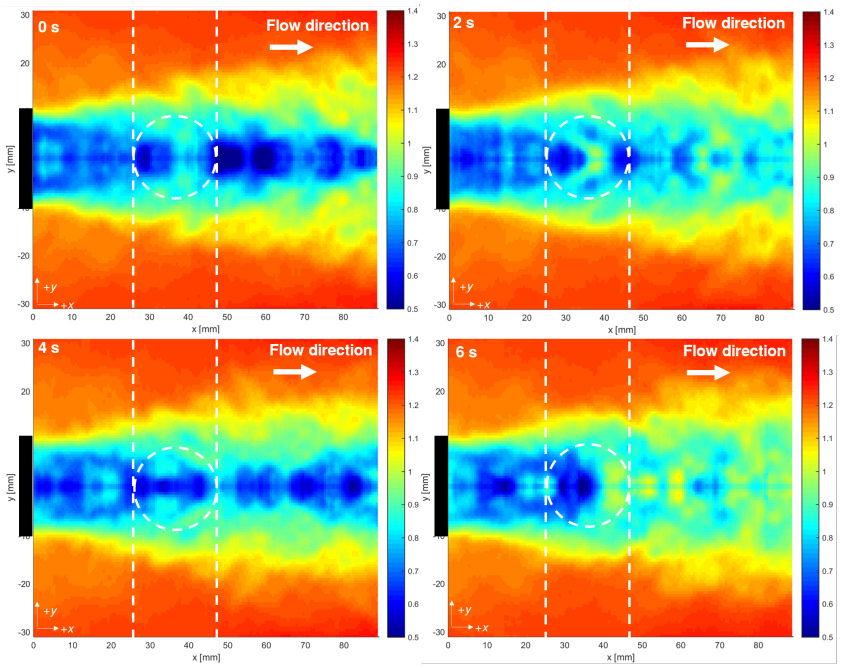

Figure 4.4: Density field obtained from the background-oriented schlieren images applying adaptive Fourier-Hankel Abel inversion.

and the density calculated from the simple theoretical analysis, the density field obtained from BOS images seems reasonable.

Figure 4.5 is an OPD map of the laser beam obtained by the SHWS, which is obtained at a coincident time, as in 4.4. In Fig.4.5, the OPD is measured within a certain range of -1 to 2λ, which was -6.35×10^{-7} to 12.7×10^{-7} m. In another study that also investigated the aero-optical characteristics for a hot jet, the OPD was measured within the range of -4×10^{-7} to 4×10^{-7} m [63]. The OPD obtained in Fig.4.5 has a similar order but a wider range than another study.

This seems to due to the difference in the jet temperature, which is around 350 K in another study, much lower than the temperature of the hot jet flow produced in this paper.

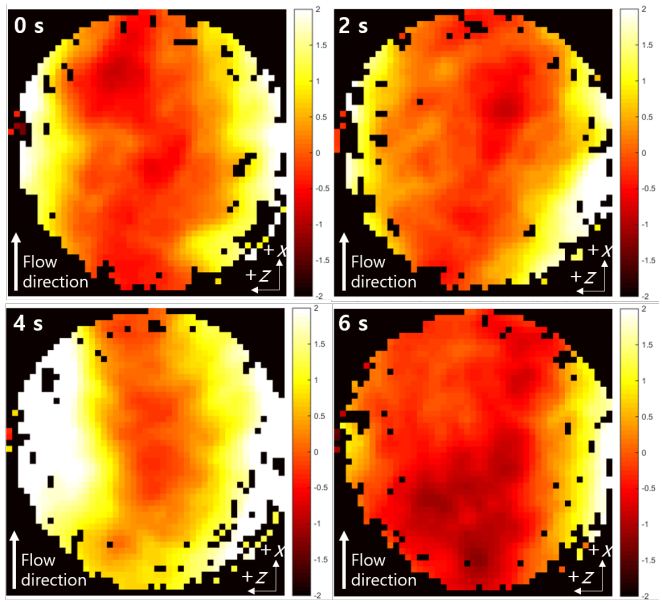

Figure 4.5: The optical path difference map acquired using the Shack-Hartmann wavefront sensor.

The lower temperature jet has a lower density difference between the jet and atmosphere. Therefore, the aberration is smaller, resulting in a narrower OPD range. Thus, the OPD measured with the SHWS, as depicted in Fig. 4.5 can be reasonable.

Dotted white lines are indicated in Fig. 4.4o compare the measured OPD map and calculated density field. The lines mean the location of the laser beam path propagating through the hot jet. The dotted

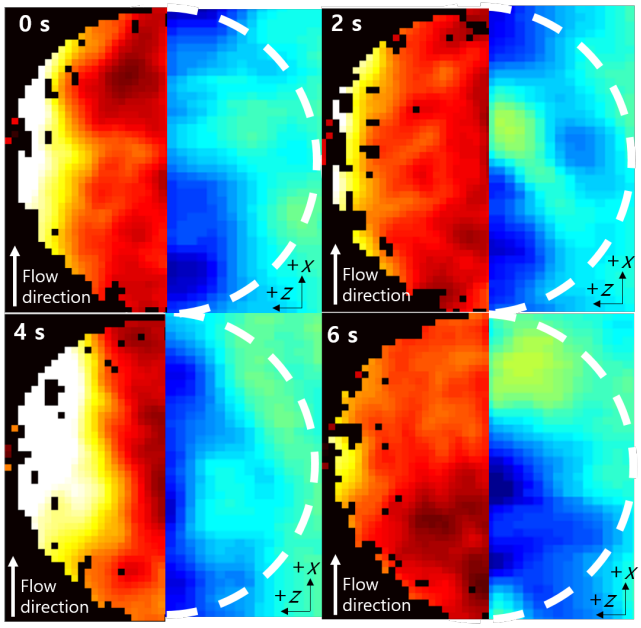

Figure 4.6: Comparison of the optical path difference (OPD) map and density field: (Left) OPD map acquired using the Shack-Hartmann sensor and (Right) density field obtained from the BOS images.

white circle in Fig.4.4 indicates the corresponding position of the laser beam. That is, this dotted white circle represents the same location of the SHWS measurement area. Thus, the OPD and density field can be compared, as illustrated in Fig. 4.6. In Fig. 4.6, the flow direction is from the bottom toward the top, which is in the $+x$-direction. Along the z-direction, the OPD value is lower at the center of the hot jet. Thus, the refractive index of light is lower inside the hot jet than the ambient atmosphere.

Because the density is linear to the refractive index, the OPD map

also indicates that the density value is lower inside the jet. The unsteadiness of the density field is also shown in the OPD map. Along the x-axis, the circled region of the different OPDs is distributed randomly. This seems to be a turbulence eddy formed inside the hot jet, which is also observed inside the hot jet in Fig. 4.4. The blue core region at the density field seems to be depicted as a dark region in the OPD map. In addition, the green region inside the density field at 6 s corresponds to the yellow region inside the OPD map. The detailed flow structure inside the OPD map and density field seems to be different because the OPD map exhibits total integration of the density along the beam path, whereas the density field exhibits the cross-section of the hot jet, but these two results seem qualitatively similar.

4.3 Quantitative Evaluation of Background-oriented Schlieren for Aero-optics

The OPD calculated from the density field was compared with the measured data using the SHWS to evaluate the density field obtained by the BOS images. Figure 4.7 illustrates the OPDs calculated using each density field. The red line represents the OPD results calculated using the BOS images and the dashed black line represents the data extracted along the center line of the OPD map acquired using the SHWS. The results displayed in Fig. 4.7 are the OPD values in the

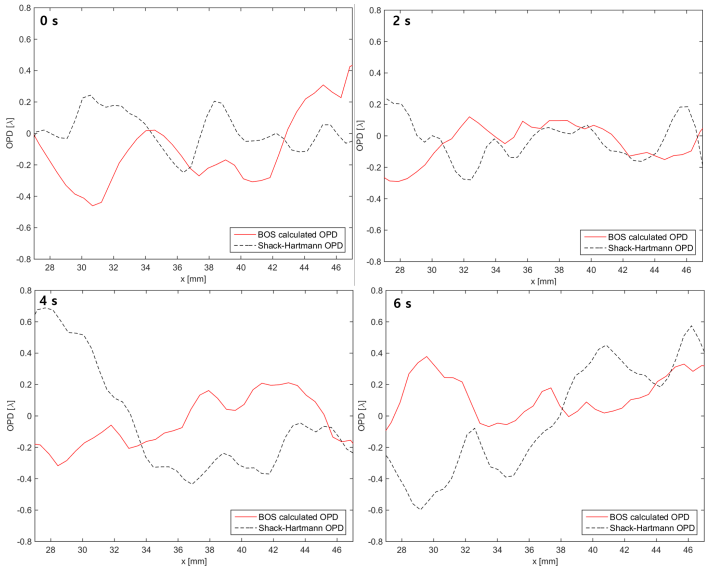

Figure 4.7: The optical path difference along the center of the jet (x-axis).

region between 27 mm and 47 mm, apart from the nozzle exit, which corresponds to the area through which the laser beam passes. The negative value of the OPD is from the subtraction of the average OPL, as indicated in Eq. 1.4. The results reveal that both data are comparable for all measured times and are within a similar range. Moreover, the tendency that the OPD varies along the x-direction seems similar for all cases. Generally, the difference between both data sets was larger in the region near the nozzle exit. In this region, OPD data calculated from the BOS image are lower than the measured OPD, except the 6 s result. This is due to the difference in the density field calculated from the BOS images and the actual density field. As displayed in Fig.

4.2(b), from the conventional schlieren image, the actual flow seems to be the turbulence flow containing a complicated vortex and eddy. This complex flow cannot be specifically resolved using one BOS image, assuming the flow is axisymmetric. Thus, the OPD at the hot core region near the exit of the heat gun cannot be properly calculated and exhibits a larger difference than other regions. To enhance the accuracy of the OPD calculation, the axisymmetric assumption could be neglected, and several BOS images from various directions could be captured simultaneously to reconstruct the 3D density field, as in the study by Hartmann and Seume [84], but this is outside of the scope of this study. The effect of the turbulence on OPD estimation can be obvious by removing the unsteadiness of the flow using time averaging and removing the local turbulence characteristics.

The validity of the 2D assumption for the subsonic heated jet is further analyzed by comparing the OPD. The OPD was calculated based on the 2D and axisymmetric assumptions, and the OPD was measured and compared using the SHWS, as illustrated in Fig. 4.8. The calculated OPD with the axisymmetric assumption and the measured OPD are quite similar, whereas the 2D assumption is different except for the trend. The larger OPD seems to be due to the rapid expansion of the jet in the 2D assumption and the lower density within the jet. As mentioned, this seems to be due to an intensified density gradient near the axis of the jet. Thus, once again, the 2D assumption

cannot be used for the current flow configuration.

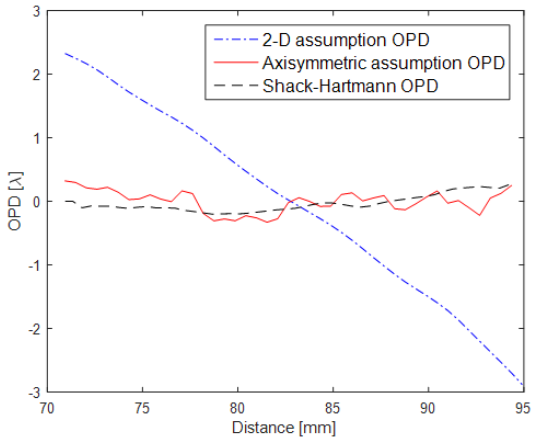

Figure 4.8: Comparison of the two-dimensional and axisymmetric assumption for the optical path difference (OPD) along the center of the jet (x-axis).

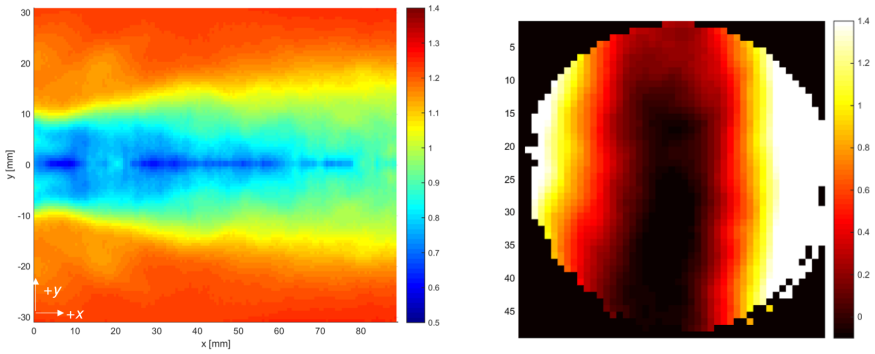

(a) (b)

Figure 4.9: Time-averaged results: (**a**) density field, and (**b**) optical path difference (OPD) map) OPD along the x-axis.

Figure 4.9 illustrates the time-averaged results for both cases. In addition, Fig. 4.9(a) reveals the time-averaged density field obtained

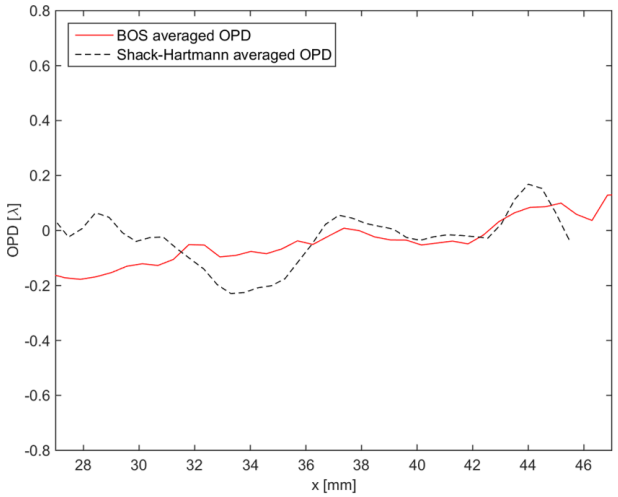

Figure 4.10: Comparison of the time-averaged optical path difference along the x-axis.

by the BOS images. Moreover, Fig. 4.9(b) lists the time-averaged OPD result obtained from the SHWS. The results were obtained by averaging 20 instantaneous images. Figure 4.10 depicts the comparison results for both data. The red line is the OPD results calculated from the time-averaged density field, and the dashed black line represents the results obtained along the x-direction at $z = 0$ in Fig. 4.9(b). Compared with the results in Fig. 4.5, the variation of the density in the heated core region of the jet flow is lower and the flow structure becomes more uniform in the time-averaged results. In other words, many turbulent flow properties become smeared by time averaging. Therefore, for the time-averaged data, the density near the nozzle exit of the heat gun is minimum, and it recovers to the ambient properties as it propagates toward the $+x$-direction.

Similarly, the difference between the OPD value calculated through the BOS images and the OPD value measured using the SHWS is smaller when the turbulence characteristic is removed using time averaging, as displayed in Fig. 4.10. To analyze the error of the OPD calculated from the BOS images, OPD_{rms} was calculated for both OPD values. The OPD_{rms} for the BOS was 0.0921λ, whereas, for SHWS, the OPD_{rms} was 0.1011λ. The relative percentage error of this OPD_{rms} was 8.9%, which seems reasonable for the aero-optics characteristic investigation. Thus, the density field acquisition using the BOS images is expected for a qualitative investigation of similar research without a high cost.

Chapter 5

Aero-optics in Supersonic Flow

IIn this chapter, the aero-optical phenomena due to the shock wave and boundary layer in the supersonic flow are described. In the first section of the chapter, the flow field over the compression ramp is discussed. The flow visualization results are presented, and the numerical flow-simulation results are validated. In the second part of the chapter, the wavefront measurement results are described. In the final part of the chapter, the optical calculation that was conducted using the ray-tracing method is presented. The numerical results are compared with the measurement results, and individual contributions of the shock wave and boundary layer on the aero-optical phenom-

ena are discussed. In this chapter, some included parts have been presented at the KSAS 2019 fall conference [78].

5.1 Supersonic Flow Field Over the Compression Ramp

The supersonic flow field over the compression ramp is illustrated in Fig. 5.1. Figure 5.1(a) presents the shadowgraph image captured during the wind tunnel experiment, and Fig. 5.1(b) depicts the synthetic shadowgraph image obtained from the numerical simulation. Multiple shock waves are depicted in Fig. 5.1(b), including the oblique shock wave generated by the ramp. The shock wave at the top of the test section was generated by the window installed on the top plate of the test section, where a small gap was found between the window and top plate. Because the Mach wave and the other shock waves do not change substantially at the intersection point, this shock wave does not affect the flow field considerably; thus, this shock wave is not considered for further analysis.

In contrast, the shock wave at the inflow boundary changes the angle of the Mach wave at the intersection. Moreover, because this shock wave reflects at the bottom plate of the test section, the reflected shock wave merges with the oblique shock wave generated by the ramp. Accordingly, the shock wave at the inflow was considered for the numerical simulation. As described in Section 3.2.2, the inflow

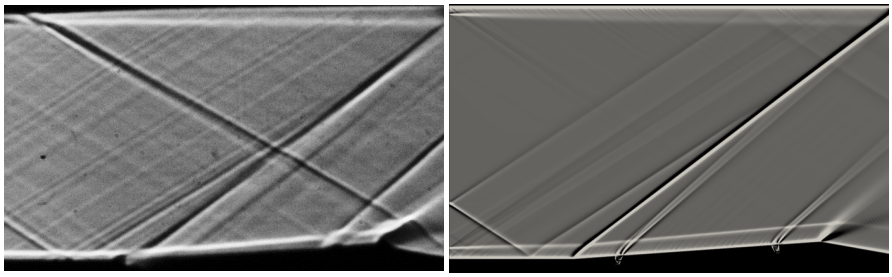

(a) (b)

Figure 5.1: Comparison of shadowgraph images: (**a**) image captured during the experiment and (**b**) image acquired from the numerical simulation.

boundary conditions were imposed to demonstrate this shock wave. The angle of the Mach wave before and after the shock wave was measured using the shadowgraph image in 5.1(a), and the Mach number and flow direction were estimated from the angle of the Mach wave. The shock wave demonstrated through the method depicted in Fig. 5.1(b) has a location and angle similar to the shock wave in Fig. 5.1(a). Two shock waves generated due to the small gap between the window and ramp are depicted in Fig. 5.1(a), starting at the surface of the ramp. These shock waves are demonstrated in the numerical simulation by including the small cavity within the computational domain; thus, these shock waves are also evident in Fig. 5.1(b). However, the angle of the shock wave in Fig. 5.1(b) is larger than that in Fig. 5.1(a). Furthermore, specific 3D effects are not considered in the 2D numerical simulation, such as the bow shock generated from the gap of a circular shape between the circular window installed in the ramp

and the surface of the ramp. Hence, a more realistic 3D numerical analysis is required to adequately compare the angle of the oblique shock wave, which is beyond the scope of this paper.

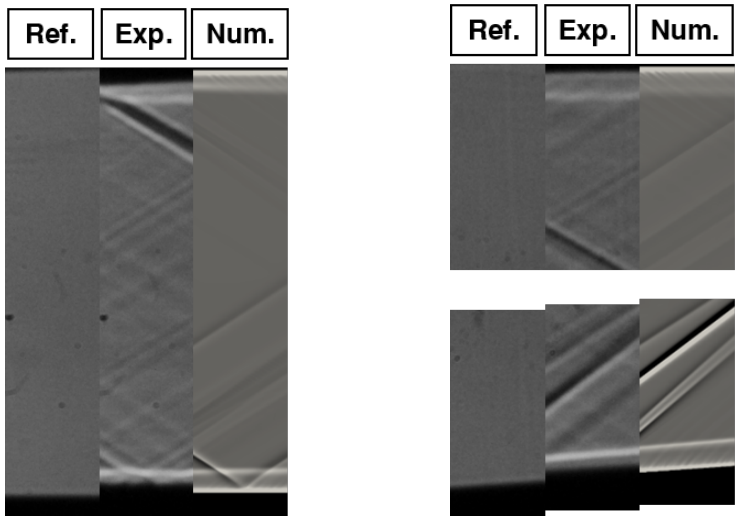

(a) (b)

Figure 5.2: Comparison of the boundary layer, where Ref. represents a shadowgraph image when the wind tunnel is not operating, Exp. signifies a shadowgraph image when wind tunnel is operating, and Num. indicates the synthetic shadowgraph acquired from the numerical simulation. The boundary layer is compared at two locations: (**a**) the boundary layer before the ramp and (**b**) the boundary layer on the ramp.

The boundary layers located before the ramp and on the surface of the ramp in the shadowgraph images are compared in Fig. 5.2, in which the shadowgraph images captured a) before the wind tunnel operation (Ref.) and b) during the wind tunnel operation (Exp.) and c) the synthetic shadowgraph image acquired from the numerical simulation (Num.) are displayed. A comparison of the shadowgraph

images before and during the wind tunnel operation (Fig. 5.2) reveals the differences in the black shadow of the test section. The height of the black shadow increases when the flow is developed.

Luthamn et al. [85] simulated a numerical shadowgraph using the ray-tracing computation and discovered that a dark region forms near the wall because the ray refracts and fails to enter the aperture of the imaging system, resulting in the absence of light. This dark region cannot be observed in the synthetic shadowgraph image; however, the bright line near the edge of the boundary layer depicted in the shadowgraph image captured during the experiment is visible in the synthetic shadowgraph image. Because the height of this bright line is similar between the experimental and numerical results, the boundary layer is verified in the numerical simulation.

5.2 Wavefront Measured with the Shack-Hartmann Wavefront Sensor

The wavefront of the laser beam was acquired using a SHWS. The LOS of the laser beam was 86°, which was perpendicular to the surface of the ramp. The transient OPD maps are depicted in Fig. 5.3. The black dot in each OPD map signifies a dead pixel in the SHWS. The OPD is nondimensionalized with the wavelength of the laser, which is 635 nm. The axis of the test section is depicted in Fig. 2.3. In all OPD maps, the OPD increases in the x-direction. Because the density (i.e., the

index of refraction) is larger behind than in front of the shock wave, the ray in the x-direction passes through a region with a relatively large index of refraction, increasing the OPD, as depicted in Fig. 5.3. Although the ramp is meant to be 2D, the contours of the OPD maps are not parallel to the z-axis, exhibiting a temporal fluctuation in the contour lines, which is likely due to the gap between the window and ramp, generating a complicated 3D flow field including a shear layer and bow shock wave.

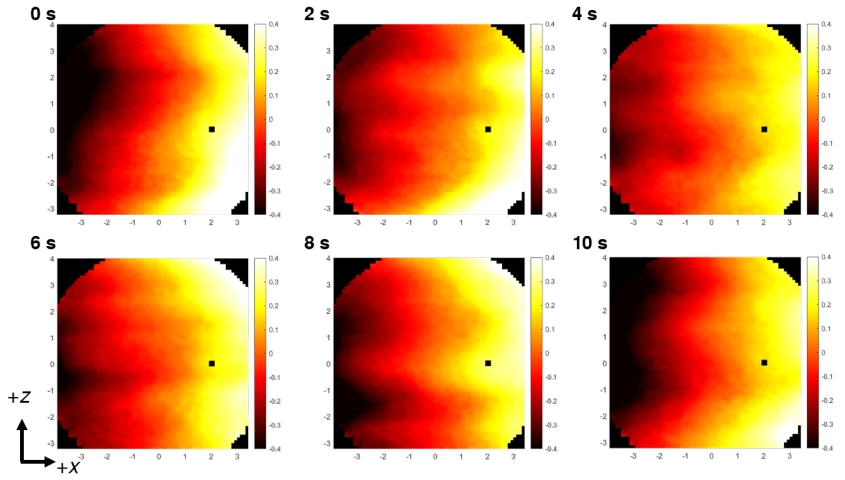

Figure 5.3: Transient optical path difference maps acquired using the Shack-Hartmann wavefront sensor during the wind tunnel experiment.

5.3 Simulation of the Propagation of the Optical Wave

5.3.1 Validation of the numerical simulation result

As described, the aero-optical effects induced by each aerodynamic feature cannot be analyzed using only the wavefront measured using the SHWS. Numerical methods are required for comparing the aero-optical effects induced by the shock wave and boundary layer in the supersonic flow field over the compression ramp. The ray-tracing computation was conducted to obtain the wavefront of the laser beam propagating through the supersonic flow field over the compression ramp. Because the flow field acquired from the numerical simulation is a steady-state solution, the transient OPD maps in Fig. 5.3 are time-averaged. The time-averaged OPD map is presented in Fig. 5.4(a), and the OPD map obtained from the ray-tracing computation is depicted in Fig. 5.4(b).

The OPD obtained from the ray-tracing computation is 1D in the x-direction; thus, it is duplicated and extended along the z-axis to obtain a 2D OPD map, as illustrated in Fig. 5.4(b). In Fig. 5.4(a), the small-scale structures inside the OPD map cannot be observed. Moreover, the curved contour lines of the OPD map are more evident than those in the transient OPD maps owing to the window in the

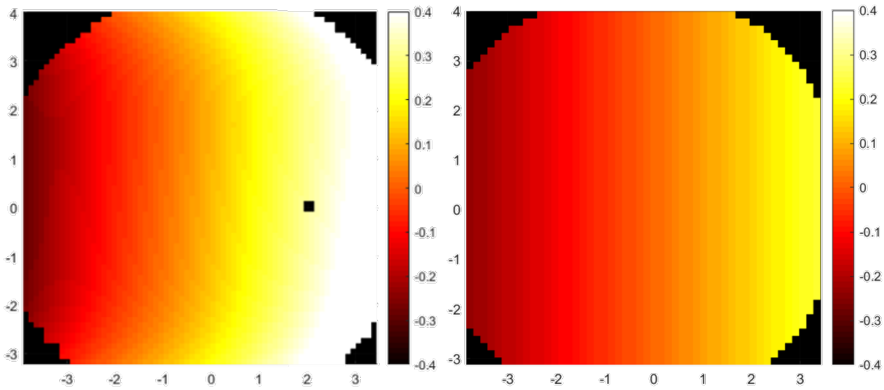

(a) (b)

Figure 5.4: Comparison of optical path difference (OPD) results: (**a**) time-averaged OPD acquired from the experiment and (**b**) OPD obtained from the ray-tracing computation.

ramp. These curved contour lines are not depicted in Fig. 5.4(b) because the flow field acquired from the numerical simulation is 2D. The overall OPD from the ray-tracing computation is less than that from the experiment, likely because of the wind tunnel vibration and 3D flow features, which cannot be demonstrated.

The deflection angle was studied along the ray in the center of the laser beam to compare the aero-optical effects due to the shock wave and boundary layer. The deflection angle is defined as the difference from the initial ray angle. The deflection angle and density along the ray are plotted in Fig. 5.5, in which the locations of the two boundary layers and the shock wave are indicated. Because an adiabatic wall condition is used, a large density gradient exists on each wall, and the

gradient of the density at the boundary layer is larger than that of the shock wave. However, the deflection angle due to the shock wave is larger than that due to the boundary layer. Thus, even if the density change at the boundary layer is considerable, the deflection due to the shock wave is stronger than that due to the boundary layer. However, the deflection angle due to the shock wave is greater than that due to the boundary layer. Consequently, the shock wave causes a greater deflection of the wavefront of the laser beam than the boundary layer because of the angle between the direction of the ray and the direction of the gradient of the density.

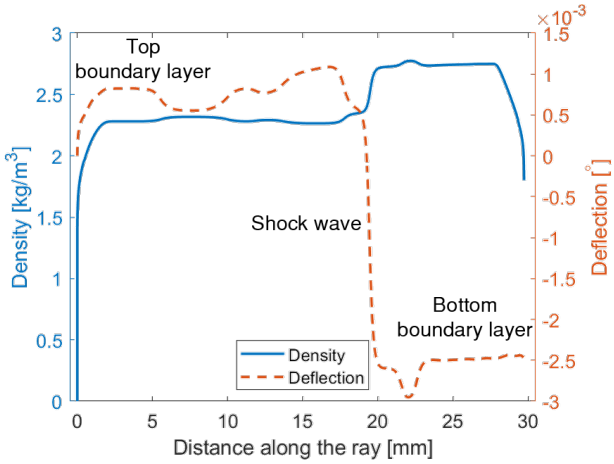

Figure 5.5: Deflection angle and density along a ray propagating through the center of a laser beam.

Because the gradient of the density along the y-direction is greater than that along the x-direction in the boundary layer, the boundary layer could be modeled as a series of regions that are parallel to the

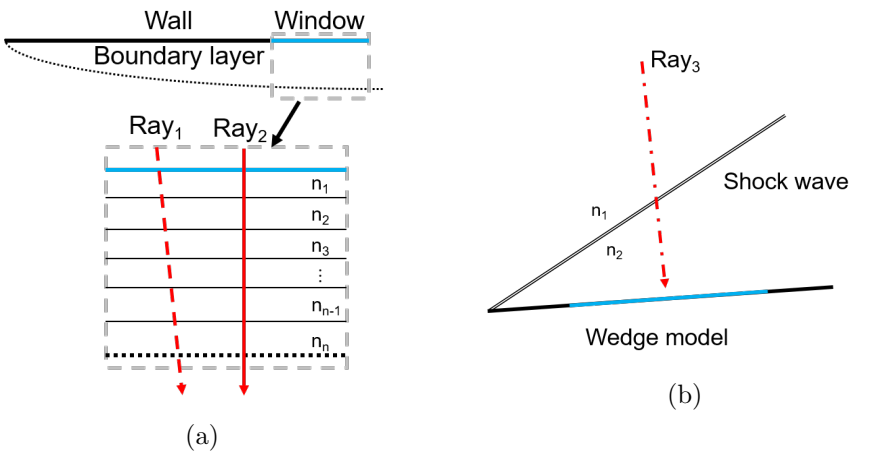

Figure 5.6: Schematic of the ray propagating through: (**a**) the boundary layer and (**b**) the shock wave.

wall with the linearly varying index of refraction, as depicted in Fig. 5.6(a). If the ray is propagating through these regions in a direction perpendicular to the window, as with Ray_2 in Fig. 5.6(a), the deflection angle (which can be calculated using Snell's law) is negligible. Because the ray is tilted from this perpendicular direction, the deflection angle of the ray is larger. However, if the angle of the tilt is not significant, as with Ray_1 in Fig. 5.6(a), then the deflection angle of the ray is not significant. The shock wave could be modeled as two regions with different indices of refraction, as depicted in Fig. Fig. 5.6(b). Considering Snell's law, if the ray propagating through the shock wave is perpendicular to the shock wave surface, then the deflection is negligible. Because the ray is tilted from the perpendicular direction, the deflection of the ray is larger. If the tilt angle of the ray is large, as with Ray_3 in Fig. Fig. 5.6(b), then the deflection angle

due to the shock wave is significant. Because the initial direction of the ray is normal to the surface of the ramp, a) the direction of the ray propagating through the top boundary layer is similar to Ray_1, b) the bottom boundary layer at the surface of the ramp is similar to Ray_2, and c) the shock wave is similar to Ray_3. Thus, the deflection angle due to the top boundary layer is lower than that due to the shock wave, and the deflection angle at the bottom boundary layer is negligible, as depicted in Fig. 5.5.

5.3.2 Effect of the refraction due to windows

To analyze the disturbance due to the refraction of the test section window and model window, numerical simulation was conducted considering the refraction due to the windows, as described in Section 3.3. The thickness and refractive index of the windows were neglected, and only the refraction due to the difference between the flow and atmosphere was considered. The OPDs of the numerical simulations with and without the refraction due to the windows are depicted in Fig. 5.7. As the refraction due to the windows was included, the PV OPD increased. However, the increment was not very large at about 0.01λ. This is also quite negligible compared to the difference between the experimental and simulation results. The reason for the small deflection at the windows is due to the similar refractive index of the flow field and the atmosphere for the current test conditions. If the Mach

number increases and the density inside the test section decreases, the difference of the refractive index between the flow field and the atmosphere will increase; thus, the reftraction due to the windows will increase and cannot be neglected. The effect of the window at higher Mach number will be discussed in Section 6.4.2. However, for current flow condition, the refraction due to the windows was neglectable and not be considered for the following analysis.

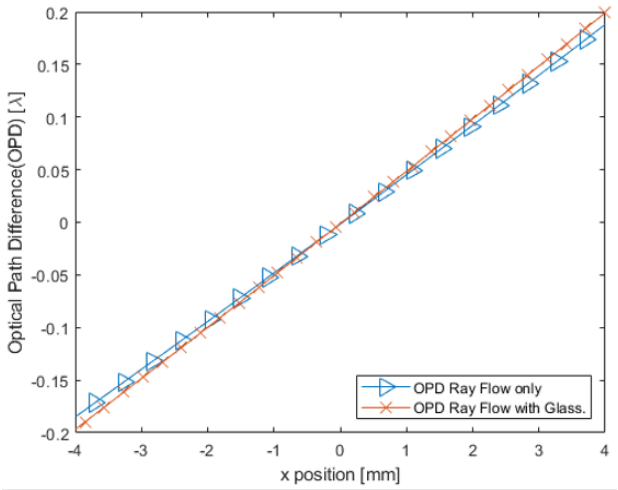

Figure 5.7: Comparison of the optical path difference (OPD) with and without refraction due to the windows.

5.3.3 Deflection along the ray depending on the line of sight

The ray-tracing method was conducted by varying the LOS. As illustrated in Fig. 5.8, due to the size of the computational domain, the

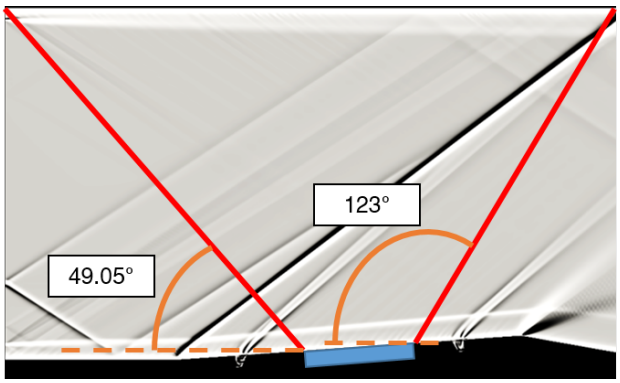

Figure 5.8: Limitation of the line of sight that can be calculated through the ray-tracing method.

limitation of the LOS was 49.05°to 123°. Thus, several LOS between 50°and 120°were calculated, and the contributions of the shock wave and boundary layer were investigated for each LOS. The deflection angle and density along a ray propagating through the center of the laser beam for each LOS is depicted in Fig. 5.9. Because the total length of the rays was different for each LOS, the distance along the rays were all nondimensionalized with the total length of each ray. Because of the nondimensionalization of the distance the location of shock wave and boundary layer are different for each LOS in Fig. 5.9. In Fig. 5.9, the density variation at the shock wave is small compared to the boundary layers. At an LOS of 50°, which is shown in Fig. 5.9(a), the deflection due to the boundary layer is as great as 0.01°, whereas the deflection due to the shock wave is very small, almost neglectable. The reason for the small deflection due to the shock wave is that the incident angle of the ray is almost perpendicular to the

shock wave. Thus, as in Eq. 3.11, the refraction due to shock waves was quite small. As the LOS increases, the deflection due to shock wave increases. At 120°, the deflection due only to the shock wave is as great as -0.015°. As the LOS increases, the deflection due to the boundary layers on both the top and compression ramp decreases, and then changes direction and increases again in that direction. The deflection due to each boundary layer are minimum when the incident angle of the ray is perpendicular to each surface. Thus, deflection due to top boundary layer is minimum when LOS is 90°, while for the boundary on the compression ramp, the minimum delfection appears when LOS is 86°.

To compare the deflection angle depending on the LOS, the final deflection angle for each LOS is plotted in Fig. 5.10. The magnitude of the deflection is also plotted in Fig. 5.10 to neglect the direction and consider the number of instances of the aero-optical phenomena. The magnitude of deflection is minimum near the LOS of 70°, which is 0.0003°. It does not mean that the aero-optical phenomena occur less in this condition, but the deflections due to the boundary layers and shock wave cancel each other out and act like little aero-optical phenomena occur. As the LOS increases, the deflection angle increases rapidly rather than gradually.

For further analysis, Eq. 3.11 is adopted to calculate the refraction due only to shock waves depending on the LOS. Assuming that the

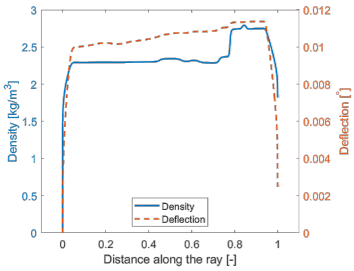

(a) 50°

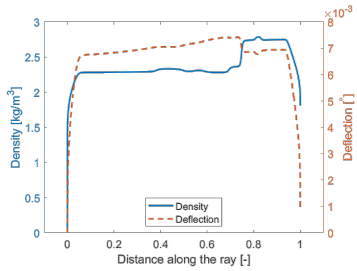

(b) 60°

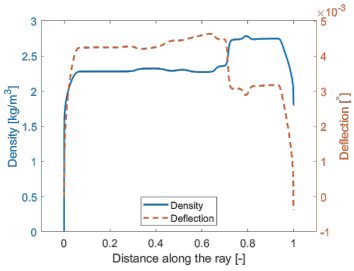

(c) 70°

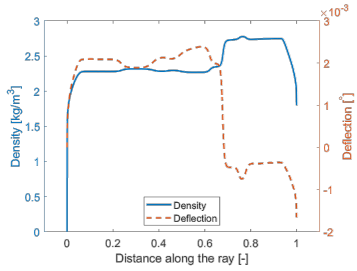

(d) 80°

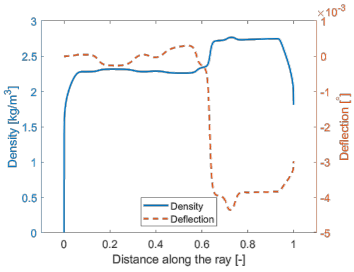

(e) 90°

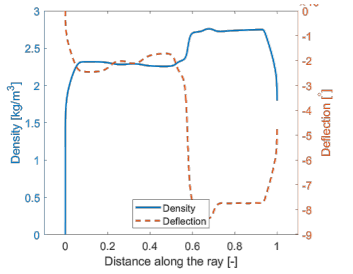

(f) 100°

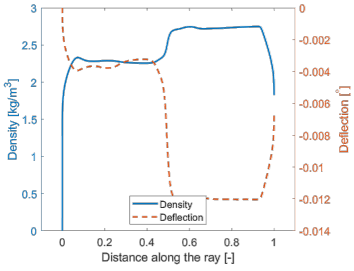

(g) 110°

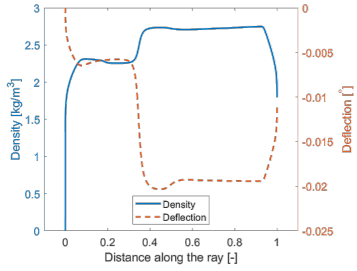

(h) 120°

Figure 5.9: Deflection angle and density along a ray propagating through the center of the laser beam for different line of sight.

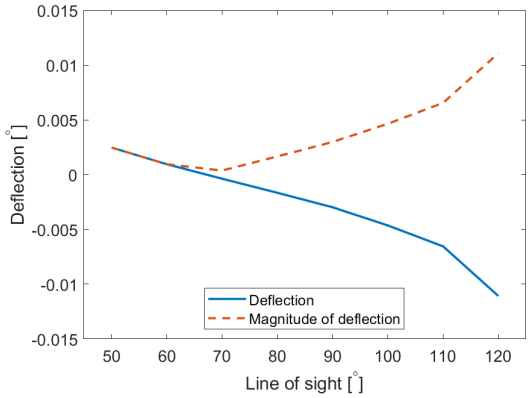

Figure 5.10: Deflection angle due to the flow field depending on the line of sight.

flow is Mach 2, the oblique shock wave formed at a 4°wedge is 33.39°. The flow conditions used for the calculation are $p_0 = 0.72$ Mpa, and $T_0 = 300$ K. The deflection due to the shock wave depending on the LOS is plotted in Fig. 5.11. An angle between 10°and 140°was calculated. Beyond 140°, the light is parallel or below the shock wave; thus, it was not considered in the calculation. The direction of deflection changes near the LOS, where the incident angle of the ray is perpendicular to the shock wave. The calculation of the deflection due to the shock wave is compared with the numerical simulation result in Fig. 5.12. In Fig. 5.12, the deflection due to the overall flow field and the deflection due to the shock wave are similar. Thus, in the current experimental setup where the laser beam propagates through two boundary layers, the shock wave is dominant for the aero-optical phenomena in the flow field over the compression ramp.

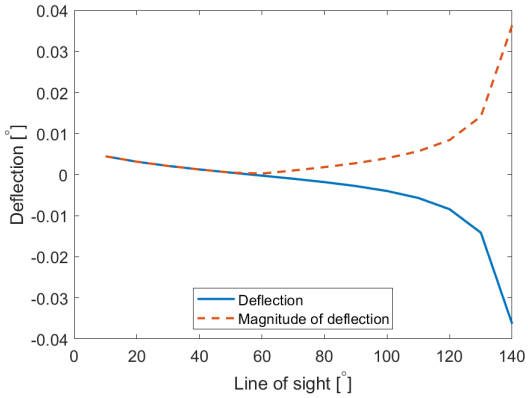

Figure 5.11: Deflection due to the shock wave calculated using Snell's law.

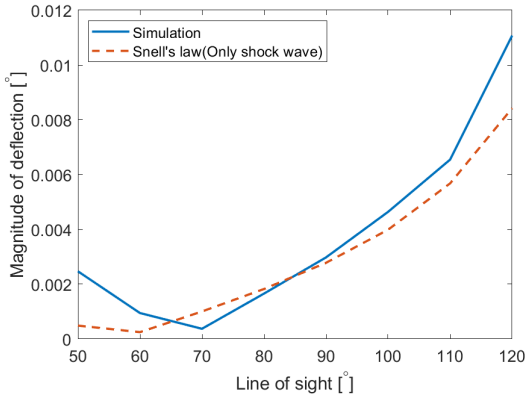

Figure 5.12: Comparison of the magnitude of deflection due to the flow field (numerically simulated) and shock wave (calculated using Snell's law).

5.3.4 Numerical simulation with slip conditions on the top wall

In the current optical measurement system, the laser always passes through two boundary layers that have opposite aero-optical effects. However, the seekers during flight only have one boundary layer over the window. Therefore, the simulation is conducted to exclude one boundary layer and compare only the shock wave and the boundary layer over the ramp. This was conducted by setting the top wall with slip conditions. The simulation result with slip conditions on the top wall is presented in Fig. 5.13. As depicted in Fig. 5.13, the top boundary layer disappeared in the flow region. To compare the individual contribution of the shock wave and boundary layer, ray-tracing was conducted using several LOSs. The deflection along the center rays for each LOS is illustrated in Fig. 5.14. In Fig. 5.14, density mainly varies due to shock wave and boundary layer on the ramp surface. The significant change of density near the top wall is due to the error during the extraction of the density at the center rays. The final deflection for each LOS is displayed in Fig. 5.15, where the trend is completely different from that of Fig. 5.10. The point where the slope changes shifted to a higher LOS. In addition, the magnitude of the deflection increased, especially when the LOS lowered. As discussed, this region is where the deflection due to the shock wave is small. The shock wave effect was also calculated using Snell's law for different

LOSs. The analytical and numerical solutions are compared in Fig. 5.16.

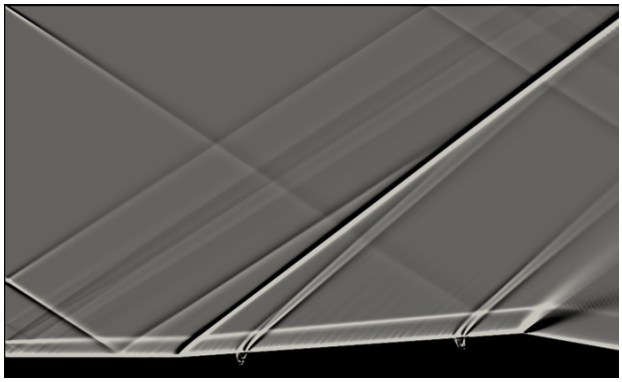

Figure 5.13: Synthetic shadowgraph image of the numerical simulation with slip conditions on the top wall.

In Fig. 5.12, the analytical solution is similar to the simulation result, meaning the shock wave is dominant and boundary layer seems to have little aero-optical effect, whereas Fig. 5.16 reveals that the effect of the boundary layer is not small. The point where the two lines in Fig. 5.16 correspond is a LOS of 90°, which is the condition in which the boundary layer effect has the lowest effect; thus, Snell's law is appropriate to estimate deflection due to shock wave. Furthermore, the direction of the deflection is coincident for all of the line of sight. Considering that the magnitude of deflection increases as the LOS decreases below 90°, the aero-optical effects at lower LOS than 90°can be estimated to be significant. Through the simulation of the slip condition on top, the aero-optical effects due to the shock wave and

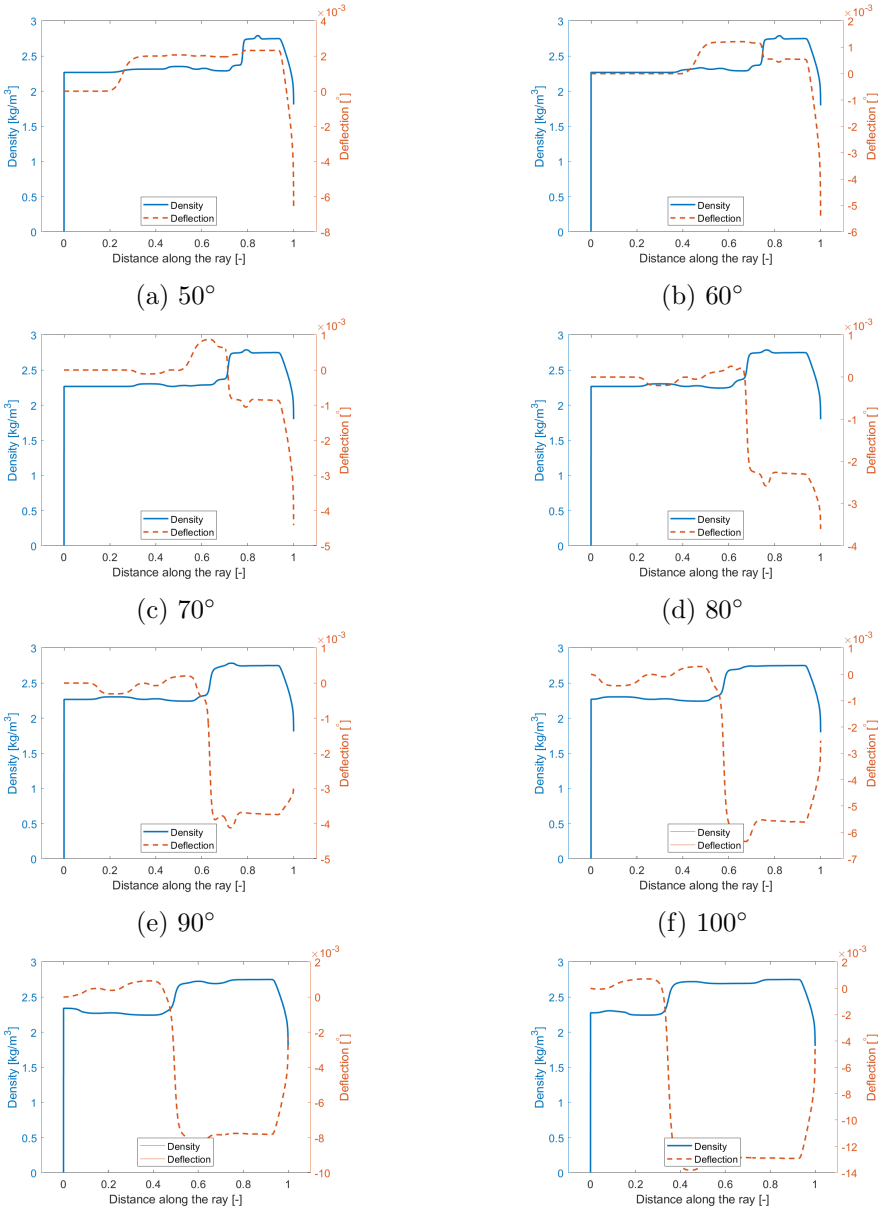

(a) 50° (b) 60°

(c) 70° (d) 80°

(e) 90° (f) 100°

(g) 110° (h) 120°

Figure 5.14: Deflection angle and density along a ray propagating through the center of the laser beam for different line of sight with the top wall slip condition.

boundary layer are significant. Moreover, because the current optical measurement system must pass two boundary layers, which cancel each other out, special experiment methods, such as the laser-induced breakdown method, should be adopted, where the light source could be generated in the middle of the flow field.

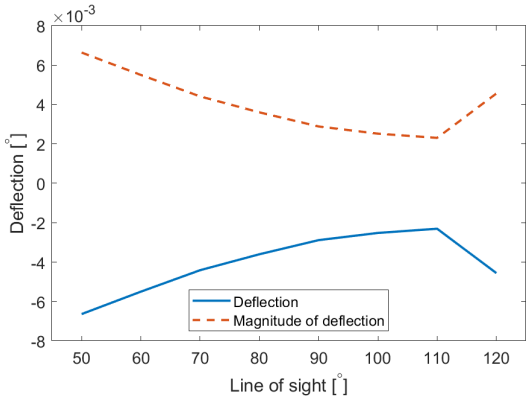

Figure 5.15: Deflection angle due to the flow field depending on the line of sight with slip conditions on the top wall.

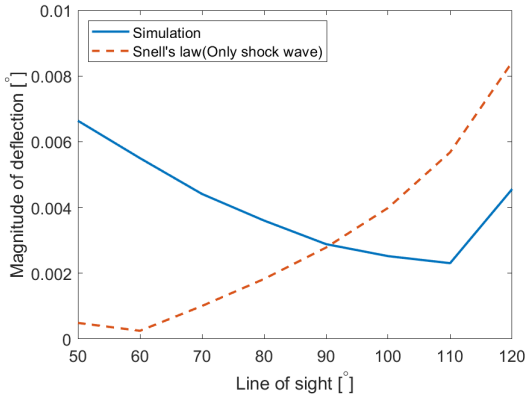

Figure 5.16: Comparison of the magnitude of the deflection due to the flow field (numerically simulated) and shock wave (calculated using Snell's law) with slip conditions on the top wall.

Chapter 6

Aero-optics in Hypersonic Flow

In this chapter, the aero-optical phenomena in hypersonic flow over a wedge are described. In the first part of the chapter, the experimental conditions and the flow field over the hypersonic wedge are described. The results of the shock tube measurement and flow visualization are presented. In the second part of the chapter, the wavefront measurement results are described. The results of the SHWS and the optical parameters are discussed. In this chapter, some of the work has been previously presented at the 31st ISSW [74].

6.1 Flow Conditions for the Hypersonic Experiment

For the hypersonic experiment, the shock tunnels were operated for two different flow conditions: high and low density. The details of the hypersonic flow conditions are described in Table 6.1. In Table 6.1,

- p_4 denotes the measured pressure of the driver gas, which is nitrogen;
- p_1 denotes the measured pressure of the driven gas, which is air;
- p_0 denotes the stagnation pressure measured right before the nozzle;
- T_0 denotes the stagnation temperature calculated with shock tube theory using the measured pressure data; and
- ρ_0 denotes the stagnation density calculated using the perfect gas law using p_0 and T_0.

Assuming the nozzle flow as isentropic expansion, the stagnation conditions of the low-density cases expands to a Mach 7 flow with the static pressure, temperature, and density of 408 Pa, 69 K, and 0.0325 kg/m^3, respectively. Considering only the density, this is the flight conditions at 39.6 km. For the high-density case, the static pressure, temperature, density, and flight altitude are 773 Pa, 58 K, 0.0728 kg/m^3, and 21.7 km, respectively.

The typical measurement of the pressure along the shock tube is plotted in Fig. 6.1. Six pressure sensors were installed along the shock tube, and the sixth sensor (Sensor 6) was installed right before the nozzle. The pressure rises once as the shock wave is generated and propagated through the shock tube. Then, as the shock wave is reflected, the pressure rises once more for Sensors 5 and 6. Similar to the pressure data for Sensor 6, the stagnation pressure was established for about 3 ms. The wavefront sensor measurements were acquired during this established flow region.

6.2 Hypersonic Flow Field Around a Wedge

Because the experimental models for the hypersonic experiment are installed at the visualization window as depicted in Fig. 2.11(a), the flow cannot be visualized in the current experimental configuration. Thus, to identify the angle of the shock wave generated over the wedge and determine whether any other disturbance occurs on the flow field, the structure is designed to install a wedge inside the test section to

Table 6.1: Flow conditions for the low- and high-density case of the hypersonic experiment; p_4 denotes the pressure of the driver tube; p_1 denotes the pressure of driven tube; p_0 denotes the stagnation pressure; T_0 denotes the stagnation temperature; and ρ_0 denotes the stagnation density.

	p_4 [MPa]	p_1 [MPa]	p_0 [MPa]	T_0 [K]	ρ_0 [kg/m^3]
Low	7.2	0.1	1.69	745.3	7.9
High	12.3	0.3	3.2	631.2	17.7

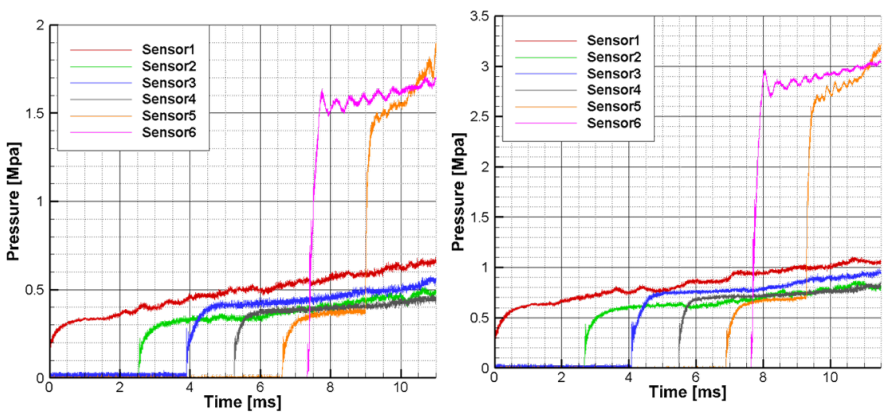

Figure 6.1: Pressure measured along the shock tube: (**a**) low density and (**b**) high density.

visualize the flow field, which is shown in Fig. 6.2. Several experiments were conducted to visualize the flow using the conventional shadowgraph technique, and one of the flow visualization results is illustrated in Fig. 6.3. As the flow is established inside the test section, the flow appears steady during the test time. The thin boundary layer is shown near the wedge. The shock wave was generated at the tip of the wedge. The analytical solution of the shock angle for the 12°wedge in Mach 7 flow is 18.4°. The angle of the shock wave in the shadowgraph measured at 18.5°, which is similar to the analytical solution. Thus, the flow over the wedge seems to be established as expected. A small disturbance seems to occur at the end of the window, but because the laser beam does not pass this region, this disturbance was neglected during the analysis. The flow field around the wedge in the experi-

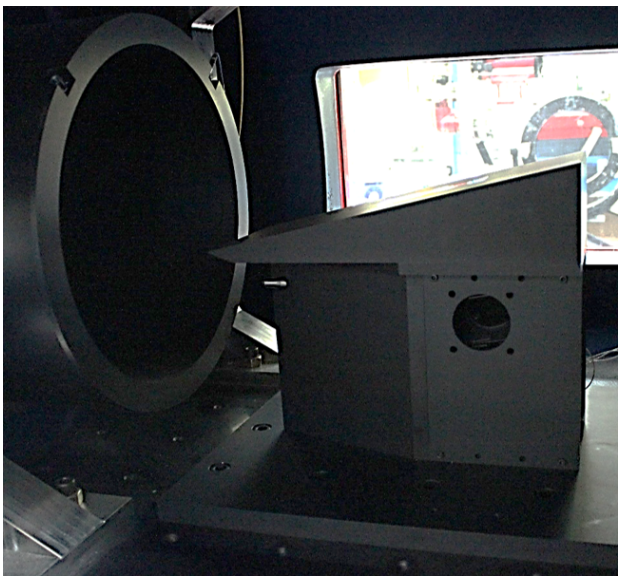

Figure 6.2: Wedge installed for flow visualization.

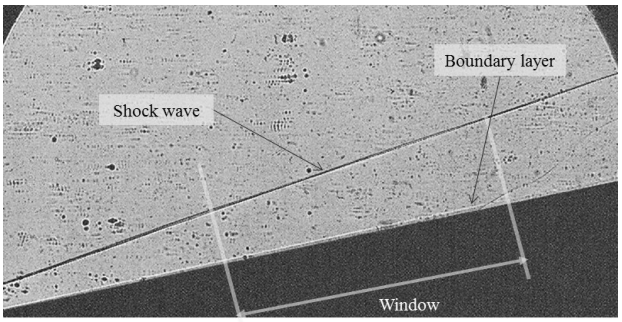

Figure 6.3: Flow visualization of the hypersonic flow around the wedge.

mental configuration in Fig. 2.11(a) is expected to be like the flow field visualized in Fig. 6.3.

6.3 Wavefront Measurement in the Hypersonic Wedge Flow

The wavefront of the laser beam propagating through the flow field is measured using a SHWS. The incident angle is perpendicular to the wedge surface, which is 12°. As discussed regarding the supersonic compression ramp flow, at this incident angle, the aero-optical phenomena due to the boundary layer on the wedge surface are expected to be neglectable. Thus, the aero-optical effects due to the boundary layer on the up-plate, shock wave, and turbulence of the flow are expected to distort the wavefront in the hypersonic flow experiment. As described in Section 2.3.2, the SHWS can acquire one image per operation. A trigger signal was adjusted to acquire the data in the middle of the steady-state conditions inside the test section by recording the signal triggering the SHWS and the stagnation pressure inside the test section together. The stagnation pressure inside the test section was measured using a pitot tube, which was installed behind the wedge. The coordinates of the wavefront measurement for the hypersonic flow are illustrated in Fig. 6.4.

For the low-density flow, 15 runs were conducted and 13 images of the wavefront are obtained. For the high-density flow, 16 runs were conducted and 15 images of wavefront were obtained. Even if the pressure when the diaphragm burst was slightly different, the runs for

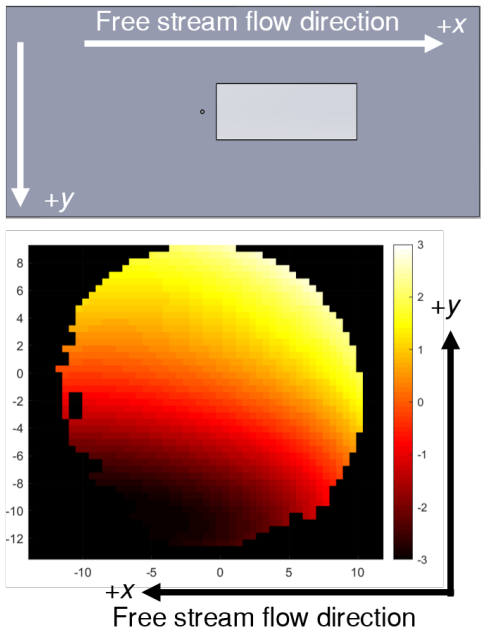

Figure 6.4: Coordinates of the optical path difference map measuring hypersonic flow.

each condition are assumed to have a similar flow field. Among these wavefront results, several OPD contours were selected and are shown in Fig. 6.5. Two OPD contours were selected for each case, which have the minimum and maximum average tilt in the x-direction. The x-direction is selected because it is the direction of the flow where a large density variation is expected due to the shock wave. Comparing four of the OPD contours, there seems to be a gradient in one direction, but this direction seems unmatched. Only the minimum OPD contours for each condition have a similar shape of the contour and the same direction of the gradient. Especially, 6.5(b) depicts the opposite

direction of the gradient compared to the other three contours. Furthermore, the directions of the gradients in the contour maps are all in the y-direction rather than the x-direction, even if $tilt_x$ is considered for the selection. However, because the wedge model is 2D, the density variation in the flow field must be dominant in the x-direction, which does not match Fig. 6.5, which has all gradients in the y-direction.

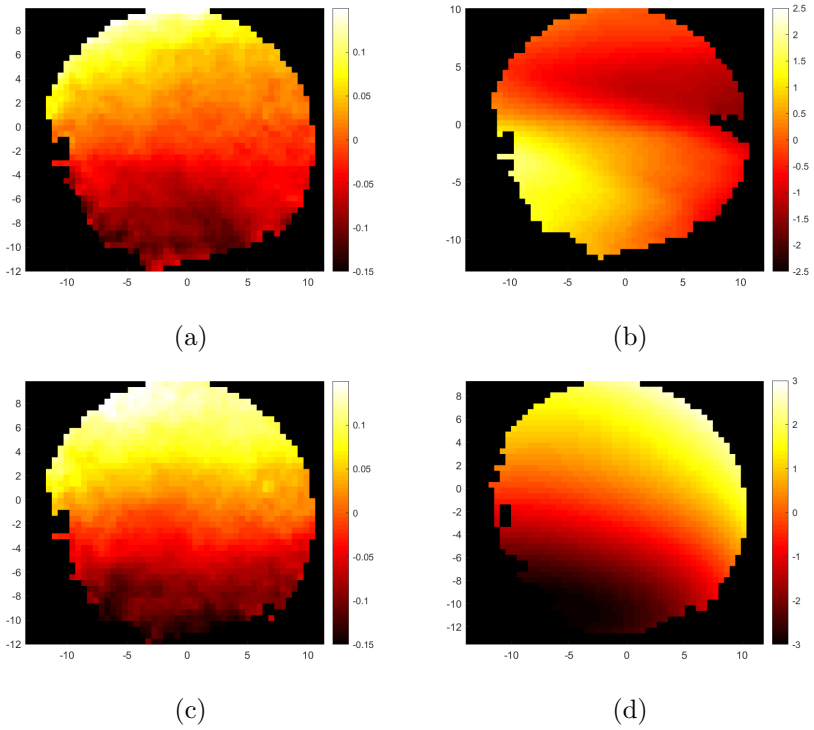

Figure 6.5: The optical path difference contours obtained using the Shack-Hartmann wavefront sensor: (**a**) minimum $tilt_x$ for low density, (**b**) maximum$tilt_x$ for low density, (**c**) minimum $tilt_x$ for high density, and (**d**) maximum $tilt_x$ for high density.

Two possible reasons exist for this. First, the laser beam expander is tilted in the y-direction, which results in a slight incident angle in the y-direction. Second, the wedge model is not aligned axially, and the flow field is 3D rather than 2D. To neglect the deflection along the y-direction, OPDs are reconstructed considering only the x-tilt term of the Zernike polynomials and are shown in Fig. 6.6. Comparing all runs, some OPD contours are in the opposite direction from the x-direction gradient. Further analysis on this opposite direction of the gradient is conducted using numerical simulations.

To identify the trends of the OPD contours, several optical parameters were extracted for all runs of low- and high-density cases. First, the PV OPD and OPD_{rms} were compared in Fig. 6.7. The PV OPD reveals the overall distortion of the wavefront, and OPD_{rms} is usually related to the turbulence of the flow field. In Fig. 6.7, the optical parameter extracted from the tilt-removed OPD is also represented. Removing the average tilt from the OPD excludes the aero-optical effects due to the bulk refraction and noise of the tunnel. Thus, tilt-removed data cannot be used to analyze the deflection due to the shock wave but are appropriate for the analysis of the turbulence in the flow. Figure 6.7(a) depicts the noisy data for both conditions. Furthermore, PV OPD and OPD_{rms} of the high-density condition are smaller than the low-density condition. The averaged PV OPD and OPD_{rms} for the high-density flow were 0.33λ and 0.024λ, respectively, whereas,

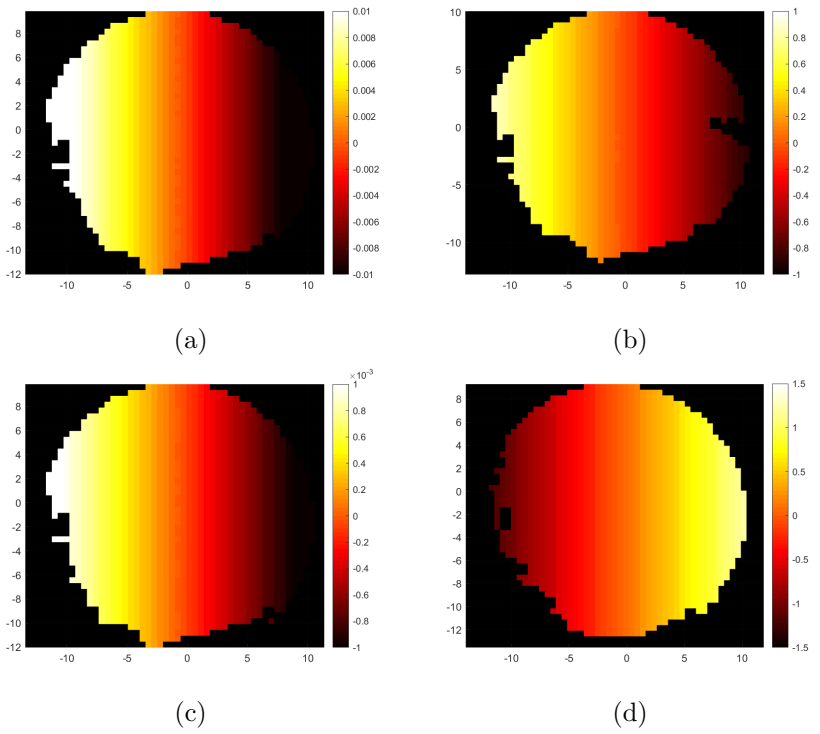

Figure 6.6: The optical path difference contours reconstructed with only the x-tilt term of the Zernike polynomials: (**a**) minimum $tilt_x$ for low density, (**b**) maximum $tilt_x$ for low density, (**c**) minimum $tilt_x$ for high density, and (**d**) maximum $tilt_x$ for high density.

for low density-flow, they were 0.497λ and 0.027λ, respectively. Thus, the averaged value was also much larger for the low density.

To evaluate this tendency, the refraction due to the shock wave was analytically calculated using Eq. 3.11. Using the values in Table 6.1 and a shock angle of 18.4°, the deflection due to the shock wave at a low-density flow was -5.5855×10^{-5}°, whereas, at a high-

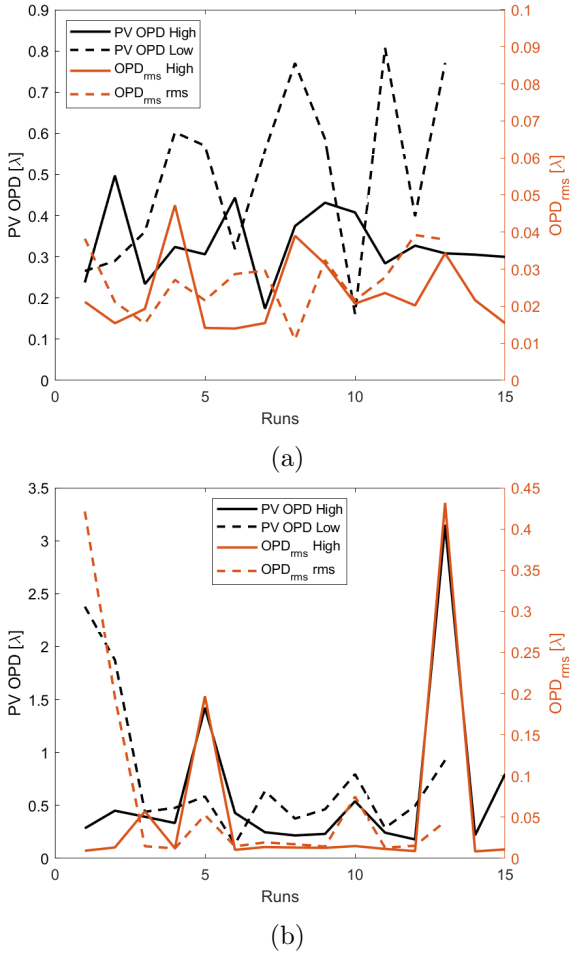

Figure 6.7: The peak-to-valley (PV) optical path difference (OPD) and OPD_{rms} measured using the Shack-Hartmann wavefront sensor: (**a**) tilt not removed and (**b**) tilt removed.

density flow, it was $-1.3118 \times 10^{-4\circ}$. The corresponding PV OPDs to these deflections were 0.0531λ and 0.1190λ, respectively. Thus, the low-density flow is expected to induce less aero-optical effects than the high-density flow, according to the analytical solution. However,

in the measurement results, the opposite tendency occurred, and the high-density flow induced the smallest aero-optical effect. Moreover, comparing the analytical PV OPD and averaged PV OPD, the low-density flow exhibited 89% error, whereas the high-density flow exhibited a 64% error. Thus, not only the aero-optical effect due to the shock wave but also other disturbances, such as the vibration of the facility, debris in the diaphragm, the tilt in the alignment, and so on interfere with the measurement results. Especially, the peak points in Fig. 6.7(b) are too large compared to other tilt-removed results. The peak points have large disturbances.

The tilt and the Strehl ratio were also investigated for the low- and high-density flow, as plotted in Fig. 6.8. The tilt and Strehl ratio were also noisy. The average $tilt_x$ and $tilt_y$ for low density was 6.1 μrad and -12.6 μrad, respectively, whereas, for high density, the values were 9.6 μrad and 9.7 μrad, respectively. The magnitude of the tilt for low density is 14.0 μrad and for high density is 13.7 μrad. In previous studies by Yanta et al. [52], the BSE due to the Mach 7 flow over a 15°wedge model was 5 to 35 μrad. The measurement results are within this range. Although the density of the free stream flow in Yanta's work is much smaller than the current conditions, the measurement results seem reliable. The analytical calculation was converted to the tilt: for low density at -0.97 μrad and for high density at -2.29 μrad, which are much lower values than the measured results. Similar to

the OPD results, high density has a smaller tilt than low density. The average of the Strehl ratio for low density was 0.85 and for high density was 0.87, which also shows a similar tendency.

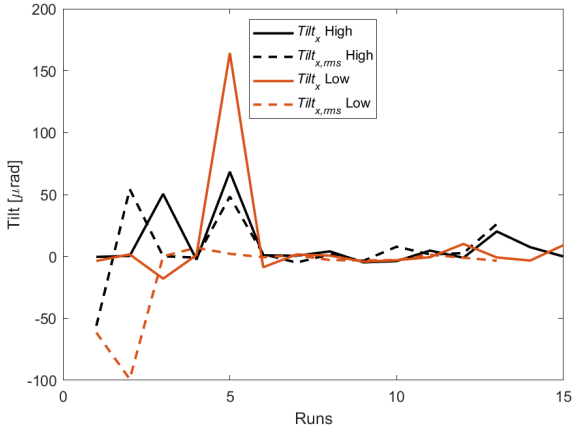

(a)

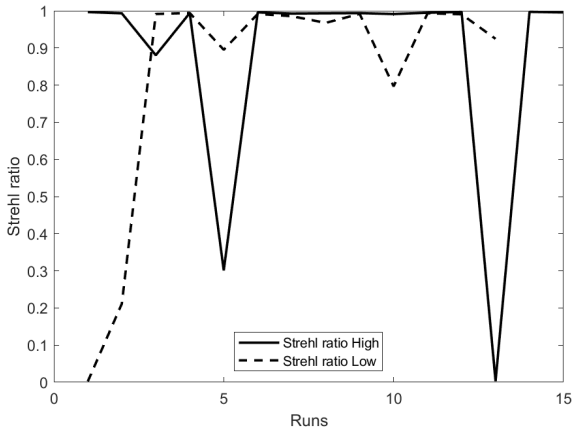

(b)

Figure 6.8: Tilt and Strehl ratio measured using the Shack-Hartmann wavefront sensor: (**a**) tilt in the x- and y-directions and (**b**) the Strehl ratio.

6.4 Numerical Simulation for Hypersonic Wedge Flow

6.4.1 Numerical simulation considering only the flow field

Numerical simulation was also conducted for the hypersonic flow to analyze the experimental results and evaluate the individual contributions of the shock wave and boundary layer. The numerically simulated flows are shown in Fig. 6.9, where the synthetic shadowgraph results for the low and high-density cases are presented. Two results do not exhibit much difference, and a weak shock wave was observed at the up-plate for both cases. The angle of the shock wave is similar to the flow visualization result in Fig. 6.3. Weak shocks are illustrated in Fig. 6.3 near the window at the wedge were neglected and were not demonstrated in the flow simulations. Because the up-plate was not installed during the flow visualization experiment, the weak shock in Fig. 6.9 is not visualized in the flow visualization results. Similar to the supersonic flow, the ray-tracing computation was conducted using the flow simulations, and the results are presented in Fig. 6.10. The directions of the contours were opposite the measurement results. Moreover, the order of the OPD is 100 times smaller, even for the minimum OPD cases. The OPD of the low-density case is half of that in the high-density case, which has a similar trend as the analytical

solution.

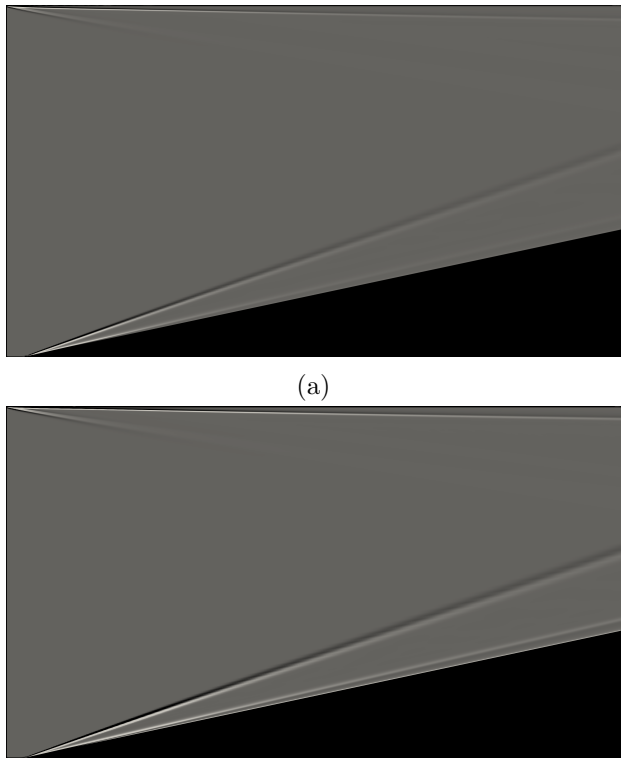

(a)

(b)

Figure 6.9: Numerical simulation results for the hypersonic flow: (**a**) low-density case and (**b**) high-density case.

6.4.2 Effect of refraction due to windows

Assuming that the reference wavefront of the laser beam is acquired when the pressure of the test section is 120 Pa during the vacuum process, the refraction due to the windows was considered, as described

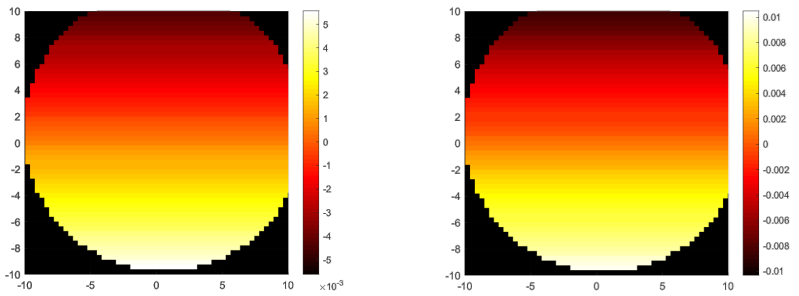

(a) (b)

Figure 6.10: The optical path difference map obtained from numerical simulations: (**a**) low-density case and (**b**) high-density case.

in Section 3.3. The OPD contour of the simulations considering the refraction of the windows is depicted in Fig. 6.11. Comparing with the numerical simulations considering only the flow field, the direction of the gradient of the OPD contours changed to the opposite direction. In addition, the value of the OPD increased 10 times more when the refraction due to the windows was considered. Thus, the effect of refraction due to the windows was bigger than the supersonic flow, where OPD only slightly changed.

The main cause of this massive change in the OPD seems to be due to the lower density of the flow field compared to the surrounding atmosphere. Because the refraction due to the windows is larger than the refraction due to the flow field, the randomness of the direction and value of the OPD measured using the SHWS might have occurred due to the aerodynamical vibration on the up-plate and wedge. Due

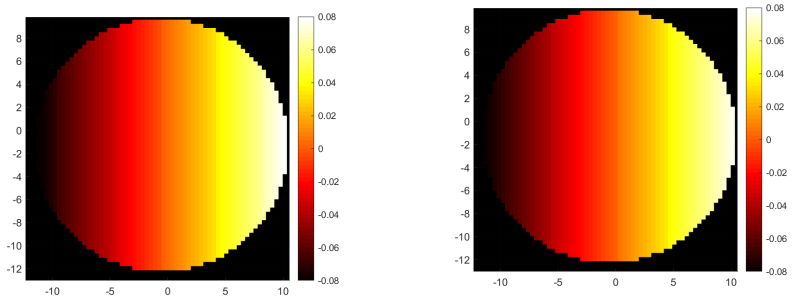

(a) (b)

Figure 6.11: The optical path difference map obtained from numerical simulations considering the refraction due to the windows: (**a**) low-density case and (**b**) high-density case.

to the vibration, the angle of the windows might have changed slightly resulted in different refraction angle due to the windows.

To identify the sensitiveness of the angle of the window on the deflection of the laser beam, the window at the wedge was inclined at a certain range, and the resulting deflection of the ray was simulated as depicted in Fig. 6.12. In this simulation, the flow field was assumed to be steady, and only the window was inclined. Simulations with different inclination of the wedge are conducted only for the high-density case. For only a 0.1°inclination of the window, the deflection increased 40 times and even changed the direction of the x-tilt depending on the direction of the inclination. This deflection due to the windows can explain the difference of the magnitude between the OPD simulated witout the windows and the OPD measured during the experiments. Furthermore, the randomness of the direction of the measured OPD

might have occured due to the random inclination of the wedge induced by the aerodynamical vibration. If the laser beam expander and SHWS were installed inside the vacuum chamber, and the laser beam only propagates through low-density air, then the effect of the refraction due to the windows is neglectable, and only the aberration due to the flow field can be measured. However, in the current wavefront measurement system, the refraction due to the windows seems to dominate the experiment results. Even if the effect of the refraction due to windows is huge, further simulations are performed neglecting the refraction due to the windows because the focus is on the comparison of the aero-optical effects due to the flow features.

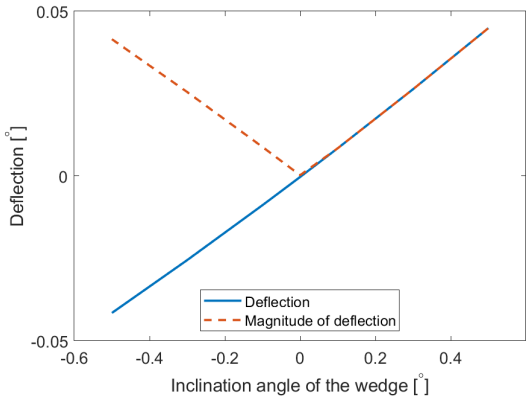

Figure 6.12: Simulated deflection of the center ray depending on the inclination angle of the wedge when refraction due to windows are considered.

6.4.3 Deflection depending on the line of sight

The individual contributions of the shock wave and boundary layer were also studied for the hypersonic flow by extracting the results along the center ray. The deflection along the mid-ray for different LOSs is presented in Fig. 6.13 for the low-density case and in Fig. 6.14 for the high-density cases. Similar to the supersonic case, the deflection due to the boundary layers canceled each other out. The deflection due to the up-plate boundary layer was minimum at a LOS of 90°, a shock wave of 70°, and a wedge boundary of 80°, which are the perpendicular propagations for each flow feature. This trend can be explained using the same theory for the supersonic case. The difference between the low-density case and high-density case is the magnitude, and the profiles were almost similar for each LOS, except at 70°. The final deflection depending on the LOS is presented in Fig. 6.15. The minimum deflection is at a LOS of 70°, which is when the light passes through the shock perpendicularly. Thus, as in supersonic flow, when there are two boundary layers, the shock wave has a more dominant aero-optical effect. For further analysis, Snell's law was used to calculate the refraction due to the shock wave depending on the LOS. The results are depicted in Fig. 6.16, and the analytical solution using Snell's law and the simulation results were almost similar. Thus, as the boundary layers canceled out in this optical configuration, and the shock wave exhibited dominant effects.

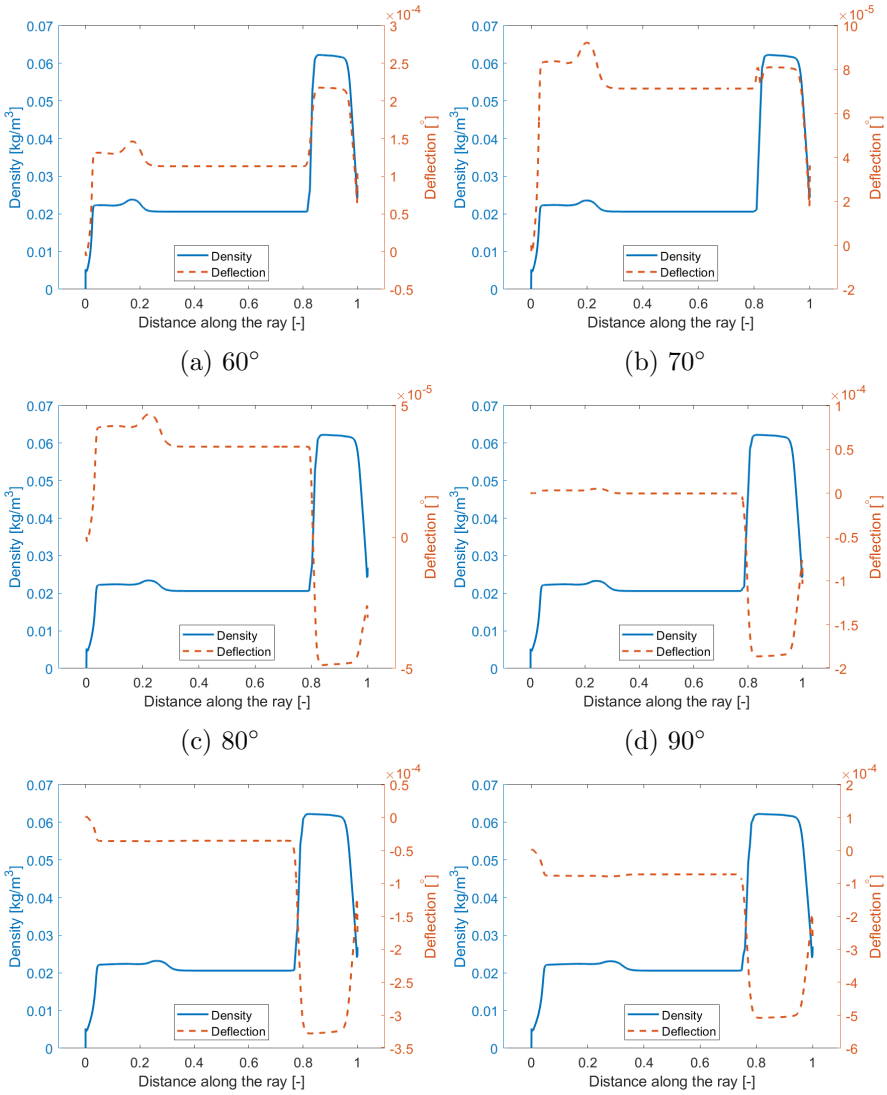

(a) 60° (b) 70°

(c) 80° (d) 90°

(e) 100° (f) 110°

Figure 6.13: Deflection angle and density along a ray propagating through the center of the laser beam for different line of sightss for the hypersonic low-density case.

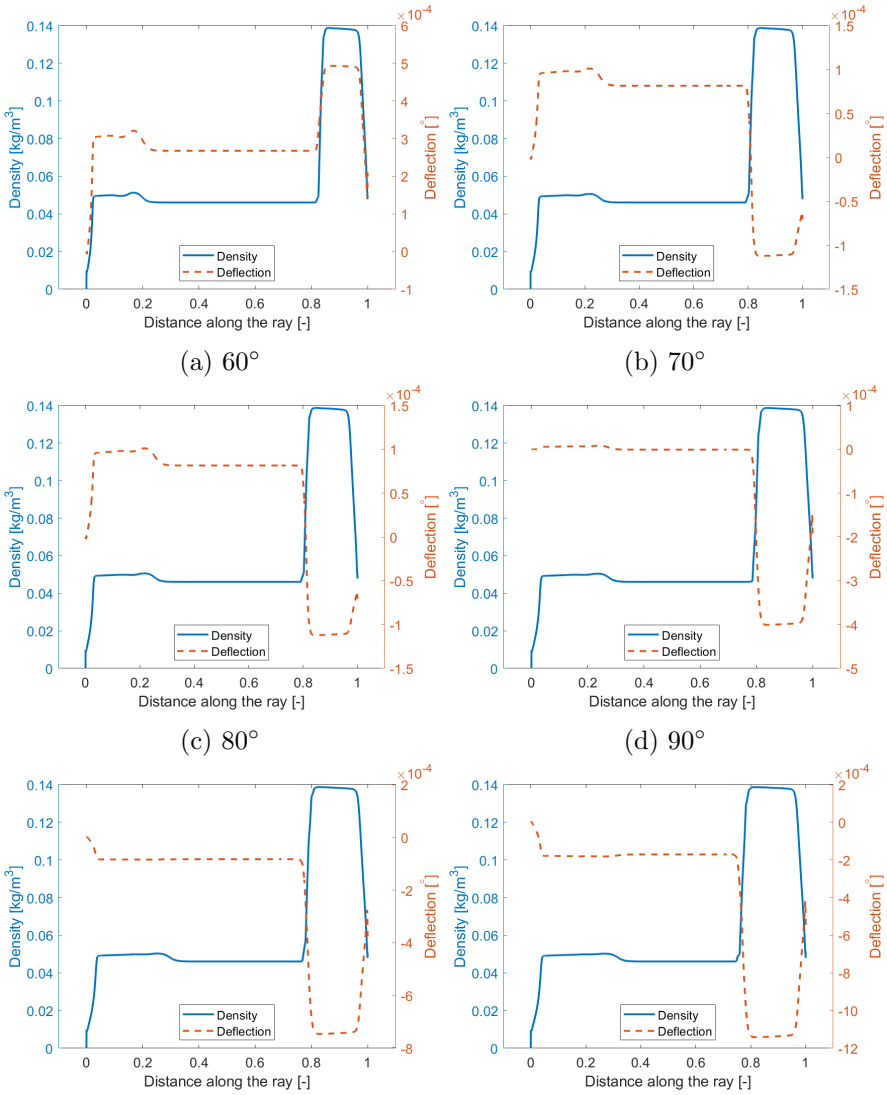

(a) 60° (b) 70°

(c) 80° (d) 90°

(e) 100° (f) 110°

Figure 6.14: Deflection angle and density along a ray propagating through the center of the laser beam for different line of sightss for the hypersonic high-density case.

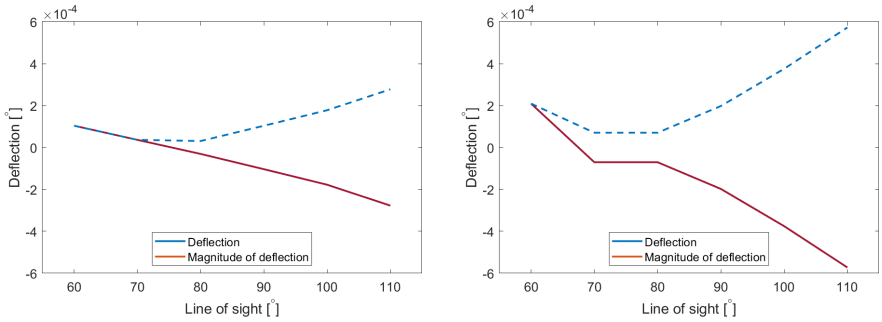

Figure 6.15: Calcaulated deflection depending on the line of sight: (**a**) low-density case and (**b**) high-density case.

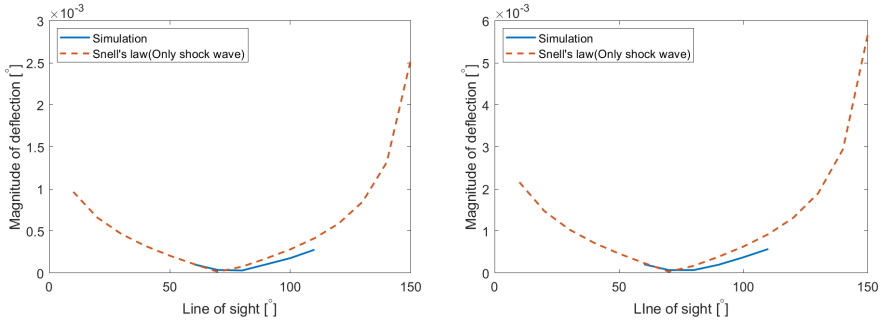

Figure 6.16: Comparison with Snell's law: (**a**) low-density case. (**b**) high-density case.

6.4.4 Numerical simulations with slip conditions on the up-plate

To exclude the aero-optical effects due to the up-plate boundary layer, slip conditions were adopted for up-plate, and the numerical simulations were conducted. The synthetic shadowgraph results for low-density and high-density cases are presented in Fig. 6.17. As slip conditions were adopted for the up-plate, the weak shock generated at the leading edge of the top plate disappeared. Thus, only the shock wave generated from the wedge and boundary layer over the wedge surface, which affects the propagation of the laser. Ray-tracing was also performed for this flow result, and the deflection along the center ray is presented in Fig. 6.18 for the low-density case and in Fig. 6.19 for the high-density case. Similar to the no-slip-condition case, the low-density and high-density cases have a similar profile but with different a magnitude. For a more comprehensive comparison, the final deflection depending on the LOS is depicted in Fig. 6.20. As slip conditions were adopted on the up-plate, the minimum point deflection could not be observed for the current range of the LOS. The minimum point is expected to be near an LOS of 50°, but more calculations are needed with a greater computational domain. Snell's law was applied to compare the shock wave and boundary layer. The comparison of the analytical and numerical solutions is depicted in Fig. 6.21. The difference between the solutions was greater than that with no-slip

conditions. Thus, as in the supersonic flow, the shock wave is not as dominant if only one boundary layer exists. Even for an LOS of 50°, where the shock wave effect increases in Snell's law, the deflection decreases, meaning that the boundary layer effect is relatively strong.

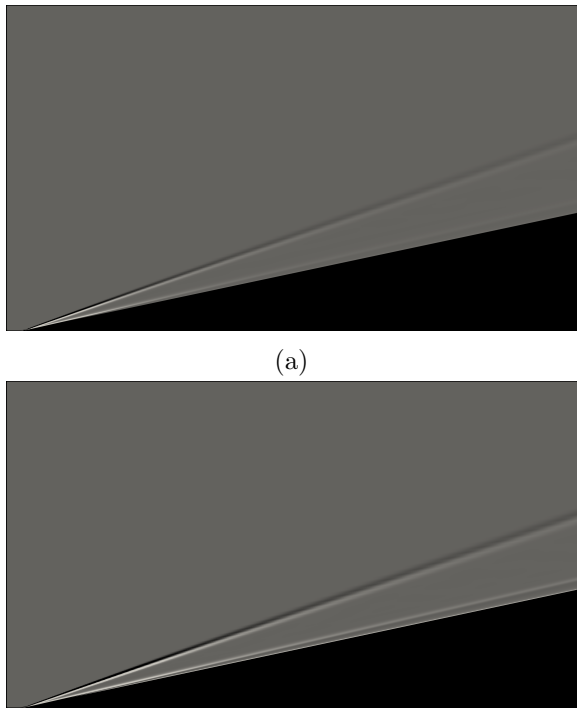

(a)

(b)

Figure 6.17: Numerical simulation result for hypersonic flow with up-plate slip conditions: (**a**) low-density case and (**b**) high-density case.

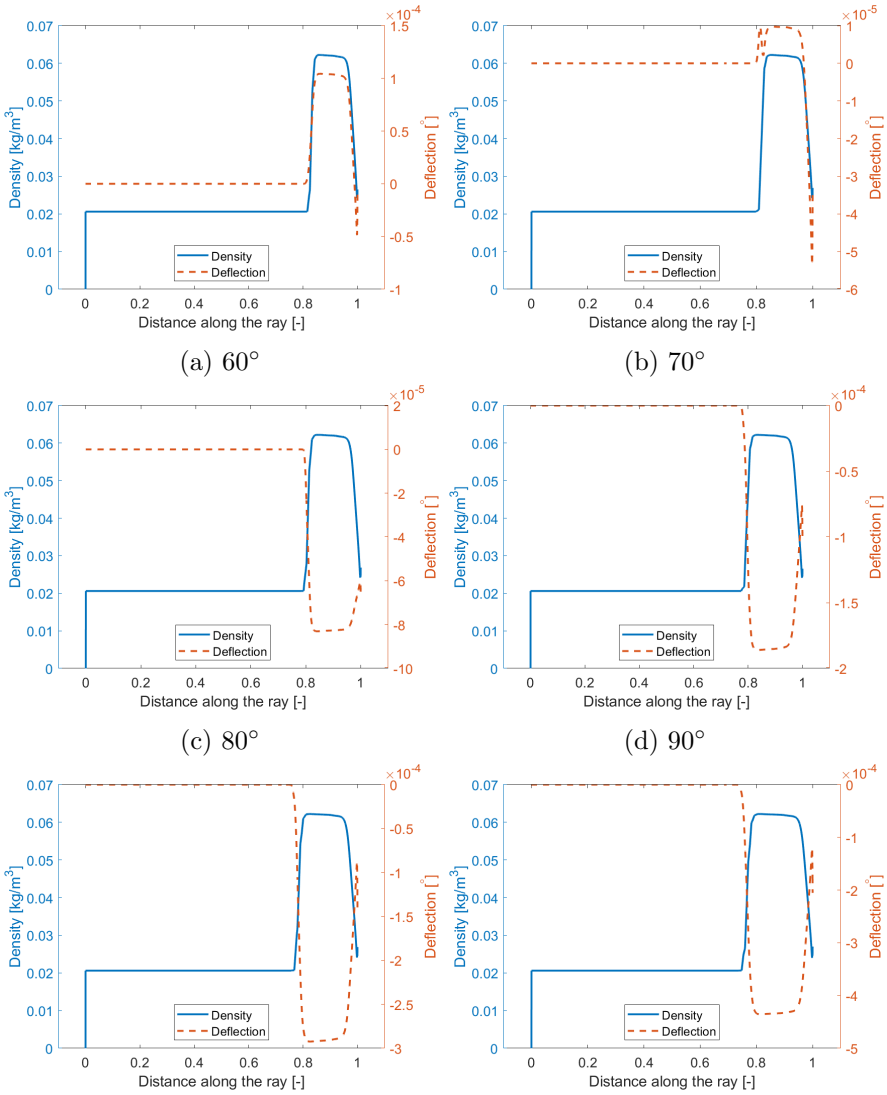

(a) 60°

(b) 70°

(c) 80°

(d) 90°

(e) 100°

(f) 110°

Figure 6.18: Deflection angle and density along a ray propagating through the center of the laser beam for different line of sights for the hypersonic low-density case with slip conditions on the up-plate.

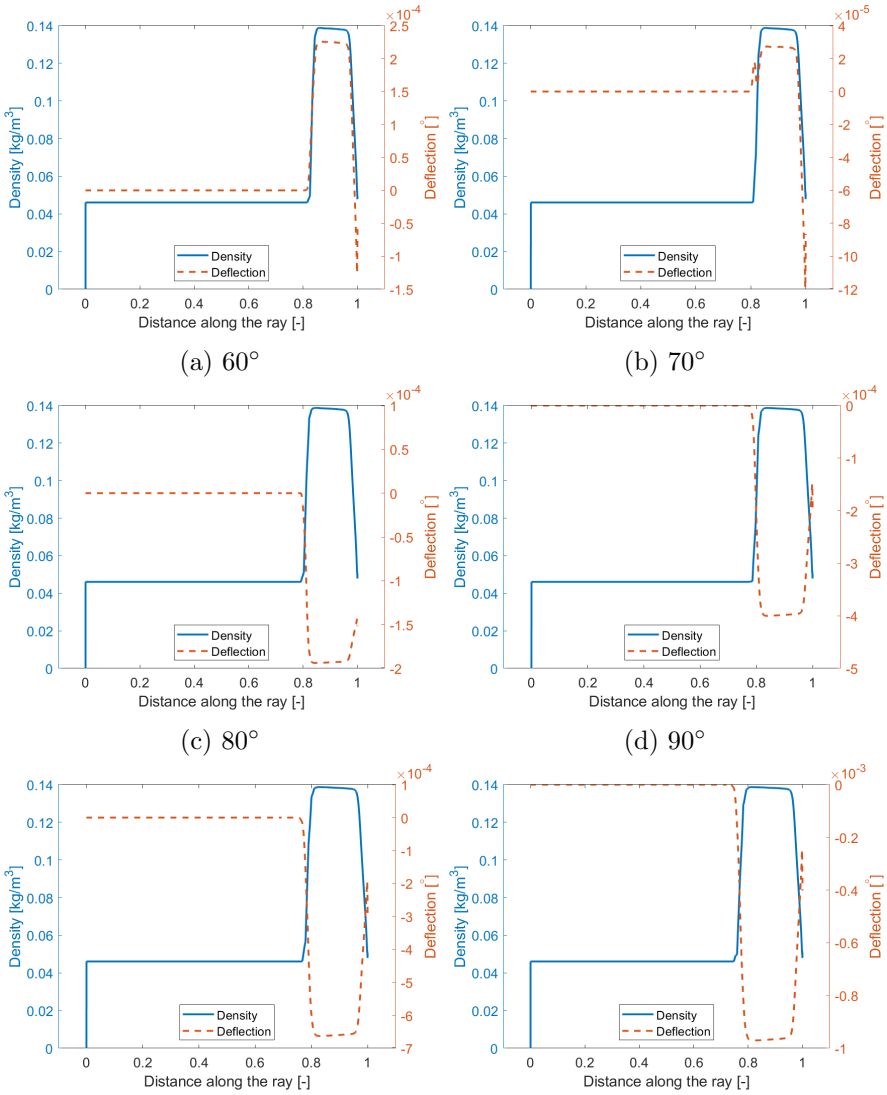

(a) 60° (b) 70°

(c) 80° (d) 90°

(e) 100° (f) 110°

Figure 6.19: Deflection angle and density along a ray propagating through the center of the laser beam for different line of sights for the hypersonic high-density case with slip conditions on the up-plate.

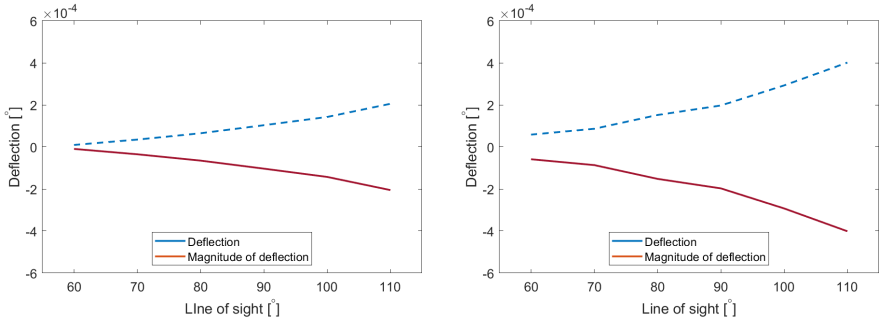

(a) (b)

Figure 6.20: Calculated deflection depending on the line of sight with slip conditions on the up-plate: (**a**) low-density case and (**b**) high-density case.

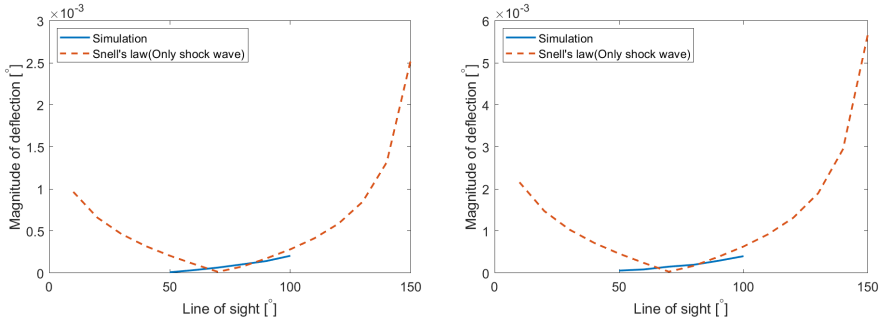

(a) (b)

Figure 6.21: Comparison using Snell's law with slip conditions on the up-plate: (**a**) low-density case and (**b**) high-density case.

6.5 Aero-optical Experiments on the Ogive Nose Cone Model

The flow field around the ogive nose cone model was visualized using the shadowgraph technique, as displayed in Fig. 6.22. In the figure, the shock wave over the wedge model was illustrated for comparison. The shock wave of the cone model was 16.7°, which is much smaller than the wedge model, at 18.4°. However, the shock layer height was much higher than the wedge model. The complicated flow field due to the window frame was expected, but in the flow visualization results, only the shock wave was visualized. Some other techniques, such as a tomograph, might be needed to visualize the 3D flow.

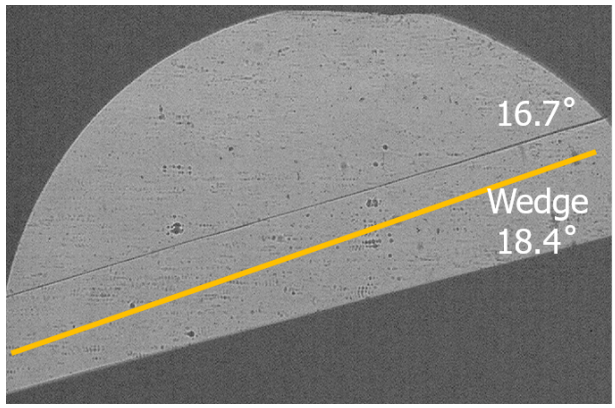

Figure 6.22: Flow visualization results for the ogive nose cone model.

The laser is propagated through the test section for two LOSs, which were 70°and 78°. Due to the test time, the wavefront was mea-

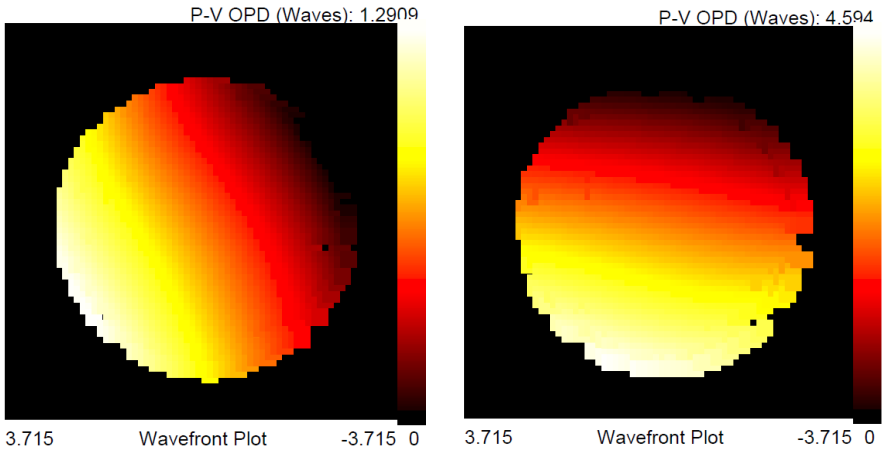

Figure 6.23: The optical path difference map measured for the ogive nose cone model: (**a**) line of sight at 70°and (**b**) line of sight at 78°.

sured only once for each run. Ten runs were conducted for each LOS. The wavefront of the laser propagating through this flow field is measured in Fig. 6.23, which is the minimum OPD_{rms} run for each LOS. Due to the bow shock wave, the OPD is expected to be curved rather than straight. However, the measured wavefront has parallel contours in a random direction. This may be due to the size of the laser beam, which is small to measure the curviness of the shock wave through the wavefront. The average OPD_{rms} for an LOS of 70°was 1.04λ and for an LOS of 78°was 1.25λ. More effect is needed when the LOS increases, which seems to be due to the angle between the laser and shock wave. The laser was almost perpendicular to the shock wave for a LOS of 70°. The value of the OPD_{rms} was 100 times larger than

that of the wedge model result. The flow field might introduce this magnitude of aero-optical effects, but the vibration of the wind tunnel seems to have more effect concerning this difference. Because the mirror is inside the cone model, the mirror might vibrate due to the aerodynamical vibration on the cone model. The disturbance of the vibration can be more clearly observed if the data for all runs are plotted together. The values of OPD_{rms} for all runs are plotted in Fig. 6.24, where the noisy data are observed.

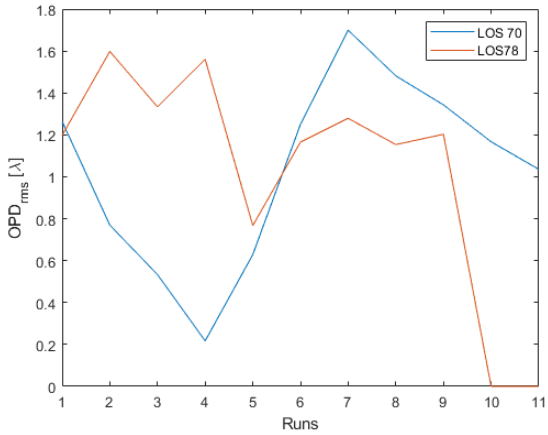

Figure 6.24: The root mean square optical path difference (OPD_{rms}) for each run with a line of sight (LOS) of 70°and 78°.

Chapter 7

Conclusions

Throughout the dissertation, the aero-optical phenomena due to the subsonic heated flow, supersonic compression ramp flow, hypersonic wedge flow, and hypersonic ogive nose cone flow were investigated using experimental and numerical methods. The experimental methods to quantify the aero-optical effects were established in the subsonic heated jet, and the same experimental method was adopted for the supersonic and hypersonic flow. In addition, new aero-optical experimental methods based on BOS techniques were suggested and validated in the subsonic heated jet. The wavefront of the laser beam propagating through these flow regimes was acquired and the aero-optical effects were analyzed. For the heated subsonic and supersonic flows, the numerical methods to obtain the flow field density and prop-

agation of the wavefront were evaluated using the experimental results and were analyzed to acquire more information than can be obtained with only the experimental methods. Thus, the importance of conducting both experimental and numerical methods simultaneously was demonstrated throughout the dissertation.

In subsonic heated flow, the feasibility of the hybrid BOS technique and the ray calculation as a wavefront acquisition system was evaluated. First, the images acquired using the BOS technique were validated by comparing them with the conventional schlieren images, which exhibited similar results. The BOS system is much simpler than that of the schlieren technique, but the spatial resolution is much less in the BOS technique due to the cross-correlation processing, which is the same method as that used for the particle image velocimetry. Second, the AFH Abel method was applied, and the density of the subsonic heated jet was acquired. Then, the optical calculation was performed, and this numerical result was evaluated using the SHWS measurement results. The calculated OPD from the BOS images and the measured OPD from the SHWS were within a similar range, and the tendency was similar. The difference between these two OPDs came from the turbulence effect of the hot jet, which was reduced in the time-averaged OPD results. The RMS for the calculated OPD from the BOS images is 0.0921λ, whereas the OPD measured by the SHWS is 0.1011λ. The relative percentage error of these two RMS

OPD values is 8.9%. Thus, the density field obtained with the BOS images is reliable, and the OPD acquired from the reconstructed density field shows the aero-optics effects of the flow qualitatively. The captured BOS images of flows are expected to be usable to acquire the density field and predict aero-optical phenomena that occurred with the flow using the acquired density field.

In supersonic flow, the aero-optical effects due to the shock wave and boundary layer, which are inevitable in supersonic flow, were investigated. The experimental method established in the heated subsonic flow was adopted, and numerical simulation was also conducted to acquire the deflection along the path through the flow field, which could not be acquired using the experimental methods. The shadowgraph technique was used to visualize the flow field, and the wavefront was measured using a SHWS. The numerical solution of the RANS equations provides the density of the flow field, which was verified against the shadowgraph image. The rays propagating through this flow field were computed by solving the ray equation. The wavefront acquired from the ray-tracing computation was compared with the time-averaged wavefront measured by the SHWS. The comparison revealed that the flow field developed over the 2D compression ramp is a 3D flow caused by the gap between the window and ramp.

The deflection angle of the ray and density of the flow field were extracted along the ray propagation path through the center of the

laser beam to compare the aero-optical effects induced by the shock wave and boundary layer. The boundary layers have an opposite effect and are canceled out as if almost no effect exists due to the shock wave. If one side of the boundary layer is excluded by assuming slip conditions, the boundary layer demonstrates similar aero-optical effects as a shock wave and is not negligible. Because the current optical measurement configuration has two boundary layers with opposite trends on aero-optical effects, a different system should be needed to study the aero-optical effects due to the boundary layer.

In hypersonic flow, similar research was conducted as in the supersonic flow. The wavefront propagating through the wedge flow was analyzed using a wavefront measurement system established in subsonic heated flow, and numerical methods were adopted to analyze the aero-optical effects along the optical path. The incident angle of the experiment is perpendicular to the wedge surface, which is the condition in which the aero-optical effects due to the boundary layer on the wedge surface are few, as discussed in the experiments on the supersonic compression flow.

Two operating conditions were investigated for hypersonic flow: low density and high density. The measurement results indicated randomness in the direction and magnitude of the tilt, which seemed to have substantial noise. Furthermore, using the analytical method adopted for supersonic flow, the deflection due to the high-density flow

seems to be greater than the deflection due to the low density. However, the measurement results revealed the opposite tendency, whereas the simulation results indicated the same tendency as an analytical solution.

However, when considering the refraction due to the windows at the up-plate and wedge, the direction of the tilt became the opposite, and the magnitude increased to 10 times larger than the tilt induced only by the flow field. From the simulation with an inclined window, the deflection of the laser beam changed significantly, and the refraction due to the windows seems to be dominant on the wavefront measurement in hypersonic flow. This seems to be due to the considerable difference between the density of the flow field and the density of the surrounding atmosphere. To reduce the refraction from the windows and to investigate only the aero-optical effects due to the flow field, a special wavefront measurement system should be designed, in which all components should be installed inside a vacuum chamber.

The individual contributions of the shock wave and boundary layer are similar to the supersonic flow field. For hypersonic flow over the ogive nose cone model, only experimental methods were adopted. However, the OPD value was 100 times higher than the wedge results, which does not appear to be physical. A large disturbance exists due to the aerodynamical vibration on the mirror inside the cone model, which is not used for the wedge model.

Overall, the research method for the aero-optics study was established and adopted for subsonic to hypersonic flow fields and includes experimental and numerical methods. The feasibility of the BOS techniques on the aero-optics study was also evaluated. In supersonic and hypersonic flow, the shock wave and boundary layer both have aero-optical effects, but if two boundary layers exist with the opposite direction of the gradient, the aero-optical effects due to boundary layers cancel out. For hypersonic flow, the refraction due to the windows cannot be neglected if the density of the flow field and the surrounding atmosphere of the wavefront measurement system are significantly different.

Bibliography

[1] J. Amannl, 2007 (accessed June 19, 2020), McDonnell Douglas F/A-18A Hornet - USA - Navy, URL: https://www.airliners.net/photo/USA-Navy/McDonnell-Douglas-F-A-18A-Hornet/1286859.

[2] M. Paschal, 2006 (accessed June 19, 2020), Boeing 737-3H4 - Southwest Airlines, URL: https://www.airliners.net/photo/Southwest-Airlines/Boeing-737-3H4/1075413/L.

[3] T. C. Lin, Development of u.s. air force intercontinental ballistic missile weapon systems, *Journal of Spacecraft and Rockets* 40 (2003) 491–509. doi:10.2514/2.3990.

[4] R. Mullins, T. Taylor, B. Scrip, B. Scrip, Visualization of weapon system effectiveness measures of performance, in: 36th AIAA Aerospace Sciences Meeting and Exhibit, Reno, Nevada, United States of America, 1998. doi:10.2514/6.1998-1062.

[5] G. H. Moon, M.-G. Seo, S.-M. Hong, S.-W. Shim, M. jea Tahk,

Time-to-go prediction for anti-ballistic missile midcourse guidance, in: AIAA Guidance, Navigation, and Control Conference, Grapevine, Texas, United States of America, 2017. doi:10.2514/6.2017-1239.

[6] W. J. Tropf, M. E. Thomas, T. J. Harris, S. A. Lutz, Performance of optical sensors in hypersonic flight, *Johns Hopkins APL Technical Digest* 8 (1987) 370–385.

[7] G. W. Sutton, J. E. Pond, R. Snow, Y. Hwang, Hypersonic interceptor aero-optics performance predictions, *Journal of Spacecraft and Rockets* 31 (1994) 592–599. doi:10.2514/3.26483.

[8] K. Gilbert, L. J. Otten, Aero-optical phenomena, Progress in astronautics and aeronautics, American Institute of Aeronautics and Astronautics, 1982. doi:10.2514/4.865541.

[9] W. Merzkirch, Flow Visualization, Academic Press, 1974. doi:10.1016/B978-0-12-491350-9.50006-X.

[10] E. J. Jumper, E. J. Fitzgerald, Recent advances in aero-optics, *Progress in Aerospace Sciences* 37 (2001) 299–339. doi:10.1016/S0376-0421(01)00008-2.

[11] E. Tromeur, E. Garnier, P. Sagaut, Analysis of the Sutton Model for aero-optical properties of compressible boundary layers, *Journal of Fluids Engineering* 128 (2006) 239–246. doi:10.1115/1.2170128.

[12] B. E. A. Saleh, M. C. Teich, Fundamentals of Photonics 2ed, John Wiley & Sons, Ltd, 2007.

[13] M. Wang, A. Mani, S. Gordeyev, Physics and computation of aero-optics, *Annual Review of Fluid Mechanics* 44 (2012) 299–321. doi:10.1146/annurev-fluid-120710-101152.

[14] D. T. Kyrazis, Airborne Laser Laboratory departure from Kirtland Air Force Base and a brief history of aero-optics, *Optical Engineering* 52 (2012) 1–6. doi:10.1117/1.OE.52.7.071403.

[15] S. Gordeyev, J. A. Cress, E. J. Jumper, A. B. Cain, Aero-optical environment around a cylindrical turret with a flat window, *AIAA Journal* 49 (2011) 308–315. doi:10.2514/1.J050476.

[16] E. J. Jumper, M. Zenk, S. Gordeyev, D. Cavalieri, M. R. Whiteley, The Airborne Aero-Optics Laboratory, AAOL, in: Acquisition, Tracking, Pointing, and Laser Systems Technologies XXVI, volume 8395, International Society for Optics and Photonics, SPIE, 2012, pp. 45–59. doi:10.1117/12.922734.

[17] E. J. Jumper, S. Gordeyev, D. Cavalieri, P. Rollins, M. Whiteley, M. Krizo, Airborne Aero-Optics Laboratory - Transonic (AAOL-T), in: 53rd AIAA Aerospace Sciences Meeting, Kissimmee, Florida, United States of America, 2015. doi:10.2514/6.2015-0675.

[18] H. A. Stine, W. Winovich, Light diffusion through high-speed tur-

bulent boundary layers, Technical Report NACA-RM-A56B21, National Advisory Committee for Aeronautics, Washington, United States of America, 1956.

[19] G. W. SUTTON, Effect of turbulent fluctuations in an optically active fluid medium, *AIAA Journal* 7 (1969) 1737–1743. doi:10.2514/3.5384.

[20] G. W. Sutton, Aero-optical foundations and applications, *AIAA Journal* 23 (1985) 1525–1537. doi:10.2514/3.9120.

[21] S. Elghobashi, A. Wassel, The effect of turbulent heat transfer on the propagation of an optical beam across supersonic boundary/shear layers, *International Journal of Heat and Mass Transfer* 23 (1980) 1229–1241. doi:10.1016/0017-9310(80)90053-8.

[22] E. Tromeur, E. Garnier, P. Sagaut, Large-eddy simulation of aero-optical effects in a spatially developing turbulent boundary layer, *Journal of Turbulence* 7 (2006) 1–28. doi:10.1080/14685240500307389.

[23] S. Gordeyev, E. Jumper, T. E. Hayden, Aero-optical effects of supersonic boundary layers, *AIAA Journal* 50 (2012) 682–690. doi:10.2514/1.J051266.

[24] S. Gordeyev, E. Jumper, T. E. Hayden, Aero-optical effects of supersonic boundary layers, *AIAA Journal* 50 (2012) 682–690. doi:10.2514/1.J051266.

[25] Q. Gao, Z. Jiang, S. Yi, X. Wang, Statistical characteristics of the tilts of the aero-optical aberration caused by the supersonic turbulent boundary layer, *Optics Letters* 38 (2013) 751–753. doi:10.1364/OL.38.000751.

[26] Q. Gao, S. Yi, Z. Jiang, L. He, X. Wang, Structure of the refractive index distribution of the supersonic turbulent boundary layer, *Optics and Lasers in Engineering* 51 (2013) 1113–1119. doi:10.1016/j.optlaseng.2013.03.016.

[27] Q. Gao, S.-H. Yi, Z.-F. Jiang, Universal form of the power spectrum of the aero-optical aberration caused by the supersonic turbulent boundary layer, *Chinese Physics B* 23 (2014) 104201. doi:10.1088/1674-1056/23/10/104201.

[28] H. Ding, S. Yi, Y. Zhu, L. He, Experimental investigation on aero-optics of supersonic turbulent boundary layers, *Applied Optics* 56 (2017) 7604–7610. doi:10.1364/AO.56.007604.

[29] H. Ding, S. Yi, X. Zhao, J. Yi, L. He, Research on aero-optical prediction of supersonic turbulent boundary layer based on aero-optical linking equation, *Optics Express* 26 (2018) 31317–31332. doi:10.1364/OE.26.031317.

[30] H. Ding, S. Yi, T. Ouyang, Y. Shi, L. He, Influence of turbulence structure with different scale on aero-optics induced by

supersonic turbulent boundary layer, *Optik* 202 (2020) 163565. doi:10.1016/j.ijleo.2019.163565.

[31] H. Ding, S. Yi, X. Zhao, Experimental investigation of aero-optics induced by supersonic film based on near-field background-oriented schlieren, *Applied Optics* 58 (2019) 2948–2962. doi:10.1364/AO.58.002948.

[32] J. H. Kiefer, A. C. Manson, Refractive index change and curvature in shock waves by angled beam refraction, *Review of Scientific Instruments* 52 (1981) 1392–1396. doi:10.1063/1.1136779.

[33] V. A. Banakh, A. A. Sukharev, A. V. Falits, Optical beam distortions induced by a shock wave, *Applied Optics* 54 (2015) 2023–2031. doi:10.1364/AO.54.002023.

[34] X.-W. Sun, W. Liu, Z.-X. Chai, Method of investigation for numerical simulation on aero-optical effect based on WCNS-E-5, *AIAA Journal* 57 (2019) 2017–2029. doi:10.2514/1.J057961.

[35] V. A. Banakh, A. A. Sukharev, Laser beam distortions caused by a shock wave near the turret of a supersonic aircraft, *Atmospheric and Oceanic Optics* 29 (2016).

[36] L. Xu, Z. Zhou, T. Ren, Study of a weak scattering model in aero-optic simulations and its computation, *Journal of the Optical Society of America A* 34 (2017) 594–601. doi:10.1364/JOSAA.34.000594.

[37] M. D. White, M. R. Visbal, Investigation of turbulent shock boundary interaction unsteadiness and its effects on aero-optics in a Mach 2 ramp flow, in: 45th AIAA Plasmadynamics and Lasers Conference, Atlanta, Georgia, United States of America, 2014. doi:10.2514/6.2014-2358.

[38] S. Gordeyev, M. R. Rennie, A. B. Cain, T. Hayden, Aero-optical measurements of high-Mach supersonic boundary layers, in: 46th AIAA Plasmadynamics and Lasers Conference, Dallas, Texas, United States of America, 2015. doi:10.2514/6.2015-3246.

[39] E. Frumker, O. Pade, Generic method for aero-optic evaluations, *Applied Optics* 43 (2004) 3224–3228. doi:10.1364/AO.43.003224.

[40] B. Sorrente, P. d'Espiney, R. Deron, Numerical study of the wavefront distortion in an aerodynamical flow field, in: A. Kohnle, K. Stein, J. D. Gonglewski (Eds.), Optics in Atmospheric Propagation and Adaptive Systems XI, volume 7108, International Society for Optics and Photonics, SPIE, 2008, pp. 92–101. doi:10.1117/12.802773.

[41] Z. Chen, S. Fu, Optical wavefront distortion due to supersonic flow fields, *Chinese Science Bulletin* 54 (2009) 623–627.

[42] S. Yi, L. Tian, Y. Zhao, L. He, Z. Chen, Aero-optical aberration measuring method based on NPLS and its application, *Chinese*

Science Bulletin. 55 (2010) 3545–3549. doi:10.1007/s11434-010-4104-5.

[43] H. Xiao, B. Zuo, Y. Tian, W. Zhang, C. Hao, C. Liu, Q. Li, F. Li, L. Zhang, Z. Fan, Joint influences of aerodynamic flow field and aerodynamic heating of the dome on imaging quality degradation of airborne optical systems, *Applied Optics* 51 (2012) 8625–8636. doi:10.1364/AO.51.008625.

[44] C. Hao, S. Chen, W. Zhang, J. Ren, C. Li, H. Pang, H. Wang, Q. Liu, C. Wang, H. Zou, Z. Fan, Comprehensive analysis of imaging quality degradation of an airborne optical system for aerodynamic flow field around the optical window, *Applied Optics* 52 (2013) 7889–7898. doi:10.1364/AO.52.007889.

[45] W. Zhang, F. Dang, C. Hao, Z. Fan, Aerodynamic heating of the dome on imaging quality degradation of conformal optical systems, *Optik* 125 (2014) 7120–7125. doi:10.1016/j.ijleo.2014.08.088.

[46] L. Liu, W. Meng, Y. Li, X. Dai, Z. Zu, Influence of aero-optical transmission on infrared imaging optical system in the supersonic flight, *Infrared Physics and Technology* 68 (2015) 110–118. doi:10.1016/j.infrared.2014.10.019.

[47] X. Zhao, S. Yi, H. Ding, Experimental study on the influence of attitude angle on the aero-optical effects of a hypersonic optical

dome, *Optik* 201 (2020) 163448. doi:10.1016/j.ijleo.2019.163448.

[48] Y. Yao, W. Xue, T. Wang, Y. Wu, L. Xu, Influence of los angle on aero-optics imaging deviation, *Optik* 202 (2020) 163732. doi:10.1016/j.ijleo.2019.163732.

[49] E. Hedlund, A. Collier, W. Murdaugh, Aero-optical testing in the NSWC Hypervelocity Tunnel No. 9, in: Annual Interceptor Technology Conference, Huntsville, Alabama, United States of America, 1992. doi:10.2514/6.1992-2797.

[50] G. Havener, C. Stepanek, Aero-optics testing capabilities at AEDC, in: 30th Aerospace Sciences Meeting and Exhibit, Reno, Nevada, United States of America, 1992. doi:10.2514/6.1992-760.

[51] D. Marren, Aero-optical demonstration test in the AEDC Hypervelocity Wind Tunnel 9, in: 8th Annual AIAA/BMDO Technology Conference and Exhibit, Boston, Massachusetts, United States of America, 1999.

[52] W. Yanta, C. Sprin, J. Lafferty, A. Collier, R. Bell, D. Neal, D. Hamrick, R. Copland, L. Pezzaniti, M. Banish, R. Shaw, Near- and farfield measurements of aero-optical effects due to propagation through hypersonic flows, in: 31st Plasmadynamics and

Lasers Conference, Denver, Colorado, United States of America, 2000. doi:10.2514/6.2000-2357.

[53] M. S. Holden, Large Energy National Shock Tunnel (LENS), Technical Report, Calspan/University of Buffalo Research Center, Buffalo, New York, United States of America, 1990.

[54] M. S. Holden, A preliminary study associated with the experimental measurement of the aero-optic characteristics of hypersonic configurations, Technical Report AD-A253-792, Calspan-UB Research Center, Buffalo, Newyork, United States of America, 1992.

[55] M. Holden, Calibration and validation studies in the LENS facility, Technical Report AD-A278-403, Calspan-UB Research Center, Buffalo, Newyork, United States of America, 1994.

[56] C. M. Wyckham, A. J. Smits, Aero-optic distortion in transonic and hypersonic turbulent boundary layers, *AIAA Journal* 47 (2009) 2158–2168. doi:10.2514/1.41453.

[57] L. Xu, Y. Cai, Influence of altitude on aero-optic imaging deviation, *Applied Optics* 50 (2011) 2949–2957. doi:10.1364/AO.50.002949.

[58] W. Ren, H. Liu, Effects of compressibility and knudsen number on the aero optics in hypersonic flow fields, *Journal of Shanghai Jiaotong University (Science)* 21 (2016).

[59] S. Gordeyev, T. J. Juliano, Optical characterization of nozzle-wall mach-6 boundary layers, in: 54th AIAA Aerospace Sciences Meeting, San Diego, California, United States of America, 2016. doi:10.2514/6.2016-1586.

[60] S. Gordeyev, T. J. Juliano, Optical measurements of transitional events in a mach-6 boundary layer, *AIAA Journal* 55 (2017) 3629–3639. doi:10.2514/1.J055759.

[61] L. E. Mackey, I. D. Boyd, Assessment of hypersonic flow physics on aero-optics, *AIAA Journal* 57 (2019) 3885–3897. doi:10.2514/1.J057869.

[62] M. M. Malley, G. W. Sutton, N. Kincheloe, Beam-jitter measurements of turbulent aero-optical path differences, *Applied Optics* 31 (1992) 4440–4443. doi:10.1364/AO.31.004440.

[63] E. J. Jumper, R. J. Hugo, Quantification of aero-optical phase distortion using the small-aperture beam technique, *AIAA Journal* 33 (1995) 2151–2157. doi:10.2514/3.12960.

[64] R. J. Hugo, E. J. Jumper, Experimental measurement of a time-varying optical path difference by the small-aperture beam technique, *Applied Optics* 35 (1996) 4436–4447. doi:10.1364/AO.35.004436.

[65] E. J. Fitzgerald, E. J. Jumper, Two-dimensional optical wavefront measurements using a small-aperture beam technique

derivative instrument, *Optical Engineering* 39 (2000) 3285–3293. doi:10.1117/1.1327838.

[66] D. Neal, E. Hedlund, M. Lederer, A. Collier, C. Spring, B. Yanta, Shack-hartmann wavefront sensor testing of aero-optic phenomena, in: 20th AIAA Advanced Measurement and Ground Testing Technology Conference, Albuquerque, New Mexico, United States of America, 1998. doi:10.2514/6.1998-2701.

[67] R. M. Rennie, M. Nguyen, S. Gordeyev, E. J. Jumper, A. B. Cain, T. E. Hayden, Wave-front measurements of a supersonic boundary layer using laser induced breakdown, *AIAA Journal* 55 (2017) 2349–2357. doi:10.2514/1.J055611.

[68] L. Tian, S. Yi, Y. Zhao, L. He, Z. Chen, Aero-optical wavefront measurement technique based on bos and its applications, *Chinese Science Bulletin* 56 (2011) 2320–2326.

[69] A. Bichal, B. S. Thurow, On the application of background oriented schlieren for wavefront sensing, *Measurement Science and Technology* 25 (2013) 015001. doi:10.1088/0957-0233/25/1/015001.

[70] G. Guo, H. Liu, Correcting aero-optical wavefront aberration of the supersonic mixing layer based on periodic pulse forcing, *Applied Optics* 56 (2017) 4613–4621. doi:10.1364/AO.56.004613.

[71] Y. Liu, Y. Yuan, X. Guo, T. Suo, Y. Li, Q. Yu, Numerical in-

vestigation of the error caused by the aero-optical environment around an in-flight wing in optically measuring the wing deformation, *Aerospace Science and Technology* 98 (2020) 105663. doi:10.1016/j.ast.2019.105663.

[72] S. Y. Lee, M. C. Jeong, I.-S. Jeung, H. J. Lee, J. K. Lee, Super/hypersonic aero-optical effects induced by external jet cooling, in: The 30th International Symposium on Shock Waves, Tel Aviv, israel, 2015.

[73] S. Y. Lee, M. C. Jeong, I.-S. Jeung, H. J. Lee, J. K. Lee, Aero-optical measurement in shock wave of hypersonic flow field, in: The 30th International Symposium on Shock Waves, Tel Aviv, israel, 2015.

[74] S. Lee, M. Jeong, M. Chang, I.-S. Jeung, H. J. Lee, Wavefront aberration in a laser beam induced by supersonic flow field around a wedge, in: The 31st International Symposium on Shock Waves, Nagoya, Japan, 2017.

[75] S. Y. Lee, H. S. Lim, I.-S. Jeung, H. J. Lee, J.-Y. Choi, Contoured nozzle design and performance validation, in: 2014 KSPE Fall Conference, Jeongseon, Gangwon-do, Republic of Korea, 2014.

[76] W. Thielicke, E. J. Stamhuis, Pivlab – towards user-friendly, affordable and accurate digital particle image velocimetry in

matlab, *Journal of Open Research Software* 2 (2014) e30. doi:10.5334/jors.bl.

[77] S. Lee, S. H. Kim, H. J. Lee, I.-S. Jeung, Density acquisition and aero-optics measurement from bos images for a hot jet, *International Journal of Aeronautical and Space Sciences* 19 (2018).

[78] S. Lee, S. D. Kim, B. J. Lee, Aero-optical phenomena due to boundary layer and shock wave around a wedge in supersonic flow, in: KSAS 2019 Fall Conference, Jeju, Republic of Korea, 2019.

[79] F. Sourgen, F. Leopold, D. Klatt, Reconstruction of the density field using the colored background oriented schlieren technique (cbos), *Optics and Lasers in Engineering* 50 (2012) 29–38. doi:10.1016/j.optlaseng.2011.07.012, advances in Flow Visualization.

[80] G. S. Settles, Schlieren and Shadowgraph Techniques: Visualizing Phenomena in Transparent Media, Springer-Verlag Berlin Heidelberg, 2001.

[81] H. Chehouani, M. E. Fagrich, Adaptation of the Fourier-Hankel method for deflection tomographic reconstruction of axisymmetric field, *Applied Optics* 52 (2013) 439–448. doi:10.1364/AO.52.000439.

[82] D. J. Tan, D. Edgington-Mitchell, D. Honnery, Measurement of

density in axisymmetric jets using a novel background-oriented schlieren (BOS) technique, *Experiments in Fluids* 56 (2015). doi:10.1007/s00348-015-2076-6.

[83] A. Sharma, D. V. Kumar, A. K. Ghatak, Tracing rays through graded-index media: a new method, *Applied Optics* 21 (1982) 984–987. doi:10.1364/AO.21.000984.

[84] U. Hartmann, J. R. Seume, Combining ART and FBP for improved fidelity of tomographic BOS, *Measurement Science and Technology* 27 (2016) 097001. doi:10.1088/0957-0233/27/9/097001.

[85] E. Luthman, N. Cymbalist, D. Lang, G. Candler, P. Dimotakis, Simulating schlieren and shadowgraph images from LES data, *Experiments in Fluids* 60 (2019) 134. doi:10.1007/s00348-019-2774-6.

초 록

탄도탄 요격유도탄이 성공적으로 요격하기 위해서는 탐색기의 성능이 중요하다. 그런데, 비행 중에는 탐색기창 주위에 유동에 의한 공기광학 효과로 인하여 탐색의 광학 센서로 촬영하는 이미지가 왜곡되어 목표를 분간하기 어려워진다. 따라서 탐색기의 성공적인 작동을 위해서는 공기광학 현상을 연구하여 광학센서로 획득한 이미지를 보정하는 과정이 필수적이다. 또한, 일반적으로 탄도탄 요격유도탄이 초음속 또는 극초음속으로 비행하기 때문에 이러한 고속 유동에 의해 발생하는 공기광학 효과를 분석해야 한다. 특히 초음속과 극초음속에서는 충격파 및 경계층이 반드시 발생하고 피할 수 없기 때문에, 충격파 및 경계층에 의한 공기광학 효과는 반드시 연구해야 한다. 본 연구에서는 초음속 및 극초음속 유동에서 충격파 및 경계층이 각각 공기광학 효과에 어떠한 영향을 미치는가를 실험 및 수치해석을 통해 분석한다. 또한, 배경지형 슐리렌(BOS)을 기반으로 한 새로운 실험 기법을 제안하고, 이 계측 기법을 다른 파면 계측기를 이용하여 검증하고자 한다. 이에 따라 아음속 고온 제트에서 샥-하트만 파면 계측기 결과와 BOS 기반 실험 기반 계측 결과가 대체로 일치하는 것을 검증하였다. BOS 기반 계측 기법은 유동 성질과 광학 특성을 동시에 획득할 수 있기 때문에, 유동과 공기광학 사이의 관계를 면밀히 파악할 수 있을 것으로 예상된다. 초음속 유동에 대해서는 압축 비탈길 주위의 유동에 의한 공기광학 효과를 연구하였으며 극초음속 유동에 대해서는 쐐기와 원뿔형 모델 주위의 유동에 의한 공기광학 효과를 파악하였다. 충격파 및 경계층 각자에 의한 공기광학 효과를 비교하기 위하여 수치해석도 수행하였다. 유동장은

Reynolds-averaged Navier-Stokes 식을 이차원 가정을 하여 수치적으로 해석하였으며 광선 추적 기법을 이용하여 광학파의 거동을 계산하였다. 전산해석 결과는 실험 결과를 이용하여 검증하였다. 레이저 빔의 중심에 위치한 광선을 따라서 굴절각을 추출하여 충격파 및 경계층 각각에 의한 빔의 굴절각을 비교하였다. 현재의 파면 계측 기법에서는 항상 두 개의 경계층을 지나며, 이 두 개의 경계층이 각각 반대 방향의 밀도 변화율을 가지고 있기 때문에 두 경계층에 의한 공기광학 효과가 서로 상쇄되는 현상을 발견하였다. 따라서 현재의 파면 계측 기법과 같이 두 개의 경계층을 지나는 경우에는 경계층의 효과가 미미하게 나타나고, 충격파의 효과가 상대적으로 크게 나타날 수 있다. 그러나 만약 충격파와 경계층이 하나씩만 존재한다면 각각에 의한 공기광학 효과를 무시할 수 없는 수준이기 때문에 둘 다 많은 영향을 미친다.

주 요 어: 공기광학, 충격파, 초음속 유동, 극초음속 유동, 파면 계측, 광선 추적, 배경 지향 슐리렌